

UC Berkeley

UC Berkeley Previously Published Works

Title

The influence of seawater carbonate chemistry, mineralogy, and diagenesis on calcium isotope variations in Lower-Middle Triassic carbonate rocks

Permalink

<https://escholarship.org/uc/item/6v0262wf>

Authors

Lau, Kimberly V
Maher, Kate
Brown, Shaun T
et al.

Publication Date

2017-11-01

DOI

10.1016/j.chemgeo.2017.09.006

Peer reviewed

1 **The influence of seawater carbonate chemistry, mineralogy, and diagenesis on**
2 **calcium isotope variations in Lower-Middle Triassic carbonate rocks**

3
4 Kimberly V. Lau^{a,1}, Kate Maher^a, Shaun T. Brown^{b,c}, Adam B. Jost^{a,d}, Demir Altiner^e, Donald J.
5 DePaolo^{b,c}, Anton Eisenhauer^f, Brian M. Kelley^{a,g}, Daniel J. Lehrmann^h, Adina Paytanⁱ, Juan
6 Carlos Silva-Tamayo^{a,j}, Meiyi Yu^k, and Jonathan L. Payne^a
7

8 ^aDepartment of Geological Sciences, Stanford University, 450 Serra Mall Bldg. 320, Stanford, CA
9 94305, USA.

10 ^bDepartment of Earth and Planetary Science, University of California, Berkeley, 307 McCone
11 Hall, Berkeley, CA 94709, USA.

12 ^cEnergy Geosciences Division, E.O. Lawrence Berkeley National Laboratory, 1 Cyclotron Road,
13 Berkeley, CA 94720, USA.

14 ^dDepartment of Earth, Atmospheric, and Planetary Sciences, Massachusetts Institute of
15 Technology, 77 Massachusetts Ave., Cambridge, MA 02139.

16 ^eDepartment of Geological Engineering, Middle East Technical University, Üniversiteler Mah.
17 Dumlupınar Blv. No: 1,06800, 06531, Ankara, Turkey.

18 ^fGEOMAR, Helmholtz Centre for Ocean Research Kiel, Wischhofstr. 1-3, 24148 Kiel, Germany.

19 ^gExxonMobil Upstream Research Company, 22777 Springwoods Village Parkway, Spring, TX
20 77389.

21 ^hGeosciences Department, Trinity University, Marrs McLean Hall, One Trinity Place, San
22 Antonio, TX 78212, USA.

23 ⁱInstitute of Marine Sciences, University of California, Santa Cruz, 1156 High Street, Santa Cruz,
24 CA 95064 USA.

25 ^jTESTLAB Geo-Ambiental, Kra 45D #60-16, Medellin, Colombia.

26 ^kCollege of Resource and Environment Engineering, Guizhou University, Caijiaguan, Guiyang
27 550003, Guizhou, China.

28
29 ¹corresponding author (kvlau@ucr.edu). Present address: Department of Earth Sciences,
30 University of California, Riverside, 900 University Avenue, Riverside, CA 92521, USA.

31
32 **Keywords: calcium isotopes; carbonates; early diagenesis; recrystallization; calcium cycling**
33

ABSTRACT

The geological calcium cycle is linked to the geological carbon cycle through the weathering and burial of carbonate rocks. As a result, calcium (Ca) isotope ratios ($^{44}\text{Ca}/^{40}\text{Ca}$, expressed as $\delta^{44/40}\text{Ca}$) can help to constrain ancient carbon cycle dynamics if Ca cycle behavior can be reconstructed. However, the $\delta^{44/40}\text{Ca}$ of carbonate rocks is influenced not only by the $\delta^{44/40}\text{Ca}$ of seawater but also by diagenetic processes and fractionation associated with carbonate precipitation. In this study, we investigate the dominant controls on carbonate $\delta^{44/40}\text{Ca}$ in Upper Permian to Middle Triassic limestones (ca. 253 to 244 Ma) from south China and Turkey. This time interval is ideal for assessing controls on Ca isotope ratios in carbonate rocks because fluctuations in seawater $\delta^{44/40}\text{Ca}$ may be expected based on several large carbon isotope ($\delta^{13}\text{C}$) excursions ranging from -2 to +8‰. Parallel negative $\delta^{13}\text{C}$ and $\delta^{44/40}\text{Ca}$ excursions were previously identified across the end-Permian extinction horizon. Here, we find a second negative excursion in $\delta^{44/40}\text{Ca}$ of ~0.2‰ within Lower Triassic strata in both south China and Turkey; however, this excursion is not synchronous between regions and thus cannot be interpreted to reflect secular change in the $\delta^{44/40}\text{Ca}$ of global seawater. Additionally, $\delta^{44/40}\text{Ca}$ values from Turkey are consistently 0.3‰ lower than contemporaneous samples from south China, providing further support for local or regional influences. By measuring $\delta^{44/40}\text{Ca}$ and Sr concentrations ([Sr]) in two stratigraphic sections located at opposite margins of the Paleo-Tethys Ocean, we can determine whether the data represent global conditions (*e.g.*, secular variations in the $\delta^{44/40}\text{Ca}$ of seawater) versus local controls (*e.g.*, original mineralogy or diagenetic alteration). The [Sr] and $\delta^{44/40}\text{Ca}$ data from this study are best described statistically by a log-linear correlation that also exists in many previously published datasets of various geological ages. Using a model of early marine diagenetic water-rock interaction, we illustrate that this general correlation can be explained by the chemical evolution of bulk carbonate sediment samples with different initial mineralogical compositions that subsequently underwent recrystallization. Although early diagenetic resetting and carbonate mineralogy strongly influence the carbonate $\delta^{44/40}\text{Ca}$ values, the relationship between [Sr] and $\delta^{44/40}\text{Ca}$ holds potential for reconstructing first-order secular changes in seawater $\delta^{44/40}\text{Ca}$ composition.

1. INTRODUCTION

Records of calcium isotopes ($\delta^{44/40}\text{Ca}$), measured in marine carbonate rocks, fossils, and authigenic minerals, provide important constraints on global calcium (Ca) and carbon cycle dynamics over the past billion years (*e.g.*, Blättler et al., 2011; Brazier et al., 2015; De La Rocha and DePaolo, 2000; Du Vivier et al., 2015; Fantle and DePaolo 2005; Farkaš et al., 2007 and 2016; Gothmann et al., 2016; Griffith et al., 2008 and 2011; Holmden et al., 2009 and 2012a; Husson et al., 2015; Jost et al., 2014 and 2017; Kasemann et al., 2014; Payne et al., 2010; Sawaki et al., 2014; Silva-Tamayo et al., 2010a and 2010b). Seawater $\delta^{44/40}\text{Ca}$ may reflect coupled C and Ca cycling because its value is controlled by the balance between the major Ca input, continental weathering, and the major Ca output, CaCO_3 burial (De La Rocha and DePaolo, 2000; DePaolo, 2004; Fantle and DePaolo, 2005). During CaCO_3 precipitation, Ca is fractionated such that ^{40}Ca is preferentially incorporated into carbonate minerals, enriching seawater in ^{44}Ca relative to the riverine input (*e.g.*, DePaolo, 2004). Assuming that riverine $\delta^{44/40}\text{Ca}$ does not vary significantly across time, the $\delta^{44/40}\text{Ca}$ record of carbonate sediments could reflect changes in carbonate mineralogy or the sedimentation flux. If the carbonate burial flux increases due to higher alkalinity (with no contemporaneous changes in hydrothermal input or groundwater flux), seawater $\delta^{44/40}\text{Ca}$ also increases. On the other hand, if carbonate saturation state (Ω) decreases temporarily in an acidified ocean, reduced carbonate sedimentation results in a transient decrease in seawater $\delta^{44/40}\text{Ca}$ (Payne et al., 2010). In this study, we examine the potential for Ca isotopes, as recorded in carbonate rocks, to provide insight into the coupled C and Ca cycles by focusing on Lower to Middle Triassic carbonate strata from stratigraphic sections located in south China and Turkey.

Carbonate $\delta^{44/40}\text{Ca}$ records can provide constraints on marine C and Ca cycling if variations in these data reflect variations in seawater $\delta^{44/40}\text{Ca}$. Calcium isotopes are readily analyzed in bulk carbonate rock, an approach that is useful for time intervals prior to the Cenozoic that are not represented in the deep-sea sediment record. However, various factors can affect the extent to which the $\delta^{44/40}\text{Ca}$ composition of bulk carbonate rock tracks seawater at the time of deposition. The kinetic fractionation of Ca isotopes during precipitation of CaCO_3 from seawater ($\Delta_{\text{carbonate-seawater}}$, hereafter $\Delta_{\text{c-s}}$) is likely controlled by reaction rate, mineralogy, and fluid stoichiometry (DePaolo, 2004; Fantle and DePaolo, 2005; Fantle et al., 2010; Gussone et al., 2005; Nielsen et al., 2012; Sime et al., 2007; Skulan et al., 1997; Tang et al., 2008a). Some of these factors can vary globally and across geologic time through changes in biology and ocean chemistry (*e.g.*, Blättler

94 et al., 2012; Farkaš et al., 2007), whereas others vary at limited spatial scales. The $\delta^{44/40}\text{Ca}$ of
95 shallow-marine carbonates may also be influenced by mixing with groundwater or altered by post-
96 depositional interaction with diagenetic fluids (Fantle, 2015; Fantle and Higgins, 2014; Holmden,
97 2009; Holmden et al., 2012b). Therefore, many factors must be considered before interpreting the
98 carbonate $\delta^{44/40}\text{Ca}$ record as secular changes in seawater $\delta^{44/40}\text{Ca}$.

99 The Early to Middle Triassic recovery from the end-Permian mass extinction is an ideal
100 time interval in which to examine the controls on the $\delta^{44/40}\text{Ca}$ of carbonate rocks because there is
101 ample evidence for large perturbations in the global C and Ca cycles. The end-Permian catastrophe
102 (ca. 252 Ma), the largest mass extinction of the Phanerozoic, was likely triggered by a large and
103 rapid release of C from the emplacement of the Siberian Traps, resulting in acidification, anoxia,
104 and warming coincident with the loss of ~80% of marine genera (reviewed in Payne and Clapham,
105 2012). Large fluctuations in the carbon cycle characterized the five million years after the end-
106 Permian mass extinction: Early Triassic $\delta^{13}\text{C}$ values exhibit multiple negative (down to
107 approximately -2‰) and positive (up to approximately 8‰) excursions (Atudorei, 1999; Horacek
108 et al., 2007a; Horacek et al., 2007b; Payne et al., 2004; Richoz, 2006), and did not fully stabilize
109 until the Middle Triassic. Biodiversity, ecological complexity, and body size also did not return to
110 pre-extinction levels until the Middle Triassic, suggesting that adverse conditions extended beyond
111 the initial extinction event (*e.g.*, Brayard et al., 2006; Brayard et al., 2009; Chen and Benton, 2012;
112 Foster and Twitchett, 2014; Hallam, 1991; Orchard, 2007; Schaal et al., 2016; Stanley, 2009).
113 Because $\delta^{44/40}\text{Ca}$ data can be collected from the same samples as those used to determine variations
114 in $\delta^{13}\text{C}$, this time interval serves as an important test case for the utility of $\delta^{44/40}\text{Ca}$ data in carbonate
115 rocks for reconstructing seawater $\delta^{44/40}\text{Ca}$, as well as for elucidating links between the Early-
116 Middle Triassic Ca and C cycles.

117 At the Permian/Triassic boundary, the globally observed negative $\delta^{13}\text{C}$ excursion is
118 commonly attributed to a release of ^{13}C -depleted CO_2 during Siberian Traps volcanism and
119 volatilization of C-rich sediments (*e.g.*, Cui et al., 2013; Svensen et al., 2009). Because rapidly
120 elevated atmospheric $p\text{CO}_2$ would increase Ca weathering as well as decrease the burial rate of
121 CaCO_3 , a negative excursion in $\delta^{44/40}\text{Ca}$ that parallels this negative $\delta^{13}\text{C}$ excursion was interpreted
122 as evidence for a major episode of ocean acidification (Hinojosa et al., 2012; Payne et al., 2010).
123 A number of additional lines of evidence support an end-Permian acidification event, including
124 high $^{187}\text{Re}/^{188}\text{Os}$ ratios in shales (Georgiev et al., 2011), the paleophysiology of animals that were

125 most severely impacted (Clapham and Payne, 2011; Kiessling and Simpson, 2011; Knoll et al.,
126 2007), sedimentological observations such as dissolution surfaces and subsequent abiotic
127 carbonate precipitation (Baud et al., 2007; Payne et al., 2007; Pruss et al., 2006; Weidlich and
128 Bernecker, 2011; Woods et al., 1999; Woods, 2014), and a negative boron isotope excursion that
129 suggests a short-lived acidification event (Clarkson et al., 2015).

130 In contrast to the boundary $\delta^{13}\text{C}$ excursion, the causes of Early Triassic $\delta^{13}\text{C}$ instability are
131 widely debated. The large negative and positive $\delta^{13}\text{C}$ excursions that characterize the remainder
132 of the Early Triassic have been interpreted to represent several pulses of volcanic C release (Payne
133 and Kump, 2007). However, radiometric dates of Siberian Traps rocks indicate that magmatism
134 greatly diminished within 0.5 Ma of the main extinction pulse (Burgess and Bowring, 2015),
135 suggesting that volcanic pulses are unlikely to have continued for 5 Ma. Nonetheless, evidence
136 from sedimentology and paleoredox proxies support variations in Ω of the Early Triassic oceans.
137 Microbialites and aragonite fan pseudomorphs—representative of supersaturated oceans with high
138 Ω —occur in localities throughout the Tethys and the eastern Panthalassa margin that span the
139 Permian/Triassic boundary through the Early Triassic (Baud et al., 2007; Pruss et al., 2006;
140 Weidlich and Bernecker, 2011; Woods et al., 1999). Widespread abiotic CaCO_3 precipitation,
141 particularly in deeper waters, is characteristic of an extensively anoxic ocean (Lau et al., 2016;
142 Song et al., 2014) dominated by anaerobic metabolisms that increase alkalinity and authigenic
143 carbonate precipitation at or below the sediment-water interface (SWI) (Bergmann et al., 2013;
144 Higgins et al., 2009; Loyd et al., 2012; Maher et al., 2006; Woods, 2014). Early Triassic C and
145 uranium (U) isotope records indicate that the oxygen minimum zone (OMZ) expanded laterally
146 and to shallower depths (Algeo et al., 2010; Algeo et al., 2011; Lau et al., 2016; Meyer et al.,
147 2011), potentially affecting organic carbon burial and authigenic carbonate precipitation. Thus,
148 $\delta^{13}\text{C}$ in the Early Triassic may have fluctuated dramatically from changing organic carbon burial
149 fluxes and associated Ω fluctuations—changes that should also be reflected in the $\delta^{44/40}\text{Ca}$ record.

150 Although $\delta^{44/40}\text{Ca}$ data have been collected in carbonate rocks for the ~ 0.5 Myr
151 immediately bracketing the end-Permian mass extinction, such records have not yet been compiled
152 for the subsequent 15 Myr. If $\delta^{13}\text{C}$ excursions in the Early Triassic are associated with changes in
153 seawater carbonate chemistry, the related fluctuations in seawater Ca should result in $\delta^{44/40}\text{Ca}$
154 excursions recorded in multiple contemporaneous stratigraphic records. If the observed records do
155 not agree among sites, then other processes must be influencing $\delta^{44/40}\text{Ca}$ in these carbonate rocks.

156

157 **2. MATERIALS AND METHODS**

158 **2.1 Geologic Setting**

159 In this study, we analyzed $\delta^{44/40}\text{Ca}$ in samples from shallow-marine carbonate stratigraphic
160 sections located in south China and Turkey. We focus on these localities because they are
161 promising for capturing secular trends in Early to Middle Triassic seawater $\delta^{44/40}\text{Ca}$ as C and U
162 isotopic data show general agreement between sections (Lau et al., 2016).

163

164 *2.1.1 Dajiang section, Great Bank of Guizhou, south China*

165 The Great Bank of Guizhou (GBG) is an exceptionally preserved isolated carbonate
166 platform in the Nanpanjiang Basin of the equatorial eastern Tethys (Figure 1; Lehrmann et al.,
167 1998). The platform is exposed in geologic cross-section along a syncline running roughly north
168 to south at the town of Bianyang (Lehrmann et al., 1998). Previous studies of the GBG have
169 established a stratigraphic framework, including the platform architecture and sedimentology
170 (Lehrmann et al., 2001; Lehrmann et al., 2005; Lehrmann et al., 1998; Li et al., 2012; Minzoni et
171 al., 2013) and age constraints from biostratigraphy, geochronology, and $\delta^{13}\text{C}$ chemostratigraphy
172 (Krull et al., 2004; Lehrmann et al., 2006; Lehrmann et al., 2015). Paleontological studies in the
173 GBG have been critical for determining the nature and timing of the biotic recovery from the end-
174 Permian mass extinction (Chen et al., 2013; Payne et al., 2006a; Payne et al., 2006b; Payne et al.,
175 2011; Song et al., 2011; Song et al., 2012b). In addition, numerous geochemical studies on
176 environmental conditions during the extinction have been conducted at the GBG (Algeo et al.,
177 2013; Brennecka et al., 2011; Lau et al., 2016; Meyer et al., 2011; Payne et al., 2010; Song et al.,
178 2013; Song et al., 2014; Song et al., 2012a; Sun et al., 2012).

179 Exceptional exposure of the platform permits measurement of stratigraphic sections and
180 collection of high-resolution sample sets recording the full interval from platform initiation during
181 the latest Permian to drowning and termination during the Late Triassic (Figures 1, 2). At Dajiang
182 (N25°33'59", E106°39'36"), a 2500 m-thick shallow-marine section (intertidal to tens of meters
183 water depth) in the platform interior, the uppermost Permian fossiliferous limestone is overlain by
184 8 to 16 m of thrombolitic microbialite at the Permian/Triassic transition (Lehrmann et al., 2003).
185 Lower Triassic strata continue with ~50 m of thin-bedded lime mudstone and ~100 m of overlying
186 oolitic dolo-grainstone. The Induan-Olenekian boundary is located at the start of ~180 m of

187 peritidal cyclic limestone, which is overlain by ~700 m of pervasively dolomitized peritidal facies
188 containing the Lower-Middle Triassic boundary (Lehrmann et al., 2001). During the Middle and
189 Late Triassic, the GBG accumulated vertically, forming high-relief escarpments along the platform
190 margin. Possibly rimmed by reefs that later collapsed along the platform margin, the platform
191 resembled an atoll with a lagoon in the platform interior. Strata consist of 600 m of bioturbated
192 molluscan-peloidal wackestones and packstones with occasional oncolites and domal
193 stromatolites. These wackestones and packstones are overlain by 400 m of shallowing-upward
194 fossiliferous peritidal cycles, after the platform returned to a flat-topped profile. Near the top of
195 the Middle Triassic, strata consist of skeletal-peloidal packstones that were deposited in subtidal
196 environments. Carbonate deposition was terminated by drowning of the platform and a higher
197 influx from siliciclastic sediments in the Carnian substage of the Late Triassic (Lehrmann et al.,
198 1998; Lehrmann et al., 2007).

199 In this study, we analyzed a suite of 45 new samples for $\delta^{44/40}\text{Ca}$ from the Dajiang section.
200 Combined with data previously published by Payne et al. (2010), the Ca isotopic record for Dajiang
201 includes data from 69 samples (refer to Table 1 for details).

202

203 *2.1.2 Taşkent, Turkey*

204 To determine whether variations in $\delta^{44/40}\text{Ca}$ are globally reproducible, we also analyzed
205 limestone samples from the Aladag Nappe, Turkey. This region was located along the western
206 Tethys (Figure 1), and is an allochthonous block that was thrust over the autochthonous series of
207 the Tauride block during the Eocene (Altiner and Özgül, 2001; Monod, 1977; Özgül, 1997). The
208 strata at Taşkent (N36°51', E32°30') contain a ~1000 m-thick shallow-marine mixed carbonate
209 and siliciclastic section that spans the Upper Permian to the Middle Triassic (Figure 3; Groves et
210 al., 2005; Richoz, 2006). The measured section begins with 48 m of uppermost Permian
211 fossiliferous lime packstone. The Permian/Triassic boundary is contained within a 0.5 m bed of
212 oolitic limestone overlain by 1 m of microbialite. Lowermost Triassic strata include 20 m of lime
213 mudstone overlain by 25 m of oolitic grainstone. The next ~600 m, which contain the remainder
214 of Lower Triassic stratigraphy and the Lower/Middle Triassic boundary, consist of alternating
215 beds of 10 cm- to 5 m-thick strata of fine-grained limestone, 0.5 to 2 m-thick strata of oolitic
216 packstone and grainstone, and <1 m- to 6-m thick strata of shale. Middle Triassic stratigraphy
217 continues with 11 m of massive lime wackestone-packstone, overlain by 132 m of covered shale.

218 Alternating massive lime packstone (strata of 3 m to 27 m thickness, with some oolitic beds) and
219 covered shale (strata of 1 m to 9 m thickness) continue for the remainder of the section.

220 The $\delta^{44/40}\text{Ca}$ record from Taškent comprises 60 samples. The geochronologic,
221 lithostratigraphic, and biostratigraphic framework for Dajiang and the GBG has been well studied
222 (Lehrmann et al., 2006; Lehrmann et al., 2015; Meyer et al., 2011), whereas the biostratigraphic
223 and geochronologic constraints at Taškent are less detailed (Altiner and Özgül, 2001; Monod,
224 1977; Özgül, 1997). We correlate Dajiang and Taškent using a combination of geochronology,
225 conodont and foraminiferan biostratigraphy, and $\delta^{13}\text{C}$ chemostratigraphy (Lau et al., 2016).

226

227 **2.2 Analytical Methods**

228 Carbon and oxygen (O) isotope data and some elemental concentration data from Dajiang
229 were previously published by Payne et al. (2004) and (2010) and Meyer et al. (2011). Carbon and
230 O isotope data and some elemental concentration data for Taškent samples were previously
231 published by Lau et al. (2016). Additional trace metal concentrations were obtained from powders
232 dissolved with 1 N acetic acid and analyzed on an Inductively Coupled Plasma-Optical Emission
233 Spectrometer (ICP-OES) at Stanford University. Reproducibility was better than $\pm 5\%$ (2SD).

234 Twenty-eight samples from Dajiang and 20 samples from Taškent were analyzed for
235 $\delta^{44/40}\text{Ca}$ at the Center of Isotope Geochemistry (CIG) at the University of California, Berkeley. A
236 0.8 mm dental drill bit was used to produce at least 1 mg of carbonate powder per sample, targeting
237 micrite and avoiding areas of alteration, such as veins. After adding 1 mL of 1 N acetic acid to the
238 powder in a 1.5 mL centrifuge tube, the sample was digested overnight. After centrifuging to
239 separate the undigested residue, 0.5 mL of the supernatant was removed and dried down in a
240 Savillex™ beaker. The sample was re-dissolved in 3 N nitric acid (HNO_3). An aliquot (equivalent
241 to 30 μg of Ca) was decanted and 280 μL of Ca double spike was added. The spiked samples
242 contained approximately 3 μg of ^{42}Ca and ^{48}Ca and yielded a final $^{42}\text{Ca}/^{44}\text{Ca}$ ratio of ~ 2.5 . After
243 drying down to completion, the sample was re-dissolved in 3 N HNO_3 , and Ca was separated from
244 Sr and other matrix elements using ~ 100 mL of element-specific DGA Eichrom Technologies
245 resin. Purified samples were dried down and re-dissolved in 3 N HNO_3 . Approximately 3 μg of Ca
246 was loaded onto a zone-refined Re filament (as part of a double filament assembly), treated with
247 3 N H_3PO_4 , and analyzed using a Thermo-Fisher Triton multi-collector thermal ionization mass
248 spectrometer (TIMS) in the CIG following methods described in Fantle and Higgins (2014). At

249 least two aliquots per sample were analyzed. Calcium isotope values are reported relative to Bulk
250 Silicate Earth (BSE) ($^{40}\text{Ca}/^{44}\text{Ca} = 47.162$ and $^{42}\text{Ca}/^{44}\text{Ca} = 0.31221$), which has a value of -0.9‰
251 relative to modern seawater and 1‰ relative to SRM-915a (Fantle and Tipper, 2014). Replicates
252 of SRM-915a had a mean $\delta^{44/40}\text{Ca}$ of $-1.06 \pm 0.15\text{‰}$ (2SD), within the expected range.

253 The remaining 17 samples from Dajiang and 40 from Taškent were analyzed at GEOMAR,
254 Helmholtz Centre for Ocean Research Kiel, following methods described in Griffith et al. (2008)
255 and Heuser et al. (2002). Sample powders produced as described above were dissolved in 2.5 M
256 hydrochloric acid (HCl). Following digestion, a $^{43}\text{Ca}/^{48}\text{Ca}$ double spike was added (Heuser et al.,
257 2002). After drying down to completion, the sample was re-dissolved in 2.5 N hydrochloric acid
258 (HCl) for separation using pre-washed cation exchange resin (BioRad AG50W). Purified samples
259 were dried down and re-dissolved in 2.5 N HCl and loaded with a Ta_2O_5 activator on zone-refined
260 Re single filaments in a double filament assembly. Calcium isotope analyses were performed on a
261 Triton TIMS at GEOMAR following methods described in Heuser et al. (2002). Three aliquots
262 per sample were analyzed and $\delta^{44/40}\text{Ca}$ values are reported relative to BSE. An in-house CaF_2
263 standard was analyzed with each run and produced a mean of $0.14 \pm 0.1\text{‰}$. External precision is
264 calculated as 2 standard deviations (2σ) from repeat measurements of the same sample solution,
265 and has a mean of 0.1‰ .

266

267 3. RESULTS

268 3.1 Dajiang, GBG, south China

269 Combined with previously published data, the Dajiang $\delta^{44/40}\text{Ca}$ data exhibit three major
270 features (Figure 2). First, as described in Payne et al. (2010), there is a negative 0.4‰ excursion
271 at the Permian/Triassic boundary, where $\delta^{44/40}\text{Ca}$ values decrease from $\sim -0.3\text{‰}$ to -0.7‰ . From 90
272 m to 220 m, $\delta^{44/40}\text{Ca}$ values gradually return to baseline values. Second, $\delta^{44/40}\text{Ca}$ decreases by
273 0.3‰ and reaches a minimum of -0.5‰ at ~ 350 m. This negative excursion, which has not
274 previously been reported, is followed by a recovery to baseline values at ~ 500 m, and $\delta^{44/40}\text{Ca}$
275 values remain near the pre-extinction baseline until the Lower/Middle Triassic boundary. Third,
276 $\delta^{44/40}\text{Ca}$ values hover around a mean of $\sim 0.1\text{‰}$ for the remainder of the 2000 m of stratigraphic
277 section. Seventeen dolomitized samples fall in the stratigraphic range of 120 m to 180 m and 400
278 m to 1000 m, and have $\delta^{44/40}\text{Ca}$ values that are slightly but not significantly more positive than

279 nearby limestone samples. A t-test comparison of overlapping limestone and dolomite $\delta^{44/40}\text{Ca}$
280 data from the Smithian substage produces a mean difference of 0.2‰ and a p -value of 0.05.

281

282 **3.2 Taşkent, Turkey**

283 At Taşkent, $\delta^{44/40}\text{Ca}$ values exhibit a negative shift of -0.5‰ at the extinction horizon and
284 reach a minimum of -1.1‰, followed by a steady positive trend, reaching a maximum of -0.1‰ at
285 a stratigraphic height of ~200 m (Figure 3). At ~300 m, $\delta^{44/40}\text{Ca}$ values again decrease to values of
286 -0.9‰. Calcium isotope values then increase to -0.5‰ at ~400 m and remain relatively steady to
287 the end of the measured stratigraphic section. There are only three dolomitized samples at Taşkent.

288

289 **3.3 Combined records**

290 To facilitate comparison between the stratigraphic sections, we produced smoothing curves
291 for the Dajiang and Taşkent data sets (*smooth.spline* function in R). To capture the analytical
292 uncertainty, we assume a Gaussian distribution defined by the 2σ of each data point and used a
293 Monte Carlo routine to resample 200 times within these bounds (Fantle, 2010). The datasets
294 overlap during the Changhsingian, Induan and Olenekian stages (Figure 4). Due to dolomitization
295 of upper Smithian and Spathian (substages of the Olenekian) strata at Dajiang, only data from
296 Taşkent are available for this interval. Accordingly, there is limited Middle-Upper Triassic overlap
297 between these two sections. At the Permian/Triassic boundary, the $\delta^{44/40}\text{Ca}$ data show similar
298 trends and decrease in uppermost Permian strata followed by a return in Induan strata, although
299 the absolute values are offset by ~0.3 to 0.4‰. Within the Dienerian strata, the records diverge.
300 At Dajiang, $\delta^{44/40}\text{Ca}$ values exhibit a short-lived negative excursion of 0.3‰, whereas $\delta^{44/40}\text{Ca}$
301 values at Taşkent are similar to the pre-extinction values of that section. In the mid-Smithian,
302 $\delta^{44/40}\text{Ca}$ at Taşkent shifts to more negative values and remains at -0.5‰ for the remainder of the
303 section, through the Anisian interval. In contrast, $\delta^{44/40}\text{Ca}$ at Dajiang in the Smithian through the
304 Middle Triassic varies between -0.2 and 0.1‰, and is positively offset by 0.3 to 0.6‰ from
305 Taşkent.

306

307 **3.4 Geochemical indicators of alteration**

308 To determine the influence of dolomitization and/or diagenetic alteration on the $\delta^{44/40}\text{Ca}$
309 records at Dajiang and Taşkent, we measured or compiled $\delta^{18}\text{O}$, Mg/Ca, Mn/Sr, [Sr], and [Mn]

310 (Figure 5). Dolomitization increases the Mg/Ca ratios of carbonates, and $\delta^{18}\text{O}$ and Mn/Sr ratios
311 are useful indicators of diagenetic alteration by anoxic, Mn-enriched brines or ^{18}O - and Sr-depleted
312 meteoritic fluids (Brand and Veizer, 1980). Because our sites were located at opposite margins of
313 the Tethys Ocean, the post-depositional alteration regimes experienced by these sediments likely
314 differed. At Taškent, Induan $\delta^{18}\text{O}$ values have a mean of $-7 \pm 2\%$ (n=60; all confidence intervals
315 reported as 2SD), whereas mean $\delta^{18}\text{O}$ in contemporaneous samples at Dajiang is $-4 \pm 2\%$ (n=71).
316 In contrast, Mn/Sr ratios remain low for both sections, except for dolomitized samples and
317 Griesbachian thrombolitic or oolitic samples. The [Sr] and [Mn] are higher at Taškent than at
318 Dajiang. At Dajiang, [Sr] range from 34 to 1463 mg/kg, with a mean of 351 mg/kg (n=71), whereas
319 at Taškent, [Sr] range from 99 to 3779 mg/kg, with a mean of 1059 mg/kg (n=60). The [Mn] at
320 Dajiang have a mean of 87 mg/kg (n=71) and range from 2 to 1019 mg/kg, and [Mn] at Taškent
321 have a mean of 144 mg/kg (n=60) and range from 11 to 804 mg/kg.

322 To check for variation in $\delta^{44/40}\text{Ca}$ that could be explained entirely by alteration, we assessed
323 the correlation of $\delta^{44/40}\text{Ca}$ with $\delta^{18}\text{O}$, $\delta^{13}\text{C}$, Mg/Ca, Mn/Sr, [Sr], and [Mn] (Figure 6; Table 2). The
324 scatter plot of $\delta^{44/40}\text{Ca}$ versus $\delta^{18}\text{O}$ highlights a major difference between the two sections: the
325 Taškent carbonates have lower $\delta^{44/40}\text{Ca}$ with $\delta^{18}\text{O}$ values than the Dajiang carbonates, with little
326 overlap between these two sections. Correlations of $\delta^{44/40}\text{Ca}$ with $\delta^{18}\text{O}$ and [Mn] (Table 2) are
327 significant at Dajiang (n=69; Spearman's $\rho=0.34$, p -value <0.01 and $\rho=-0.31$, p -value=0.01,
328 respectively) but are not statistically significant at Taškent (n=60; $\rho=-0.13$, p -value=0.31 and
329 $\rho=0.19$, p -value=0.15, respectively) (Table 2). However, the directions of these correlations are
330 opposite to the predicted positive and negative correlations of $\delta^{44/40}\text{Ca}$ with $\delta^{18}\text{O}$ and [Mn],
331 respectively, assuming $\delta^{44/40}\text{Ca}$ trends to more positive values during diagenetic alteration at
332 equilibrium with seawater (Fantle and DePaolo, 2007) and greater depletion of ^{18}O and enrichment
333 of Mn from diagenetic interaction with anoxic fluids. At Taškent, correlation between $\delta^{44/40}\text{Ca}$ and
334 Mn/Sr, as a measure of exchange with Mn-enriched and Sr-depleted fluids (Brand and Veizer,
335 1980), is significant (n=60, $\rho=0.28$, p -value=0.03). However, Mn/Sr values are well below 1.0,
336 and thus are inconsistent with a high degree of alteration (Kaufman et al., 1993). There is no
337 significant correlation between $\delta^{44/40}\text{Ca}$ and Mn/Sr for Dajiang. Finally, $\delta^{44/40}\text{Ca}$ for both Dajiang
338 and Taškent exhibits significant negative correlations with [Sr]. Although carbonate [Sr] can be
339 modulated by diagenesis, it is subject to additional controls as discussed in detail below in 4.
340 *Discussion.*

341 The fabric of a carbonate rock affects the extent of diagenetic alteration because grain size
342 is roughly correlated with surface area, which affects the rate of dissolution. Specifically, larger
343 grain sizes generally have slower rates of dissolution (Walter and Morse, 1984), and thus may limit
344 diagenetic alteration. Matrix-supported limestones, which are dominated by smaller grain sizes
345 (*i.e.*, mudstones, wackestones), have greater porosity but lower permeability than grain-supported
346 ones (*i.e.*, grainstones and packstones), decreasing the ratio of water-to-rock exchanged (Enos and
347 Sawatsky, 1981). The dolomitized samples (Figure 6) from both sections have more positive $\delta^{18}\text{O}$
348 and $\delta^{44/40}\text{Ca}$ compositions than limestones. Along with thrombolitic (microbialite) samples,
349 samples that are dolomitized or grain-supported also have high Mn/Sr ratios, with dolostones
350 having especially low [Sr] and thrombolites having high [Mn]. Mudstones and wackestones have
351 lower $\delta^{18}\text{O}$ compositions and thus may be more altered. Oolites have high $\delta^{13}\text{C}$ values at Dajiang.
352 At Taşkent, oolites have more negative $\delta^{44/40}\text{Ca}$ compositions. Other than relatively positive
353 $\delta^{44/40}\text{Ca}$ values, packstones and grainstones do not differ from mudstones/wackestones in these
354 geochemical indices of diagenesis.

355

356 4. DISCUSSION

357 The $\delta^{44/40}\text{Ca}$ records from Dajiang, south China, and Taşkent, Turkey, differ in both their
358 temporal trends and their absolute values. Although the negative excursion of $\sim 0.3\text{‰}$ at the end-
359 Permian mass extinction at Dajiang (Payne et al., 2010) occurs also at Taşkent, the Taşkent $\delta^{44/40}\text{Ca}$
360 values are almost 0.4‰ more negative than those at Dajiang. A similar trend in $\delta^{44/40}\text{Ca}$ occurs in
361 hydroxyapatite conodont elements collected from Meishan, south China (Hinojosa et al., 2012).
362 Thus, the $\delta^{44/40}\text{Ca}$ trends appear to record secular changes in the global Ca cycle, but the observed
363 offset suggests that local effects have shifted absolute values. Through the remainder of the Early
364 and Middle Triassic, there is little evidence for large excursions. The Dajiang record contains a
365 second negative excursion of slightly smaller magnitude at ~ 251.4 Ma, which is not observed at
366 Taşkent. Instead, $\delta^{44/40}\text{Ca}$ values at Taşkent shift towards more negative values at 251.1 Ma but do
367 not return to pre-extinction values and remain consistently more negative than those from Dajiang,
368 with an offset ranging from 0.3 to 0.6‰.

369 The use of carbonate $\delta^{44/40}\text{Ca}$ data to infer trends in seawater composition assumes that the
370 fractionation factor between seawater and carbonate can be inferred, and that Ca is derived from
371 seawater. However, the degree to which our $\delta^{44/40}\text{Ca}$ data have been overprinted by local, syn-

372 depositional or post-depositional factors needs to be considered. We use the relationship between
373 the $\delta^{44/40}\text{Ca}$ and [Sr] to distinguish between these factors. From this framework, we propose a
374 model that combines isotopic and elemental change during recrystallization with differences in
375 initial carbonate mineralogy to explain the observed trends.

376

377 **4.1 Post-depositional processes and potential impact on $\delta^{44/40}\text{Ca}$ in carbonate rocks**

378 The original depositional $\delta^{44/40}\text{Ca}$ of bulk carbonates can be altered via various local syn-
379 depositional and post-depositional processes such that it no longer tracks seawater $\delta^{44/40}\text{Ca}$ (*e.g.*,
380 Fantle and Higgins, 2014; Fantle, 2015; Farkaš et al., 2016; Griffith et al., 2015; Husson et al.,
381 2015; Jost et al., 2014 and 2017). Bulk geochemical composition can be diagenetically altered
382 from precipitation of authigenic carbonate (cementation and reduction in porosity) or via
383 recrystallization (dissolution and replacement with no change in porosity). Diagenetic processes
384 are further differentiated by the source of fluids exchanging with the carbonate rock. Unlike the
385 original depositional $\delta^{44/40}\text{Ca}$ value, which is offset from seawater by ~ -1 to $\sim -1.7\%$ depending on
386 the polymorph of CaCO_3 that precipitates (*e.g.*, Gussone et al., 2005), the $\delta^{44/40}\text{Ca}$ value of
387 carbonates precipitated during recrystallization (including authigenic cements) reflects isotopic
388 equilibrium with porewater Ca, with little to no fractionation (DePaolo, 2011; Fantle and DePaolo,
389 2007; Fantle, 2015). Thus, the porewater source and its associated $\delta^{44/40}\text{Ca}$ influence the alteration
390 of $\delta^{44/40}\text{Ca}$ in carbonate rock.

391 For example, early marine diagenesis occurs within the upper sediment column (in which
392 sediments are not yet well cemented), where the Ca in carbonate sediments exchanges with
393 porewater in communication with seawater (*e.g.*, Berner 1980). Early diagenetic processes such as
394 dissolution of biogenic carbonates, ion exchange due to ammonium production, and organic
395 carbon remineralization may all result in porewater $\delta^{44/40}\text{Ca}$ values that are more negative than
396 seawater by 0.6 to 0.8‰ (Teichert et al., 2009). Subsequent authigenic CaCO_3 precipitation or
397 recrystallization at equilibrium—with little to no fractionation (DePaolo 2011; Fantle and
398 DePaolo, 2007; Fantle, 2015)—would result in a minor to negligible positive offset. Although
399 models of early marine diagenesis assume bottom waters diffuse into the sediments, advection of
400 seawater (in some cases on continental shelves mixed with groundwater) can be driven by
401 gradients in hydraulic head, density, and temperature (Whitaker and Smart, 1990). Exchange with
402 hydrothermal or burial diagenetic fluids (often reducing brines) occurs at depth in the sediment

403 column and often $>10^6$ years after initial deposition (*e.g.*, Moore, 1989). Meteoric diagenesis is
404 primarily driven by advection and can occur either during early diagenesis or much later if the
405 strata are subsequently uplifted. Although subaerial exposure occurred periodically at Dajiang and
406 Taškent during deposition of the strata, we do not observe correlations between $\delta^{44/40}\text{Ca}$ and
407 sequence boundaries (indicative of subaerial erosion surfaces; Figures 2 and 3).

408 In addition to interaction with fluids, the carbonate minerals themselves can undergo
409 localized structural changes that alter their geochemical and isotopic compositions. Although
410 “neomorphism” has been used broadly to refer to a change from an initial meta-stable carbonate
411 phase to stable low-magnesian calcite (LMC), in this paper we define this process as the closed-
412 system, solid-state transition of primary aragonite and high-magnesian calcite (HMC) to LMC in
413 the absence of exchange with porewaters (Machel, 1997). In contrast, we use “recrystallization”
414 to mean the dissolution and re-precipitation of carbonate minerals (that may include but does not
415 require a change in mineralogy) and can result in geochemical exchange with porewaters (Machel,
416 1997). Finally, the timing of dolomitization and its fluid source remain challenging to infer, but
417 numerous models indicate that both seawater and external fluids can be involved in this process
418 (*e.g.*, Land, 1985).

419

420 **4.2 Relationship between $\delta^{44/40}\text{Ca}$ and [Sr]**

421 *4.2.1 Conceptual models*

422 Numerous factors can affect carbonate $\delta^{44/40}\text{Ca}$ values and the extent to which they reflect
423 changes in seawater $\delta^{44/40}\text{Ca}$ (summarized in Table 3). In addition to diagenetic alteration as
424 described in the previous section, the original depositional $\delta^{44/40}\text{Ca}$ value depends on CaCO_3
425 mineralogy and the net kinetic fractionation factor. To determine the relative importance of these
426 factors, we focus on the observed relationship between $\delta^{44/40}\text{Ca}$ and [Sr]. Strontium concentrations
427 in carbonates can vary as a function of the size of the seawater Sr reservoir, which is controlled by
428 the mass balance between continental weathering, hydrothermal circulation, and carbonate
429 deposition (Goddéris and François 1995; Kump 1989; Steuber and Veizer, 2002). Assuming a
430 constant offset between carbonate and seawater $\delta^{44/40}\text{Ca}$, an invariant distribution coefficient for
431 Sr incorporation for each CaCO_3 polymorph, and a constant aragonite-to-calcite ratio, secular
432 variations in both the Ca and Sr seawater cycles should be reflected in the carbonate rock record
433 (Figure 7A).

434 Controls on the Ca kinetic fractionation factor between seawater and CaCO₃ (such as
435 precipitation rate) can also affect [Sr], producing an apparent inverse, linear relationship between
436 carbonate $\delta^{44/40}\text{Ca}$ and [Sr] (*e.g.*, Tang et al., 2008a and 2008b; Watkins et al., 2017; Figure 7B).
437 At equilibrium, Ca isotopes are not appreciably fractionated between CaCO₃ and aqueous Ca (*i.e.*,
438 $\Delta_{\text{c-s}} = \sim 0\%$) (Fantle and DePaolo, 2007; Jacobson and Holmden, 2008), implying that fractionation
439 arises from kinetic isotope effects and the relative rates of forward and backward reactions
440 (DePaolo, 2011; Tang et al., 2008a). This equilibrium fractionation factor was derived from
441 observations from deep-sea carbonate samples with estimated precipitation rates of $<10^{-17}$
442 mol/m²/s (Fantle and DePaolo, 2007). In contrast, inorganic calcite precipitated in the laboratory
443 at faster rates (between 10^{-8} and 10^{-5} mol/m²/s) is modeled to exhibit a small equilibrium
444 fractionation of -0.5 to -0.2‰ (DePaolo, 2011). Thus, theoretical considerations and experimental
445 evidence suggests that as precipitation rate increases, $\Delta_{\text{c-s}}$ also increases (*e.g.*, Tang et al., 2008a;
446 Watkins et al., 2017). We note that an inverse relationship between $\Delta_{\text{c-s}}$ and precipitation rates has
447 also been observed (Lemarchand et al., 2004; AlKhatib and Eisenhauer, 2017a) suggesting that
448 very minor perturbations in $\delta^{44/40}\text{Ca}$ arise from an acidification event (Komar and Zeebe, 2016).
449 Given the uncertainties in the relationship between the precipitation rate and $\Delta_{\text{c-s}}$, we use the Tang
450 et al. (2008a) relationship because their experimental methods minimized transport limitations
451 which complicate the relationship between rate and $\Delta_{\text{c-s}}$ (DePaolo, 2011). More impurities, such as
452 Sr, are incorporated at higher precipitation rates (*e.g.*, Tang et al., 2008b; DePaolo, 2011), although
453 in the presence of fluids with high Sr/Ca, calcite precipitation is inhibited by strain within the local
454 crystal lattice and increasing mineral solubility (Nielsen et al., 2013). If porewater Sr/Ca remains
455 constant (as would be the case for fluids derived from seawater), both the magnitude of $\Delta_{\text{c-s}}$ and
456 degree of Sr incorporation in carbonates (K_{Sr}) increase as precipitation rate increases, producing a
457 linear and inverse trend between [Sr] or Sr/Ca and $\delta^{44/40}\text{Ca}$ (Figure 7B; Farkaš et al., 2007 and
458 2016; Steuber and Buhl, 2006; Tang et al., 2008a and 2008b; Watkins et al., 2017). This correlation
459 is also predicted by modeling of inorganic calcite precipitation, where both $\Delta_{\text{c-s}}$ and K_{Sr} are
460 described as functions of precipitation and dissolution rates (DePaolo, 2011; Watkins et al., 2017).
461 Carbonate $\delta^{44/40}\text{Ca}$ and [Sr] also vary as a function of the CaCO₃ polymorph that is initially
462 precipitated, with aragonite and LMC as end-members. Because aragonite has a larger cation site
463 in its crystal lattice than calcite, aragonite is associated with higher [Sr] (*e.g.*, Kinsman, 1969).
464 Additionally, precipitation of aragonite results in a larger Ca isotope fractionation from seawater,

465 producing $\delta^{44/40}\text{Ca}$ values that are more negative than calcite (Gussone et al., 2005; Blättler et al.,
466 2012). Thus, variable mixtures of polymorphs could result in an inverse correlation between
467 $\delta^{44/40}\text{Ca}$ and [Sr] (Figure 7C; Farkaš et al., 2017). Although the initial aragonite-to-calcite ratio is
468 unknown because metastable aragonite and HMC transform into LMC during neomorphism, this
469 factor has been gaining favor as an explanation for $\delta^{44/40}\text{Ca}$ trends across the Shuram $\delta^{13}\text{C}$ anomaly
470 (Husson et al., 2015), the Hirnantian glaciation (Kimmig and Holmden, 2017), the end-Triassic
471 mass extinction (Jost et al., 2017), and the Phanerozoic (Blättler et al., 2012). Secular variation in
472 the aragonite-to-calcite ratio in global carbonate sediment has also been invoked to explain
473 Phanerozoic $\delta^{44/40}\text{Ca}$ seawater trends recorded in well-preserved biogenic calcite from
474 brachiopods, belemnites, and foraminifera (Farkaš et al., 2007).

475 Interaction with submarine groundwater, which generally has low [Sr], would result in
476 diagnostic patterns in $\delta^{44/40}\text{Ca}$ and [Sr] (orange arrow in Figure 7D; Holmden et al., 2012b).
477 Submarine groundwater discharge from local restriction is hypothesized to have decreased the
478 $\delta^{44/40}\text{Ca}$ composition and [Sr] of Hirnantian carbonate rocks relative to global seawater, resulting
479 in a positive relationship between $\delta^{44/40}\text{Ca}$ and [Sr] (Holmden et al., 2012a), although an updated
480 interpretation attributes this relationship to changes in the variations in aragonite precipitation
481 (Kimmig and Holmden, 2017). The effect of burial diagenesis on $\delta^{44/40}\text{Ca}$ in bulk carbonate rock
482 remains challenging to constrain as the effects of marine-derived fluids on carbonate $\delta^{44/40}\text{Ca}$ are
483 not well known. Interaction with Sr-rich hydrothermal fluids is predicted to produce an inverse
484 relationship between $\delta^{44/40}\text{Ca}$ and [Sr] (Figure 7D, purple arrow). The $\delta^{44/40}\text{Ca}$ of hydrothermal
485 fluids from the Mid-Atlantic Ridge and East Pacific Rise have $\delta^{44/40}\text{Ca}$ values $\sim 0.95\%$ lighter than
486 modern seawater (Amini et al., 2008; Schmitt et al., 2003), which could result in a small positive
487 shift during recrystallization at isotopic equilibrium (assumed to be near unity; Brown et al., 2013).
488 Similarly, deep porewaters (> 245 to 300 meters below seafloor) in interaction with oceanic
489 basement are depleted in ^{44}Ca relative to seawater (Teichert et al., 2009). In contrast, early
490 diagenetic recrystallization in the presence of seawater—assuming an equilibrium $\Delta_{\text{c-s}}$ of 0‰
491 (Fantle, 2015; Fantle and Higgins, 2014)—would instead result in a positive shift from the original
492 composition (Figure 7D, gray arrow).

493

494 *4.2.2 Comparison with Early-Middle Triassic $\delta^{44/40}\text{Ca}$ and [Sr] data*

495 Given the numerous factors that can potentially influence Ca and Sr in carbonate rocks and
496 their predicted relationships between $\delta^{44/40}\text{Ca}$ and [Sr], our records, along with literature data,
497 provide a means to examine the dominant controls on the $\delta^{44/40}\text{Ca}$ composition of carbonate rock.
498 Because the $\delta^{44/40}\text{Ca}$ and [Sr] data from Dajiang and Taškent do not co-vary (Figure 4), we
499 eliminate a secular change in seawater Ca and Sr (Figure 7A) as the principal factor controlling
500 the stratigraphic trends in these carbonate rocks. Although our data roughly exhibit an inverse
501 linear trend, we also consider a log-linear model where [Sr] is plotted on a logarithmic axis (Figure
502 8). We use standardized major axis (SMA) regression models (*sma* function in R) to evaluate the
503 quality of fit between the linear and log-linear models. Unlike more common least-squares linear
504 regression models, which assume one variable is the control and is known (usually plotted along
505 the x-axis), SMA models assume that neither variable is the control and that both have
506 measurement error. Using SMA, the inverse relationship between $\delta^{44/40}\text{Ca}$ and [Sr] (Figure 8), is
507 better described by a log-linear model (Spearman's $\rho=-0.71$, p -value <0.001) than a linear model.
508 Using the Aikake information criterion (AIC) to evaluate the quality of the regression, the AIC for
509 the log-linear fit is much lower than that for the linear fit ($\Delta\text{AIC}=-1902$) and further supports a
510 non-linear relationship. In contrast to the linear regression results, the log-linear SMA models are
511 nearly identical when performed for each section and suggest common controlling factors (Figure
512 8). In fact, a single, common SMA model for the entire dataset produces a better fit ($\Delta\text{AIC}=-81$)
513 than separate models for the two sections. The preference for a log-linear model suggests that a
514 non-linear process is producing Sr loss concurrently with an increase in $\delta^{44/40}\text{Ca}$.

515 The observed log-linear model relationship eliminates precipitation rate as a primary
516 control on our dataset because a linear relationship is both predicted and observed between K_{Sr} and
517 $\Delta_{\text{c-s}}$ when precipitation rate is the controlling variable (Figure 7B; DePaolo, 2011; Nielsen et al.,
518 2012; Tang et al., 2008a and 2008b; Watkins et al., 2017). Because CaCO_3 saturation state
519 fluctuated during this time interval (Baud et al., 2007; Pruss et al., 2006; Weidlich and Bernecker,
520 2001; Woods et al., 2009), changes in fractionation from variations in precipitation rate probably
521 occurred. However, the lack of a clear linear relationship (*e.g.*, Farkaš et al., 2016) suggests that
522 this was not the major factor in determining the [Sr] and $\delta^{44/40}\text{Ca}$ in our carbonate rocks. Mixing
523 between aragonite and calcite end-members results in a linear relationship between [Sr] and
524 $\delta^{44/40}\text{Ca}$ (Figure 7C); our observation of a log-linear relationship for [Sr] with $\delta^{44/40}\text{Ca}$ suggests
525 that local variation in the relative proportions of CaCO_3 end-members can only partially explain

526 the dataset. Open-system alteration under the influence of external sources such as groundwater
527 and burial fluids (Figure 7D) as principal controls on our data is also inconsistent with our data
528 because we observe neither a positive correlation nor an enrichment in Sr, respectively.
529 Furthermore, our statistical results (*section 3.4*) comparing $\delta^{44/40}\text{Ca}$ to diagenetic indicators show
530 that although we did find significant correlations of $\delta^{44/40}\text{Ca}$ with $\delta^{18}\text{O}$, [Mn], and Mn/Sr, the
531 direction of the correlation (Figure 6) is generally opposite to the expected relationship under
532 meteoric or burial diagenesis, or the influence of groundwater and local restriction. Thus,
533 diagenetic resetting with meteoric or reducing fluids is unlikely to fully account for the trends in
534 $\delta^{44/40}\text{Ca}$. Similarly, the absence of correlation between Mg/Ca and $\delta^{44/40}\text{Ca}$ argues against
535 dolomitization as a primary control on the $\delta^{44/40}\text{Ca}$ composition. Instead, we suggest that variation
536 in initial carbonate mineralogy through time and between stratigraphic sections (Figure 7C),
537 combined with alteration and exchange with porewater in communication with seawater, best
538 account for the offset between the sections (Figure 7D, gray arrow).

539

540 *4.2.3 Insights from a water-rock interaction model of exchange with seawater*

541 Because of the observed log-linear relationship between $\delta^{44/40}\text{Ca}$ and [Sr] (Figure 8), our
542 data cannot be fully explained by variations in the initial aragonite-to-calcite composition.
543 However, early diagenetic recrystallization superimposed on samples with differing initial
544 aragonite-to-calcite ratios can account for the pattern. An open-system water-rock interaction
545 model (based on Banner and Hanson, 1990; Figure 9, Table 4) shows that exchange with porewater
546 in communication with seawater results in a redistribution of isotopes towards a new equilibrium
547 (*e.g.*, Fantle and DePaolo, 2007) that matches our observations. This simple equilibrium reaction
548 model tracks the evolution of carbonate geochemical compositions with increasing interaction with
549 a seawater-derived fluid. In the model, we evaluate the evolution of carbonate [Sr] and $\delta^{44/40}\text{Ca}$ (as
550 well as $\delta^{13}\text{C}$ and $\delta^{18}\text{O}$ for context) as a function of N , or the cumulative water-to-rock ratio (by
551 mass), under the assumption that recrystallization occurs at equilibrium and thus $\Delta_{c-s} = 0$ ‰ (Fantle
552 and DePaolo, 2007). We also assume that the concentrations and isotopic compositions of the
553 elements of interest in porewaters are constant. Because recrystallization occurs rapidly in the
554 upper part of the sediment column (<30 m), this calculation illustrates the potential for the bulk
555 carbonate $\delta^{44/40}\text{Ca}$ and [Sr] values to vary from their initial compositions during equilibration with
556 porewater (Fantle, 2010; Fantle, 2015). Initial concentrations in the fluid and rock, their isotopic

557 compositions, and fractionation factors are shown in Figure 9A-D, and a summary of model
558 equations and parameters is presented in the Appendix and Table 4.

559 As recrystallization in equilibrium with porewaters proceeds, loss of Sr occurs more
560 quickly than resetting of $\delta^{44/40}\text{Ca}$, resulting in non-linear evolution in $\delta^{44/40}\text{Ca}$ versus [Sr] space
561 (Figure 9E, F). Under this scenario, the diagenetic trajectory of [Sr] and $\delta^{44/40}\text{Ca}$ better matches
562 the log-linear relationship than the other factors described earlier. Different initial aragonite-to-
563 calcite ratios also influence the diagenetic trajectory by shifting the starting bulk composition.
564 Importantly, initial linear correlation between [Sr] and $\delta^{44/40}\text{Ca}$ produced by variation in
565 precipitation rate alone (Figure 7B) would not provide a mixture of carbonate minerals with
566 differing susceptibility to early diagenetic alteration.

567 The diagenetic resetting of [Sr] and $\delta^{44/40}\text{Ca}$ implied by our model can be reconciled with
568 observations of fluid flow in modern carbonate platforms (*e.g.*, Whitaker and Smart, 1990). For
569 the water-rock ratios invoked by this model, an N of 1000 is equivalent to 1 L of water exchanged
570 for every gram of rock. Although the exact values of N predicted in our model can vary depending
571 on the parameterizations of the modeled system (*e.g.*, porosity; *cf.* Husson et al., 2015), the
572 important observation is the point at which each geochemical component is altered relative to the
573 others. Regardless of the uncertainty in N , the fluxes of water required are substantial, and would
574 be typical of advective rather than diffusive fluxes of seawater into pores. The recrystallization
575 suggested by the model likely occurred at relatively shallow depths: the primary $^{87}\text{Sr}/^{86}\text{Sr}$ marine
576 signatures preserved in these rocks (Schaal, 2014) indicates interaction with seawater-derived
577 early diagenetic fluids.. Seawater can be advected within shallow marine sediments through an
578 array of processes. For example, density flows driven by evaporative salinity gradients along a
579 carbonate platform can generate pore velocities compatible with the values of N predicted by our
580 model (Whitaker and Smart, 1990). To illustrate, assuming an initial porosity of 0.4 and a rock
581 density of 3 g/cm^3 , a gram of carbonate sediment would contain $\sim 0.2 \text{ mL}$ of pore volume (PV).
582 One liter of water exchange is equivalent to $\sim 5000 PV$. Because PV can be defined in terms of
583 fluid residence time, T :

$$584 \quad T = PV * L/V \quad (1)$$

585 where V is the pore velocity and L is the reaction length scale $\sim 0.69 \text{ cm/g}$ of rock, pore velocities
586 on the order of 10^{-1} to 10^1 cm/yr estimated from model simulations of salinity-driven density flows
587 (Jones et al., 2006; Kaufman, 1994; Simms, 1984) would produce porewater residence times of 1

588 to 100 years. Additionally, a density gradient within a carbonate platform can persist for 100 times
589 the duration of a salinity-driven fluid refluxing through the sediment (*i.e.*, latent reflux; Jones et
590 al., 2006). In comparison to these time scales that are reasonable for recrystallization, temperature-
591 driven Kohout flows and mixing driven by freshwater can pump seawater at Darcy velocities of
592 0.3-1 and 5-20 m/yr, respectively (Simms, 1984), fluxes too rapid for carbonate precipitation at
593 isotopic equilibrium. Although our proposed density-driven reflux flows are typically invoked in
594 models for dolomitization, reactive transport modeling suggests that slower rates of dolomitization
595 are generated when rates of reflux are also slow (Jones and Xiao, 2005). Thus, at slow advective
596 velocities, chemical alteration may potentially occur absent dolomitization.

597 In summary, the mechanism that can best model the log-linear relationship between [Sr]
598 and $\delta^{44/40}\text{Ca}$ is early diagenetic resetting from a range of initial aragonite-to-calcite CaCO_3
599 compositions. This allows for a common seawater $\delta^{44/40}\text{Ca}$ to be inferred at both stratigraphic
600 sections. The first-order hydrologic constraints imposed by our simple diagenetic model are
601 reasonable based on studies of fluid flow through modern carbonate platforms.

602

603 **4.3 Comparison of $\delta^{44/40}\text{Ca}$ records from Dajiang and Taşkent**

604 Although carbon and uranium require greater volumes of fluid exchange to be fully reset
605 than calcium (Figure 9B; Lau et al., 2017), the agreement between the U and C isotope records at
606 Dajiang and Taşkent (Lau et al., 2016) implies that diagenesis has not resulted in complete
607 geochemical alteration. Therefore, these samples may retain the long-term $\delta^{44/40}\text{Ca}$ value of the
608 carbonate rock. If secular variations in seawater $\delta^{44/40}\text{Ca}$ are also preserved in these samples, then
609 the temporal trends of the carbonate rock $\delta^{44/40}\text{Ca}$ should agree between Dajiang and Taşkent.
610 Though the $\delta^{44/40}\text{Ca}$ values show temporally cohesive trends with discernable temporal patterns
611 for individual sections, neither the pattern nor the absolute value match (Figure 4). A $\sim 0.4\%$
612 negative $\delta^{44/40}\text{Ca}$ excursion at the Permian/Triassic boundary is observed at both sections, but the
613 minimum $\delta^{44/40}\text{Ca}$ value at Dajiang is -0.7% compared to -1% at Taşkent. Late Smithian to
614 Carnian $\delta^{44/40}\text{Ca}$ values at both sections are relatively stable, but $\delta^{44/40}\text{Ca}$ values at Dajiang have a
615 mean of 0.0% whereas $\delta^{44/40}\text{Ca}$ at Taşkent have a mean of -0.5% . Although there is some
616 uncertainty in the correlation, the $\delta^{13}\text{C}$ chemostratigraphy takes advantage of the large and well-
617 defined positive and negative $\delta^{13}\text{C}$ perturbations in the Early Triassic. The negative $\delta^{44/40}\text{Ca}$
618 isotope shift at Dajiang corresponds to a positive $\delta^{13}\text{C}$ excursion (Figure 2), whereas the opposite

619 is true for Taškent (Figure 3). Thus, it is unlikely that the discrepancy between south China and
620 Turkey is primarily a factor of the age model and/or correlation.

621 This variability in carbonate $\delta^{44/40}\text{Ca}$ may be attributed to local environmental conditions,
622 which would also influence the mode of carbonate precipitation and rock fabric type (e.g., grain-
623 supported, matrix-supported, microbialite). The ANOVA results indicate that the $\delta^{44/40}\text{Ca}$ data are
624 not significantly different when grouped by fabric type at Taškent (Table 5). The opposite is
625 observed at Dajiang, as ANOVA results indicate that $\delta^{44/40}\text{Ca}$ is significantly associated with fabric
626 type (p -value <0.001 ; Table 5, Figure 10). Because $\delta^{44/40}\text{Ca}$ values in rocks with grain-supported
627 fabrics are significantly more positive than those with matrix-supported fabrics, a plausible
628 interpretation is that more permeable sediments at Dajiang experienced greater diagenetic
629 resetting. Below, we further explore how variability in local depositional environments may
630 explain the differences in the $\delta^{44/40}\text{Ca}$ values of our two sections.

631

632 4.3.1 Local environmental variations

633 We propose that variations in the original aragonite-to-calcite mineralogy are the most
634 plausible explanation for the isotopic differences between stratigraphic sections. If aragonite was
635 the dominant original CaCO_3 polymorph at Taškent whereas calcite was the dominant original
636 polymorph at Dajiang, one would expect higher [Sr] and Sr/Ca and more negative $\delta^{44/40}\text{Ca}$ at
637 Taškent, consistent with observations (Figure 8) and our recrystallization model (Figure 9).
638 Additionally, the ~ 0.3 to 0.6% offset in $\delta^{44/40}\text{Ca}$ between the two sections falls within the $\sim 0.5\%$
639 difference in fractionation factor between calcite and aragonite (Gussone et al., 2005) and,
640 therefore, can be explained by systematic differences in their original admixtures of CaCO_3
641 polymorphs. In other words, seawater $\delta^{44/40}\text{Ca}$ was the same during deposition (as expected), but
642 the precipitated carbonate $\delta^{44/40}\text{Ca}$ fell between an aragonite-dominated end-member with [Sr]
643 ~ 3000 mg/kg and $\delta^{44/40}\text{Ca} \sim -1\%$ and a calcite-dominated end-member with [Sr] ~ 400 mg/kg and
644 $\delta^{44/40}\text{Ca} \sim 0\%$. As noted in *section 4.2.2*, the combined data do not fall along the predicted linear
645 mixing curve between aragonite and calcite end-members (Figure 9E). It would be expected that
646 the linear regression lines for the two sections would overlap if the [Sr] and $\delta^{44/40}\text{Ca}$ of the CaCO_3
647 end members were similar for the two stratigraphic sections; this is not the case. Although local
648 carbonate mineralogy can only partially explain the relationship between $\delta^{44/40}\text{Ca}$ and [Sr], it can
649 explain the offset between the Dajiang and Taškent data.

650 The Ca isotope fractionation during CaCO₃ precipitation varies with temperature (*e.g.*,
651 AlKhatib and Eisenhauer, 2017a,b; Gussone et al., 2005; Marriott et al., 2004); however,
652 fractionation is driven by kinetic effects and temperature is not the primary control (Brown et al.,
653 2013; DePaolo, 2011; Nielsen et al., 2012). In any case, the difference in $\delta^{44/40}\text{Ca}$ between
654 stratigraphic sections is too large to be fully attributed to temperature differences. Given a positive
655 relationship between $\Delta_{\text{c-s}}$ and temperature of $\sim 0.02\text{‰}$ per °C (Gussone et al., 2005; Marriott et al.,
656 2004), the ~ 0.3 to 0.6‰ offset (Figure 4) implies that sea surface temperatures in Turkey were 15
657 to 25 °C colder than in South China. This range exceeds the variability in modern tropical sea
658 surface temperatures. Additionally, an increase in temperature coincident with the end-Permian
659 extinction horizon (Romano et al., 2013; Sun et al., 2012) would decrease precipitation rate and
660 $\Delta_{\text{c-s}}$, predicting a positive excursion in the $\delta^{44/40}\text{Ca}$ of the rocks—opposite of the observed pattern.

661 Calcium in groundwater can affect the $\delta^{44/40}\text{Ca}$ in coastal sites (Holmden et al., 2012b).
662 Both sections were situated in shallow-marine environments: Taşkent on an attached carbonate
663 ramp, and Dajiang in the interior of an isolated carbonate platform. In both environments,
664 freshwater—influenced by carbonate dissolution—may have mixed with seawater, resulting in
665 carbonates precipitated with a more negative $\delta^{44/40}\text{Ca}$ composition relative to seawater. This
666 hypothesis is supported by the relatively negative $\delta^{18}\text{O}$ values at Taşkent, potentially caused by
667 mixing with meteoric waters or resetting during recrystallization; but the high [Sr] at Taşkent does
668 not support the influence of Sr-depleted groundwater (Brand and Veizer, 1980). Additionally,
669 significant groundwater intrusion predicts large salinity gradients (Holmden et al., 2012b); in
670 contrast, the faunas at Dajiang and Taşkent are representative of normal marine salinities (Payne
671 et al., 2006b, 2007), indicating that the depositional environments of the studied stratigraphic
672 sections experienced open marine circulation. Hence, it is unlikely that groundwater is the primary
673 process contributing to the observed $\delta^{44/40}\text{Ca}$ differences.

674 Remineralization of organic matter within the upper sediment column can result in the
675 release of organically-bound ⁴⁰Ca into porewaters, driving bulk carbonate $\delta^{44/40}\text{Ca}$ to more
676 negative values (Teichert et al., 2009). It is unlikely that organic matter oxidation played an
677 important role at our sites because total organic carbon (TOC) contents for limestone samples are
678 generally very low, with a mean of 0.4% for Dajiang and 0.3% for Taşkent (Lau et al., 2016). Deep
679 fluids that have reacted with ocean crust would also have low [Sr] and ⁸⁷Sr/⁸⁶Sr (Teichert et al.,
680 2009), but our stratigraphic sections were deposited on continental crust and positive correlations

681 with $\delta^{44/40}\text{Ca}$ are not observed (Figure 6). Additionally, $^{87}\text{Sr}/^{86}\text{Sr}$ data from these sections are
682 normal marine to slightly radiogenic (Schaal, 2014).

683 A biological control on the fractionation factor of Ca is also improbable. In this scenario,
684 higher proportions of aragonitic sponges, molluscs, foraminifera, and echinoderms, which exert a
685 strong biological control on the precipitation rate of CaCO_3 , result in larger $\Delta_{\text{c-s}}$ than brachiopods,
686 red algae, and calcitic sponges, which either precipitate calcite skeletons or demonstrate a weaker
687 control on the precipitation rate (Blättler et al., 2012). The paucity of skeletal grains at both
688 sections, where the approximate rock area comprising skeletal material is on average less than 4%
689 (Table 6), and the $\delta^{44/40}\text{Ca}$ values for samples with >10% skeletal components are indistinct from
690 those with <10% (t-test p -value = 0.13). Thus, a change in vital effects is unlikely to be the primary
691 control on $\delta^{44/40}\text{Ca}$.

692

693 4.3.2 *Microfacies and petrographic observations*

694 To investigate differences in original CaCO_3 mineralogy between Dajiang and Taškent, we
695 collected petrographic data from thin sections to identify the prevalence of primary (*e.g.*, micrite,
696 skeletal), early diagenetic (*e.g.*, microcrystalline cement, recrystallized clasts), or burial diagenetic
697 (*e.g.*, sparry calcite) microfacies. We examined thin sections from a subset of samples (27 from
698 Dajiang and 10 from Taškent) and visually estimated the area of the thin section composed of each
699 microfacies type (Table 6).

700 This first-order analysis provides us with clear differences in sedimentation, porosity, and
701 degree of recrystallization between stratigraphic sections and through time. In general, micritic
702 facies compose a larger proportion of microfacies at Dajiang, followed by microcrystalline
703 cement. In fact, micrite composes a large proportion of almost all the examined thin sections from
704 above the Permian/Triassic boundary, which is dominated by early diagenetic microcrystalline
705 cements and burial diagenetic sparry calcite. The micrite directly above the boundary is distinct
706 from micrite in other intervals because it is a component of the microbial framework of the
707 boundary thrombolites (Payne et al., 2006b). Skeletal grains are limited at Dajiang above the end-
708 Permian extinction horizon. Micrite is also an important component of Taškent carbonates, but
709 these rocks contain a larger proportion of grains—mostly recrystallized peloids, ooids, and other
710 clasts—and are much more heterogeneous in composition among samples. At Taškent, micrite is
711 most dominant in strata bracketing the Permian/Triassic boundary, but is not a volumetrically

712 important component for the rest of the section. Hand sample observations for intervals without
713 associated thin sections also illustrate that ooids and peloids are common.

714 Differences in sedimentary fabrics may provide insight into the chemical differences
715 between Dajiang and Taškent. First, ooids and peloids are especially prevalent at Taškent (Groves
716 et al., 2005; Richoz, 2006) but are much more limited at Dajiang. Although we are unable to
717 determine the original mineralogy of these clasts at Taškent, giant ooids from the GBG were
718 initially aragonitic or bimineralic (Lehrmann et al., 2012; Payne et al., 2006a). This observation is
719 consistent with our hypothesis that aragonite-dominated CaCO_3 precipitation could have been a
720 controlling factor on $\Delta_{\text{c-s}}$ and therefore differences in $\delta^{44/40}\text{Ca}$ (e.g., Kimmig and Holmden, 2017).
721 Second, the greater proportion of grain-supported lithologies at Taškent favor very early
722 cementation of aragonite—also supported by high [Sr] that indicate precipitation from seawater-
723 like fluids.

724 Dajiang $\delta^{44/40}\text{Ca}$ values are comparable to modern inorganic calcite (Blättler et al., 2012).
725 Petrographic observations and evidence for aragonitic seas (Stanley, 2006) indicate that inorganic
726 calcite is unlikely to have precipitated in this section for the entire time interval. Therefore, these
727 data could also be influenced by a reset of $\delta^{44/40}\text{Ca}$ to more positive compositions during
728 recrystallization. Tukey-Kramer statistical results (Table 5) are consistent with this hypothesis:
729 $\delta^{44/40}\text{Ca}$ values in matrix-supported samples are 0.29‰ more negative than grain-supported
730 samples (Figure 10). Early diagenetic recrystallization has been invoked to explain a positive 0.15-
731 0.8‰ shift in $\delta^{44/40}\text{Ca}$ (Fantle and DePaolo, 2007; Griffith et al., 2015). The magnitude of this
732 offset is predicted to increase with lower sedimentation rates because this would increase the
733 residence time of the carbonate sediments at the depths at which porewater pH decreases from
734 aerobic respiration, which can result in open-system diagenesis and a positive shift in $\delta^{44/40}\text{Ca}$
735 (Griffith et al., 2015). However, the shallow-marine environment of our studied sections is
736 characterized by high sedimentation rates. Despite occasional depositional hiatuses, we do not
737 observe evidence for positive excursions associated with these events at either section. Therefore,
738 it is most plausible that the generally more negative $\delta^{44/40}\text{Ca}$ values at Taškent are a function of
739 original aragonite-to-calcite ratios, but some of the temporal variations are due to recrystallization,
740 controlled by carbonate fabric type. Additionally, because changes in saturation state can produce
741 variations in precipitation rate, the effect of saturation state on precipitation rate may also partially
742 explain some of the variability in our $\delta^{44/40}\text{Ca}$ data (e.g., Silva-Tamayo, in review).

743

744 **4.4 Other carbonate $\delta^{44/40}\text{Ca}$ records**

745 An inverse relationship between [Sr] and $\delta^{44/40}\text{Ca}$ was previously observed for Ediacaran
746 carbonates from Australia (Husson et al., 2015), Ordovician carbonates from the western United
747 States (Holmden et al., 2012a), Upper Silurian carbonates from the Czech Republic (Farkaš et al.,
748 2016), and Triassic/Jurassic carbonates from Italy (Jost et al., 2017). Similar to the model
749 presented herein, Husson et al. (2015) propose that the log-linear relationship between [Sr] and
750 $\delta^{44/40}\text{Ca}$ in the Ediacaran Wonoka Formation spanning the Shuram negative $\delta^{13}\text{C}$ excursion falls
751 within an array defined by mixing between calcite and aragonite end-members with various
752 degrees of Sr loss. The combination of our data and model illustrates that although multiple
753 sections do not exhibit the same absolute value of $\delta^{44/40}\text{Ca}$, this difference can be attributed to
754 different mixtures of primary CaCO_3 polymorphs that fall along similar diagenetic trajectories.

755 To determine if a common mechanism explains both data reported herein and previously
756 published observations from other localities spanning numerous geological periods, we compiled
757 previously published $\delta^{44/40}\text{Ca}$ data measured in shallow-marine carbonate rocks that also evaluated
758 Sr concentrations or ratios (Figure 11). In addition to the studies mentioned above, these include
759 Ediacaran carbonates from China (Sawaki et al., 2014), Ordovician carbonates from Canada
760 (Holmden, 2009), Permian carbonates from Turkey and China (Jost et al., 2014), and
761 Permian/Triassic carbonates from Oman and Italy (Silva-Tamayo, in review). Core-top sediments
762 deposited in shallow waters (Fantle and Higgins, 2014), which have undergone only very early
763 diagenesis, are also included. Although there are several additional studies of $\delta^{44/40}\text{Ca}$ in carbonate
764 rock or core-top sediments, these studies lack data on [Sr] and thus are not useful for this exercise.

765 The compiled $\delta^{44/40}\text{Ca}$ data exhibit a correlation with [Sr] similar to the data presented in
766 this study, with a significant inverse correlation (Spearman's $\rho = -0.64$, p -value < 0.001), despite
767 the vast differences in paleogeographic location and time interval. A log-linear SMA regression
768 model (Figure 11B) is statistically better than a linear SMA model (Figure 11A; $\Delta\text{AIC} = -8806$;
769 Table A.1). Correlations between $\delta^{44/40}\text{Ca}$ and Sr/Ca ratios are better modeled using a linear
770 relationship (Figure 11C, D; Table A.1), but the converse is true for correlations with Sr/(Mg+Ca)
771 ratios (Figure 11E, F). However, given the limited number of datasets reporting these ratios, it is
772 unclear what might explain the differences in correlation between [Sr] and normalized [Sr].

773 The ubiquitous log-linear relationship of $\delta^{44/40}\text{Ca}$ with [Sr] suggests that the major control
774 on bulk shallow-marine $\delta^{44/40}\text{Ca}$ composition in carbonates since the Neoproterozoic is a
775 combination of initial carbonate mineralogy and subsequent recrystallization. The individual
776 Ediacaran datasets (Sawaki et al., 2014; Husson et al., 2015), the Triassic/Jurassic carbonates (Jost
777 et al., 2017), and the non-dolomitized Ordovician carbonates (Holmden et al., 2012a) are also
778 better described by a log-linear than a linear regression model (see Table A.1 for statistics). The
779 comparable regression slopes for most of these datasets (that are also similar to the regression for
780 the compilation) may indicate a relatively consistent shallow marine diagenetic regime through
781 time.

782 There are exceptions to the inverse log-linear correlation that suggest additional local
783 factors played a larger role than early diagenetic recrystallization in determining the $\delta^{44/40}\text{Ca}$ of
784 carbonate sediments at some sites. First, the positive correlation between Sr/Ca and $\delta^{44/40}\text{Ca}$ in
785 Middle-Late Ordovician carbonates from Saskatchewan is interpreted as mixing between
786 dolomitized and non-dolomitized end-members (Holmden, 2009). Second, Upper Silurian
787 carbonate $\delta^{44/40}\text{Ca}$ and [Sr] values fall along a linear mixing line with a slope in agreement with
788 the experimentally determined dependence of the kinetic fractionation factor on the precipitation
789 rate (Farkaš et al., 2016). Finally, there is no significant correlation between $\delta^{44/40}\text{Ca}$ and [Sr] for
790 the Permian dataset (Jost et al., 2014). Thus, although early diagenetic recrystallization appears to
791 be the dominant control in many published datasets, the influence of many other local factors can
792 become more important and cannot be ignored.

793

794 **4.5 Implications for interpreting changes in the global Ca cycle**

795 This study highlights the challenges of reconstructing secular variation in seawater $\delta^{44/40}\text{Ca}$
796 from bulk carbonate rock samples. In many instances, the expected coupling between C and Ca
797 cycles and their isotopic compositions appears to have been erased or heavily overprinted (Griffith
798 et al., 2015). Our findings demonstrate that the $\delta^{44/40}\text{Ca}$ of carbonate rocks is controlled by three
799 major processes: the $\delta^{44/40}\text{Ca}$ of contemporaneous seawater, the proportions of the two major
800 CaCO_3 polymorphs, and the degree of resetting during recrystallization. The similarities in the log-
801 linear relationship of $\delta^{44/40}\text{Ca}$ and [Sr] between our Permian/Triassic records and data spanning
802 selected intervals across the past ~650 million years suggest that the last two factors may have
803 been dominant through the Phanerozoic, and the nearly identical slopes imply that such processes

804 were common from the Late Permian through the Middle Triassic. Because mineralogy and
805 recrystallization greatly influenced bulk carbonate $\delta^{44/40}\text{Ca}$, these local effects present a challenge
806 in reconstructing changes in seawater $\delta^{44/40}\text{Ca}$ using bulk carbonate rock, as these factors may
807 obscure the temporal patterns. For example, the uncorrelated $\delta^{44/40}\text{Ca}$ data at Dajiang and Taškent
808 after the Griesbachian substage appear to predominantly reflect local controls.

809 In samples where mineralogy and recrystallization are the most dominant controls on
810 carbonate $\delta^{44/40}\text{Ca}$, it may be possible to account for the effect of variable CaCO_3 mineralogy and
811 diagenesis, and broadly estimate secular changes in seawater $\delta^{44/40}\text{Ca}$. Seawater [Sr] has
812 undoubtedly changed over the Phanerozoic (Richter et al., 1992; Steuber and Veizer, 2002), and
813 partitioning of Sr into carbonates is a function of organism growth and calcification rate (Stoll and
814 Schrag, 1998) in addition to the CaCO_3 polymorph, and thus is variable through time. However,
815 comparing the range of $\delta^{44/40}\text{Ca}$ values for a given [Sr] should provide a general sense of how
816 seawater $\delta^{44/40}\text{Ca}$ varied among the studied time intervals. In other words, if partitioning of Sr is
817 assumed to be constant over the Phanerozoic, varying seawater $\delta^{44/40}\text{Ca}$ would result in vertical
818 shifts in the regression intercept. This intercept does not hold geologic meaning, but can be
819 interpreted as normalized carbonate $\delta^{44/40}\text{Ca}$ with overprinting of mineralogy and recrystallization
820 removed. Thus, SMA intercepts for each dataset in Figure 11B (assuming a generally similar
821 diagenetic regime such that the data are well-represented by a negative regression) can be
822 compared to each other. Indeed, despite the differences between $\delta^{44/40}\text{Ca}$ data from Dajiang and
823 Taškent, their SMA intercepts are similar (Figure 8B), consistent with precipitation from seawater
824 with a shared $\delta^{44/40}\text{Ca}$ value.

825 To test this estimation, we used Phanerozoic $\delta^{44/40}\text{Ca}$ records hypothesized to reflect
826 predominantly aragonite or calcite precipitation, based on Mg/Ca ratios. In the calcitic seas of the
827 early Paleozoic, Mg/Ca ratios and inferred seawater $\delta^{44/40}\text{Ca}$ values are lower than intervals of
828 aragonitic seas (Blättler et al., 2012; Farkaš et al., 2007; Le Houedec et al., 2017; Stanley, 2006).
829 The regression intercepts of the log-linear models also mirror this trend, suggesting that first-order
830 variations in seawater $\delta^{44/40}\text{Ca}$ can be preserved in bulk carbonate rocks (Figure 12; Table A.1).
831 For example, the intercept is more negative during the calcitic seas in the Ordovician (Holmden et
832 al., 2009) than for the aragonitic seas in the Triassic to early Jurassic (this study; Jost et al., 2017).
833 The intercepts of Neoproterozoic datasets are more negative than in the Phanerozoic, but it is
834 difficult to test whether this agrees with seawater $\delta^{44/40}\text{Ca}$ in an inferred calcite seabecause

835 seawater Mg/Ca is less well constrained (Husson et al., 2015; Sawaki et al., 2014). Thus, first-
836 order secular trends in seawater $\delta^{44/40}\text{Ca}$ may be recovered despite diagenetic overprinting. We
837 caution that at this point, these corrections for mineralogy and recrystallization are only qualitative
838 with large uncertainties (Table A.1), and quantitative estimates are beyond the scope of this paper.
839 Although the assumption made here that partitioning of Sr into carbonates was invariant is
840 simplistic, this assumption and the sensitivity of the result to this assumption are testable in the
841 case that quantitative interpretation is desired.

842 An important observation of the present study is that the absolute values of $\delta^{44/40}\text{Ca}$ differ
843 substantially between two coeval stratigraphic sections. Because the 0.3‰ negative shift at the
844 end-Permian extinction boundary is reproduced at geographically disparate areas and between
845 different minerals (Hinojosa et al., 2012), we infer that this excursion reflects a change in seawater
846 chemistry that dominates local and post-depositional factors. However, the absolute values and
847 patterns higher in the section reveal significant heterogeneity in $\delta^{44/40}\text{Ca}$ and suggest that local
848 factors can make interpretation between stratigraphic sections challenging. The $\delta^{44/40}\text{Ca}$ record at
849 Dajiang—which is more positive than at Taškent—is most likely explained by more prevalent
850 aragonite precipitation at Taškent than at Dajiang, which would result in a larger $\Delta_{\text{c-s}}$ – reflected
851 by greater [Sr] and more negative $\delta^{44/40}\text{Ca}$ values. It is probable that the carbonates experienced
852 varying degrees of resetting during recrystallization, as supported by geochemical and
853 petrographic observations. Our findings emphasize the importance of collecting bulk carbonate
854 $\delta^{44/40}\text{Ca}$ data from multiple stratigraphic sections across geographic areas to evaluate the
855 importance of the many processes that can affect the fidelity of this proxy.

856

857 5. CONCLUSIONS

858 Because fluctuations in seawater $\delta^{44/40}\text{Ca}$ are primarily influenced by imbalances in the
859 calcium cycle, calcium isotopes hold promise for elucidating patterns in the coupled C and Ca
860 cycles. However, numerous factors can cause the $\delta^{44/40}\text{Ca}$ value recorded in carbonate sediments
861 and rocks to deviate from the contemporaneous seawater $\delta^{44/40}\text{Ca}$ composition. In this study, we
862 test the utility of carbonate $\delta^{44/40}\text{Ca}$ to constrain C and Ca cycling by comparing $\delta^{44/40}\text{Ca}$ in two
863 stratigraphic sections that span the Upper Permian to Middle Triassic. We do not find covarying
864 shifts in $\delta^{44/40}\text{Ca}$ in our two sections above the reproducible negative excursion at the
865 Permian/Triassic boundary. Instead, recrystallization and CaCO_3 mineralogy both contribute to

866 control the $\delta^{44/40}\text{Ca}$ value of our bulk carbonates and any signal of changes in seawater $\delta^{44/40}\text{Ca}$
867 composition has not been preserved. We suggest that any changes in seawater carbonate
868 chemistry—and the subsequent changes in carbonate $\delta^{44/40}\text{Ca}$ —were either too small to be
869 preserved, or were overprinted by these other factors. Although other records (*e.g.*, conodonts)
870 may prove useful to providing these constraints in future studies, our results support the hypothesis
871 that $\delta^{13}\text{C}$ perturbations were not driven by changing carbonate chemistry, but instead changing
872 redox conditions and organic carbon burial (Lau et al., 2016).

873 Although they appear to show little agreement in absolute $\delta^{44/40}\text{Ca}$ value as well as temporal
874 trend, they both exhibit the same systematic relationship with [Sr]—specifically, an inverse
875 correlation between $\log([\text{Sr}])$ and $\delta^{44/40}\text{Ca}$. This log-linear relationship can be explained using a
876 model of water-rock interaction of early diagenetic recrystallization from variable aragonite-to-
877 calcite ratios in the original sediment, precipitated from seawater with the same $\delta^{44/40}\text{Ca}$ and [Sr].
878 These factors of original mineralogy and water-rock interaction play a dominant role in the bulk
879 carbonate $\delta^{44/40}\text{Ca}$ value at these sites. This interpretation is further supported by a comparable
880 relationship between $\log([\text{Sr}])$ and $\delta^{44/40}\text{Ca}$ in compiled core-top shallow-marine carbonate
881 sediments and rocks spanning the past 600 million years. Despite overprinting by local factors,
882 first-order temporal trends in carbonate $\delta^{44/40}\text{Ca}$ can be informative of seawater chemistry and
883 secular trends in seawater $\delta^{44/40}\text{Ca}$ may be reconstructed from bulk carbonate records.

884

885 **Acknowledgements:** This research was supported by National Science Foundation Continental
886 Dynamics Grant EAR-0807475, American Chemical Society Petroleum Research Fund Grant
887 52457-ND2, and National Aeronautics and Space Administration Grant NNX09AN67G to
888 J.L.P., and an ARCS Fellowship, the GSA Gretchen L. Blechschmidt Award, and the AAPG
889 David Worthington Named Grant to K.V.L. The isotopic spike used in this research was supplied
890 by the United States Department of Energy Office of Science by the Isotope Program in the
891 Office of Nuclear Physics. We thank Guangchao Li, Tom Owens, and Hailun (Cindy) Ni for
892 assistance in the laboratory, and three anonymous reviewers for helpful suggestions that
893 improved this manuscript.

894

895 **References**

- 896 Algeo, T.J., Hinnov, L., Moser, J., Maynard, J.B., Elswick, E., Kuwahara, K., Sano, H., 2010. Changes in productivity
897 and redox conditions in the Panthalassic Ocean during the latest Permian. *Geology* 38, 187-190.
- 898 Algeo, T.J., Henderson, C.M., Tong, J., Feng, Q., Yin, H., Tyson, R.V., 2013. Plankton and productivity during the
899 Permian–Triassic boundary crisis: An analysis of organic carbon fluxes. *Global and Planetary Change* 105,
900 52-67.
- 901 Algeo, T.J., Kuwahara, K., Sano, H., Bates, S., Lyons, T., Elswick, E., Hinnov, L., Ellwood, B., Moser, J., Maynard,
902 J.B., 2011. Spatial variation in sediment fluxes, redox conditions, and productivity in the Permian-Triassic
903 Panthalassic Ocean. *Palaeogeography, Palaeoclimatology, Palaeoecology* 308, 65-83.

904 AlKhatib, M., Eisenhauer, A., 2017. Calcium and strontium isotope fractionation in aqueous solutions as a function
905 of temperature and reaction rate; I. Calcite. *Geochimica et Cosmochimica Acta* 209, 296-319.

906 AlKhatib, M., Eisenhauer, A., 2017. Calcium and strontium isotope fractionation during precipitation from aqueous
907 solutions as a function of temperature and reaction rate; II. Aragonite. *Geochimica et Cosmochimica Acta*
908 209, 320-342.

909 Altiner, D., Özgül, N., 2001. Carboniferous and Permian of the allochthonous terranes of the Central Tauride Belt,
910 southern Turkey, *PaleoForams 2001*, International Conference on Paleozoic Benthic Foraminifera, 20-24
911 August 2001, Guidebook., Ankara, p. 35.

912 Amini, M., Eisenhauer, A., Böhm, F., Fietzke, J., Bach, W., Garbeschönberg, D., Rosner, M., Bock, B., Lackschewitz,
913 K., Hauff, F., 2008. Calcium isotope ($\delta^{44/40}\text{Ca}$) fractionation along hydrothermal pathways, Logatchev field
914 (Mid-Atlantic Ridge, 14°45' N). *Geochimica et Cosmochimica Acta* 72, 4107-4122.

915 Atudorei, V., 1999. Constraints on the Upper Permian to Upper Triassic marine carbon isotope curve, Case studies
916 from the Tethys. University of Lausanne, p. 160.

917 Banner, J.L., Hanson, G.N., 1990. Calculation of simultaneous isotopic and trace element variations during water-
918 rock interaction with applications to carbonate diagenesis. *Geochimica et Cosmochimica Acta* 54, 3123-
919 3137.

920 Baud, A., Richoz, S., Pruss, S., 2007. The lower Triassic anachronistic carbonate facies in space and time. *Global and*
921 *Planetary Change* 55, 81-89.

922 Bergmann, K.D., Grotzinger, J.P., Fischer, W.W., 2013. Biological Influences on Seafloor Carbonate Precipitation.
923 *Palaios* 28, 99-115.

924 Berner, 1980. *Early Diagenesis: A Theoretical Approach*. Princeton University Press.

925 Blättler, C.L., Henderson, G.M., Jenkyns, H.C., 2012. Explaining the Phanerozoic Ca isotope history of seawater.
926 *Geology* 40, 843-846.

927 Blättler, C.L., Jenkyns, H.C., Reynard, L.M., Henderson, G.M., 2011. Significant increases in global weathering
928 during Oceanic Anoxic Events 1a and 2 indicated by calcium isotopes. *Earth and Planetary Science Letters*
929 309, 77-88.

930 Böhm, F., Gussone, N., Eisenhauer, A., Dullo, W.-C., Reynaud, S., Paytan, A., 2006. Calcium isotope fractionation
931 in modern scleractinian corals. *Geochimica et Cosmochimica Acta* 70, 4452-4462.

932 Brand, U., Veizer, J., 1980. Chemical Diagenesis of a Multicomponent Carbonate System--1: Trace Elements. *Journal*
933 *of Sedimentary Petrology* 50, 1219-1236.

934 Brayard, A., Bucher, H., Escarguel, G., Flueau, F., Bourquin, S., Galfetti, T., 2006. The Early Triassic ammonoid
935 recovery: Paleoclimatic significance of diversity gradients. *Palaeogeography, Palaeoclimatology,*
936 *Palaeoecology* 239, 374-395.

937 Brayard, A., Escarguel, G., Bucher, H., Monnet, C., Brühwiler, T., Goudemand, N., Galfetti, T., Guex, J., 2009. Good
938 Genes and Good Luck: Ammonoid Diversity and the End-Permian Mass Extinction. *Science* 325, 1118-1121.

939 Brazier, J.-M., Suan, G., Tacail, T., Simon, L., Martin, J.E., Mattioli, E., Balter, V., 2015. Calcium isotope evidence
940 for dramatic increase of continental weathering during the Toarcian oceanic anoxic event (Early Jurassic).
941 *Earth and Planetary Science Letters* 411, 164-176.

942 Brennecke, G.A., Herrmann, A.D., Algeo, T.J., Anbar, A.D., 2011. Rapid expansion of oceanic anoxia immediately
943 before the end-Permian mass extinction. *Proceedings of the National Academy of Sciences* 108, 17631-
944 17634.

945 Brown, S.T., Kennedy, B.M., DePaolo, D.J., Hurwitz, S., Evans, W.C., 2013. Ca, Sr, O and D isotope approach to
946 defining the chemical evolution of hydrothermal fluids: Example from Long Valley, CA, USA. *Geochimica*
947 *et Cosmochimica Acta* 122, 209-225.

948 Burgess, S.D., Bowring, S.A., 2015. High-precision geochronology confirms voluminous magmatism before, during,
949 and after Earth's most severe extinction. *Science Advances* 1, 1-14.

950 Chen, Y., Twitchett, R.J., Jiang, H., Richoz, S., Lai, X., Yan, C., Sun, Y., Liu, X., Wang, L., 2013. Size variation of
951 conodonts during the Smithian-Spathian (Early Triassic) global warming event. *Geology* 41, 823-826.

952 Chen, Z.-Q., Benton, M.J., 2012. The timing and pattern of biotic recovery following the end-Permian mass extinction.
953 *Nature Geoscience* 5, 375-383.

954 Clapham, M.E., Payne, J.L., 2011. Acidification, anoxia, and extinction: A multiple logistic regression analysis of
955 extinction selectivity during the Middle and Late Permian. *Geology* 39, 1059-1062.

956 Clarkson, M.O., Kasemann, S.A., Wood, R.A., Lenton, T.M., Daines, S.J., Richoz, S., Ohnemüller, F., Meixner, A.,
957 Poulton, S.W., Tipper, E.T., 2015. Ocean acidification and the Permo-Triassic mass extinction. *Science* 348,
958 229-232.

959 Cui, Y., Kump, L.R., Ridgwell, A., 2013. Initial assessment of the carbon emission rate and climatic consequences

960 during the end-Permian mass extinction. *Palaeogeography, Palaeoclimatology, Palaeoecology* 389, 128-136.

961 DePaolo, D.J., 2004. Calcium Isotopic Variations Produced by Biological, Kinetic, Radiogenic and Nucleosynthetic

962 Processes. *Reviews in Mineralogy* 55, 255-288.

963 DePaolo, D.J., 2011. Surface kinetic model for isotopic and trace element fractionation during precipitation of calcite

964 from aqueous solutions. *Geochimica et Cosmochimica Acta* 75, 1039-1056.

965 De La Rocha, C.L., DePaolo, D.J., 2000. Isotopic Evidence for Variations in the Marine Calcium Cycle Over the

966 Cenozoic. *Science* 289, 1176-1178.

967 Du Vivier, A.D.C., Jacobson, A.D., Lehn, G.O., Selby, D., Hurtgen, M.T., Sageman, B.B., 2015. Ca isotope

968 stratigraphy across the Cenomanian–Turonian OAE 2: Links between volcanism, seawater geochemistry,

969 and the carbonate fractionation factor. *Earth and Planetary Science Letters* 416, 121-131.

970 Enos, P., Sawatsky, L.H., 1981. Pore networks in Holocene carbonate sediments. *Journal of Sedimentary Petrology*

971 51, 961-985.

972 Fantle, M.S., 2010. Evaluating the Ca isotope proxy. *American Journal of Science* 310, 194-230.

973 Fantle, M.S., 2015. Calcium isotopic evidence for rapid recrystallization of bulk marine carbonates and implications

974 for geochemical proxies. *Geochimica et Cosmochimica Acta* 148, 378-401.

975 Fantle, M.S., DePaolo, D.J., 2005. Variations in the marine Ca cycle over the past 20 million years. *Earth and Planetary*

976 *Science Letters* 237, 102-117.

977 Fantle, M.S., DePaolo, D.J., 2007. Ca isotopes in carbonate sediment and pore fluid from ODP Site 807A: The

978 $\text{Ca}^{2+}(\text{aq})$ -calcite equilibrium fractionation factor and calcite recrystallization rates in Pleistocene sediments.

979 *Geochimica et Cosmochimica Acta* 71, 2524-2546.

980 Fantle, M.S., Higgins, J., 2014. The effects of diagenesis and dolomitization on Ca and Mg isotopes in marine platform

981 carbonates: Implications for the geochemical cycles of Ca and Mg. *Geochimica et Cosmochimica Acta* 142,

982 458-481.

983 Fantle, M.S., Maher, K.M., DePaolo, D.J., 2010. Isotopic approaches for quantifying the rates of marine burial

984 diagenesis. *Reviews of Geophysics* 48.

985 Fantle, M.S., Tipper, E.T., 2014. Calcium isotopes in the global biogeochemical Ca cycle: Implications for

986 development of a Ca isotope proxy. *Earth-Science Reviews* 129, 148-177.

987 Farkaš, J., Böhm, F., Wallmann, K., Blenkinsop, J., Eisenhauer, A., Vangeldern, R., Munnecke, A., Voigt, S., Veizer,

988 J., 2007. Calcium isotope record of Phanerozoic oceans: Implications for chemical evolution of seawater and

989 its causative mechanisms. *Geochimica et Cosmochimica Acta* 71, 5117-5134.

990 Farkaš, J., Frýda, J., Holmden, C., 2016. Calcium isotope constraints on the marine carbon cycle and CaCO_3 deposition

991 during the late Silurian (Ludfordian) positive $\delta^{13}\text{C}$ excursion. *Earth and Planetary Science Letters* 451, 31-

992 40.

993 Farkaš, J., Frýda, J., Holmden, C., 2017. Corrigendum to “Calcium isotope constraints on the marine carbon cycle and

994 CaCO_3 deposition during the late Silurian (Ludforidan) positive $\delta^{13}\text{C}$ excursion”. *Earth and Planetary Science*

995 *Letters*, in press.

996 Foster, W.J., Twitchett, R.J., 2014. Functional diversity of marine ecosystems after the Late Permian mass extinction

997 event. *Nature Geoscience* 7, 233-238.

998 Georgiev, S., Stein, H.J., Hannah, J.L., Bingen, B., Weiss, H.M., Piasecki, S., 2011. Hot acidic Late Permian seas

999 stifled life in record time. *Earth and Planetary Science Letters* 310, 389-400.

1000 Goddérís, Y., François, L.M., 1995. The Cenozoic evolution of the strontium and carbon cycles: relative importance

1001 of continental erosion and mantle exchange. *Chemical Geology* 126, 169-190.

1002 Gothmann, A.M., Bender, M.L., Blättler, C.L., Swart, P.K., Giri, S.J., Adkins, J.F., Stolarski, J., Higgins, J.A., 2016.

1003 Calcium isotopes in scleractinian fossil corals since the Mesozoic: Implications for vital effects and

1004 biomineralization through time. *Earth and Planetary Science Letters* 444, 205-214.

1005 Griffith, E.M., Fantle, M.S., Eisenhauer, A., Paytan, A., Bullen, T.D., 2015. Effects of ocean acidification on the

1006 marine calcium isotope record at the Paleocene–Eocene Thermal Maximum. *Earth and Planetary Science*

1007 *Letters* 419, 81-92.

1008 Griffith, E.M., Paytan, A., Caldeira, K., Bullen, T., Thomas, E., 2008. A Dynamic Marine Calcium Cycle During the

1009 Past 28 Million Years. *Science* 322, 1671-1674.

1010 Griffith, E.M., Paytan, A., Eisenhauer, A., Bullen, T.D., Thomas, E., 2011. Seawater calcium isotope ratios across the

1011 Eocene-Oligocene transition. *Geology* 39, 683-686.

1012 Groves, J.R., Altiner, D., Rettori, R., 2005. Extinction, survival, and recovery of Langenide foraminifers in the

1013 Permian-Triassic boundary interval, Central Taurides, Turkey. *Journal of Paleontology* 79, 1-38.

1014 Gussone, N., Böhm, F., Eisenhauer, A., Dietzel, M., Heuser, A., Teichert, B., Reitner, J., Worheide, G., Dullo, W.,

1015 2005. Calcium isotope fractionation in calcite and aragonite. *Geochimica et Cosmochimica Acta* 69, 4485-
1016 4494.

1017 Hallam, A., 1991. Why was there a delayed radiation after the end-Paleozoic extinctions? *Historical Biology* 5, 257-
1018 262.

1019 Heuser, A., Eisenhauer, A., Böhm, F., Wallmann, K., Gussone, N., Pearson, P.N., Nägler, T.F., Dullo, W.-C., 2005.
1020 Calcium isotope ($\delta^{44}\text{Ca}$) variations of Neogene planktonic foraminifera. *Paleoceanography* 20, 1-13.

1021 Heuser, A., Eisenhauer, A., Gussone, N., Bock, B., Hansen, B.T., Nagler, T.F., 2002. Measurement of calcium isotopes
1022 ($\delta^{44}\text{Ca}$) using a multicollector TIMS technique. *International Journal of Mass Spectrometry* 230, 385-397.

1023 Higgins, J.A., Fischer, W.W., Schrag, D.P., 2009. Oxygenation of the ocean and sediments: Consequences for the
1024 seafloor carbonate factory. *Earth and Planetary Science Letters* 284, 25-33.

1025 Hinojosa, J.L., Brown, S.T., Chen, J., DePaolo, D.J., Paytan, A., Shen, S.Z., Payne, J.L., 2012. Evidence for end-
1026 Permian ocean acidification from calcium isotopes in biogenic apatite. *Geology* 40, 743-746.

1027 Hippler, D., Kozdon, R., Darling, K.F., Eisenhauer, A., Nägler, T.F., 2009. Calcium isotopic composition of high-
1028 latitude proxy carrier *Neogloboquadrina pachyderma* (sin.). *Biogeosciences* 6, 1-14.

1029 Holmden, C., 2009. Ca isotope study of Ordovician dolomite, limestone, and anhydrite in the Williston Basin:
1030 Implications for subsurface dolomitization and local Ca cycling. *Chemical Geology* 268, 180-188.

1031 Holmden, C., Panchuk, K., Finney, S.C., 2012a. Tightly coupled records of Ca and C isotope changes during the
1032 Hirnantian glaciation event in an epeiric sea setting. *Geochimica et Cosmochimica Acta* 98, 94-106.

1033 Holmden, C., Papanastassiou, D.A., Blanchon, P., Evans, S., 2012b. $\delta^{44/40}\text{Ca}$ variability in shallow water carbonates
1034 and the impact of submarine groundwater discharge on Ca-cycling in marine environments. *Geochimica et*
1035 *Cosmochimica Acta* 83, 179-194.

1036 Horacek, M., Brandner, R., Abart, R., 2007a. Carbon isotope record of the P/T boundary and the Lower Triassic in
1037 the Southern Alps: Evidence for rapid changes in storage of organic carbon. *Palaeogeography,*
1038 *Palaeoclimatology, Palaeoecology* 252, 347-354.

1039 Horacek, M., Richoz, S., Brandner, R., Krystyn, L., Spötl, C., 2007b. Evidence for recurrent changes in Lower Triassic
1040 oceanic circulation of the Tethys: The $\delta^{13}\text{C}$ record from marine sections in Iran. *Palaeogeography,*
1041 *Palaeoclimatology, Palaeoecology* 252, 355-369.

1042 Husson, J.M., Higgins, J.A., Maloof, A.C., Schoene, B., 2015. Ca and Mg isotope constraints on the origin of Earth's
1043 deepest $\delta^{13}\text{C}$ excursion. *Geochimica et Cosmochimica Acta* 160, 243-266.

1044 Jacobson, A.D. and Holmden, C., 2008. $\delta^{44}\text{Ca}$ evolution in a carbonate aquifer and its bearing on the equilibrium
1045 isotope fractionation factor for calcite. *Earth and Planetary Science Letters* 270, 349-353.

1046 Jones, G.D., Whitaker, F.F., Smart, P.L., Sanford, W.E., 2006. Fate of reflux brines in carbonate platforms. *Geology*
1047 2002 30, 371-374.

1048 Jones, G.D., Xiao, Y., 2015. Dolomitization, anhydrite cementation, and porosity evolution in a reflux system: Insights
1049 from reactive transport models. *AAPG Bulletin* 89, 577-601.

1050 Jost, A.B., Bachan, A., van de Schootbrugge, B., Brown, S.T., DePaolo, D.J., Payne, J.L., 2017. Additive effects
1051 of acidification and mineralogy on calcium isotopes in Triassic/Jurassic boundary limestones. *Geochemistry,*
1052 *Geophysics, Geosystems* 18, 113-124.

1053 Jost, A.B., Mundil, R., He, B., Brown, S.T., Altiner, D., Sun, Y., DePaolo, D.J., Payne, J.L., 2014. Constraining the
1054 cause of the end-Guadalupian extinction with coupled records of carbon and calcium isotopes. *Earth and*
1055 *Planetary Science Letters* 396, 201-212.

1056 Kasemann, S.A., Pogue von Strandmann, P.A.E., Prave, A.R., Fallick, A.E., Elliott, T., Hoffmann, K.-H., 2014.
1057 Continental weathering following a Cryogenian glaciation: Evidence from calcium and magnesium isotopes.
1058 *Earth and Planetary Science Letters* 396, 66-77.

1059 Kaufman, A.J., Jacobsen, S.B., Knoll, A.H., 1993. The Vendian record of Sr and C isotopic variations in seawater:
1060 Implications for tectonics and paleoclimate. *Earth and Planetary Science Letters* 120, 409-430.

1061 Kaufman, J., 1994. Numerical models of fluid flow in carbonate platforms: Implications for dolomitization. *Journal*
1062 *of Sedimentary Research* A64, 128-139.

1063 Kiessling, W., Simpson, C., 2011. On the potential for ocean acidification to be a general cause of ancient reef crises.
1064 *Global Change Biology* 17, 56-67.

1065 Kimmig, S.R., Holmden, C., 2017. Multi-proxy geochemical evidence for primary aragonite precipitation in a tropical-
1066 shelf 'calcite sea' during the Hirnantian glaciation. *Geochimica et Cosmochimica Acta* 206, 254-272.

1067 Kinsman, D.J., 1969. Interpretation of Sr+2 Concentrations in Carbonate Minerals and Rocks. *Journal of Sedimentary*
1068 *Petrology* 39, 486-508.

1069 Knoll, A.H., Bambach, R.K., Payne, J.L., Pruss, S., Fischer, W.W., 2007. Paleophysiology and end-Permian mass
1070 extinction. *Earth and Planetary Science Letters* 256, 295-313.

1071 Komar, N., Zeebe, R.E., 2016. Calcium and calcium isotope changes during carbon cycle perturbations at the end-
1072 Permian. *Paleoceanography* 31, 115-130.

1073 Krull, E.S., Lehrmann, D.J., Druke, D., Kessel, B., Yu, Y., Li, R., 2004. Stable carbon isotope stratigraphy across the
1074 Permian–Triassic boundary in shallow marine carbonate platforms, Nanpanjiang Basin, south China.
1075 *Palaeogeography, Palaeoclimatology, Palaeoecology* 204, 297-315.

1076 Kump, L.R., 1989. Alternative Modeling Approaches to the Geochemical Cycles of Carbon, Sulfur, and Strontium
1077 Isotopes. *American Journal of Science* 289, 390-410.

1078 Land, L.S., 1985. The Origin of Massive Dolomite. *Journal of Geological Education* 33, 112-125.

1079 Lau, K.V., Maher, K., Altiner, D., Kelley, B.M., Kump, L.R., Lehrmann, D.J., Silva-Tamayo, J.C., Weaver, K.L., Yu,
1080 M., Payne, J.L., 2016. Marine anoxia and delayed Earth system recovery after the end-Permian extinction.
1081 *Proceedings of the National Academy of Sciences* 113, 2360-2365.

1082 Lau, K.V., Macdonald, F.A., Maher, K., Payne, J.L., 2017. Uranium isotope evidence for temporary ocean
1083 oxygenation in the aftermath of the Sturtian Snowball Earth. *Earth and Planetary Science Letters* 458, 282-
1084 292.

1085 Le Houedec, S., McCulloch, M., Trotter, J., Rankenburg, K. Conodont apatite $\delta^{88/86}\text{Sr}$ and $\delta^{44/40}\text{Ca}$ compositions and
1086 implications for the evolution of Palaeozoic to early Mesozoic seawater. *Chemical Geology* 453, 55-65.

1087 Lehrmann, D.J., Donghong, P., Enos, P., Minzoni, M., Ellwood, B.B., Orchard, M.J., Jiyan, Z., Jiayong, W., Dillett,
1088 P., Koenig, J., Steffen, K., Druke, D., Druke, J., Kessel, B., Newkirk, T., 2007. Impact of differential tectonic
1089 subsidence on isolated carbonate-platform evolution: Triassic of the Nanpanjiang Basin, south China. *AAPG*
1090 *Bulletin* 91, 287-320.

1091 Lehrmann, D.J., Enos, P., Payne, J.L., Montgomery, P., Wei, J., Yu, Y., Xiao, J., Orchard, M.J., 2005. Permian and
1092 Triassic depositional history of the Yangtze platform and Great Bank of Guizhou in the Nanpanjiang basin
1093 of Guizhou and Guangxi, south China. *Albertiana* 33, 167-184.

1094 Lehrmann, D.J., Minzoni, M., Li, X., Yu, M., Payne, J.L., Kelley, B.M., Schaal, E.K., Enos, P., 2012. Lower Triassic
1095 oolites of the Nanpanjiang Basin, south China: Facies architecture, giant ooids, and diagenesis—Implications
1096 for hydrocarbon reservoirs. *AAPG Bulletin* 96, 1389-1414.

1097 Lehrmann, D.J., Payne, J.L., Felix, S.V., Dillett, P.M., Wang, H., Yu, Y.Y., and Wei, J.Y., 2003. Permian-Triassic
1098 boundary sections from shallow-marine carbonate platforms of the Nanpanjiang basin, south China:
1099 Implications for oceanic conditions associated with the end-Permian extinction and its aftermath. *Palaios* 18,
1100 138-152.

1101 Lehrmann, D.J., Ramezani, J., Bowring, S.A., Martin, M.W., Montgomery, P., Enos, P., Payne, J.L., Orchard, M.J.,
1102 Hongmei, W., Jiayong, W., 2006. Timing of recovery from the end-Permian extinction: Geochronologic and
1103 biostratigraphic constraints from south China. *Geology* 34, 1053.

1104 Lehrmann, D.J., Stepchinski, L., Altiner, D., Orchard, M.J., Montgomery, P., Enos, P., Ellwood, B.B., Bowring, S.A.,
1105 Ramezani, J., Wang, H., 2015. An integrated biostratigraphy (conodonts and foraminifers) and
1106 chronostratigraphy (paleomagnetic reversals, magnetic susceptibility, elemental chemistry, carbon isotopes
1107 and geochronology) for the Permian–Upper Triassic strata of Guandao section, Nanpanjiang Basin, south
1108 China. *Journal of Asian Earth Sciences* 108, 117-135.

1109 Lehrmann, D.J., Wan, Y., Wei, J., Yu, Y., Xiao, J., 2001. Lower Triassic peritidal cyclic limestone: an example of
1110 anachronistic carbonate facies from the Great Bank of Guizhou, Nanpanjiang Basin, Guizhou province, South
1111 China. *Palaeogeography, Palaeoclimatology, Palaeoecology* 173, 103-123.

1112 Lehrmann, D.J., Wei, J., Enos, P., 1998. Controls on Facies Architecture of a Large Triassic Carbonate Platform: The
1113 Great Bank of Guizhou, Nanpanjiang Basin, South China. *Journal of Sedimentary Research* 68, 311-326.

1114 Lemarchand, D., Wasserbug, G.J., Papanastassiou, D.A., 2004. Rate-controlled calcium isotope fractionation in
1115 synthetic calcite. *Geochimica et Cosmochimica Acta* 68, 4665-4678.

1116 Li, X., Yu, M., Lehrmann, D.J., Payne, J.L., Kelley, B.M., Minzoni, M., 2012. Factors controlling carbonate platform
1117 asymmetry: Preliminary results from the Great Bank of Guizhou, an isolated Permian–Triassic Platform in
1118 the Nanpanjiang Basin, south China. *Palaeogeography, Palaeoclimatology, Palaeoecology* 315-316, 158-171.

1119 Loyd, S.J., Berelson, W.M., Lyons, T.W., Hammond, D.E., Corsetti, F.A., 2012. Constraining pathways of microbial
1120 mediation for carbonate concretions of the Miocene Monterey Formation using carbonate-associated sulfate.
1121 *Geochimica et Cosmochimica Acta* 78, 77-98.

1122 Machel, H.G., 1997. Recrystallization versus neomorphism, and the concept of ‘significant recrystallization’ in
1123 dolomite research. *Sedimentary Geology* 113, 161-168.

1124 Maher, K., Steefel, C.I., DePaolo, D.J., Viani, B.E., 2006. The mineral dissolution rate conundrum: Insights from
1125 reactive transport modeling of U isotopes and pore fluid chemistry in marine sediments. *Geochimica et*
1126 *Cosmochimica Acta* 70, 337-363.

- 1127 Marriott, C.S., Henderson, G.M., Belshaw, N.S., Tudhope, A.W., 2004. Temperature dependence of $\delta^7\text{Li}$, $\delta^{44}\text{Ca}$ and
 1128 Li/Ca during growth of calcium carbonate. *Earth and Planetary Science Letters* 222, 615-624.
- 1129 Meyer, K.M., Yu, M., Jost, A.B., Kelley, B.M., Payne, J.L., 2011. $\delta^{13}\text{C}$ evidence that high primary productivity
 1130 delayed recovery from end-Permian mass extinction. *Earth and Planetary Science Letters* 302, 378-384.
- 1131 Minzoni, M., Lehrmann, D.J., Payne, J.L., Enos, P., Yu, M., Wei, J., Kelley, B.M., Li, X., Schaal, E., Meyer, K.M.,
 1132 Montgomery, P., Goers, A., Wood, T., 2013. Triassic Tank: Platform Margin and Slope Architecture in Space
 1133 and Time, Nanpanjiang Basin, South China. *SEPM Special Publication* 105, 84-113.
- 1134 Monod, O., 1977. Recherches géologiques dans le Taurus occidental au Sud de Beysehir (Turquie) [Ph.D. thesis].
 1135 Université de Paris-Sud, Centre d'Orsay, p. 442.
- 1136 Moore, C.H., 1989. Carbonate Diagenesis and Porosity. *Developments in Sedimentology* Vol. 46. Elsevier Science
 1137 Publishing B.V.
- 1138 Nielsen, L.C., De Yoreo, J.J., DePaolo, D.J., 2013. General model for calcite growth kinetics in the presence of
 1139 impurity ions. *Geochimica et Cosmochimica Acta* 115, 100-114.
- 1140 Nielsen, L.C., DePaolo, D.J., De Yoreo, J.J., 2012. Self-consistent ion-by-ion growth model for kinetic isotopic
 1141 fractionation during calcite precipitation. *Geochimica et Cosmochimica Acta* 86, 166-181.
- 1142 Orchard, M.J., 2007. Conodont diversity and evolution through the latest Permian and Early Triassic upheavals.
 1143 *Palaeogeography, Palaeoclimatology, Palaeoecology* 252, 93-117.
- 1144 Özgül, N., 1997. Stratigraphy of the tectono-stratigraphic units in the region Bozkir-Hadim-Taşkent (northern central
 1145 Taurides) [in Turkish with English abstract]. *Mineral Research and Exploration Institute of Turkey (MTA)*
 1146 *Bulletin* 119, 113-174.
- 1147 Payne, J.L., Kump, L., 2007. Evidence for recurrent Early Triassic massive volcanism from quantitative interpretation
 1148 of carbon isotope fluctuations. *Earth and Planetary Science Letters* 256, 264-277.
- 1149 Payne, J.L., Lehrmann, D.J., Christensen, S., Wei, J., Knoll, A.H., 2006a. Environmental and Biological Controls on
 1150 the Initiation and Growth of a Middle Triassic (Anisian) Reef on the Great Bank of Guizhou, Guizhou
 1151 Province, China. *Palaaios* 21, 325-343.
- 1152 Payne, J.L., Lehrmann, D.J., Follett, D., Seibel, M., Kump, L.R., Riccardi, A., Altiner, D., Sano, H., Wei, J., 2007.
 1153 Erosional truncation of uppermost Permian shallow-marine carbonates and implications for Permian-Triassic
 1154 boundary events. *Geological Society of America Bulletin* 119, 771-784.
- 1155 Payne, J.L., Lehrmann, D.J., Wei, J., Knoll, A.H., 2006b. The Pattern and Timing of Biotic Recovery from the End-
 1156 Permian Extinction on the Great Bank of Guizhou, Guizhou Province, China. *Palaaios* 21, 63-85.
- 1157 Payne, J.L., Lehrmann, D.J., Wei, J., Orchard, M.J., Schrag, D.P., Knoll, A.H., 2004. Large perturbations of the carbon
 1158 cycle during recovery from the end-Permian extinction. *Science* 305, 506-509.
- 1159 Payne, J.L., Summers, M., Rego, B.L., Altiner, D., Wei, J., Yu, M., Lehrmann, D.J., 2011. Early and Middle Triassic
 1160 trends in diversity, evenness, and size of foraminifers on a carbonate platform in south China: implications
 1161 for tempo and mode of biotic recovery from the end-Permian mass extinction. *Paleobiology* 37, 409-425.
- 1162 Payne, J.L., Turchyn, A.V., Paytan, A., DePaolo, D.J., Lehrmann, D.J., Yu, M., Wei, J., 2010. Calcium isotope
 1163 constraints on the end-Permian mass extinction. *Proceedings of the National Academy of Sciences* 107, 8543.
- 1164 Pruss, S.B., Bottjer, D.J., Corsetti, F.A., Baud, A., 2006. A global marine sedimentary response to the end-Permian
 1165 mass extinction: Examples from southern Turkey and the western United States. *Earth-Science Reviews* 78,
 1166 193-206.
- 1167 Richoz, S., 2006. Stratigraphie et variations isotopiques du carbone dans le Permien supérieur et le Trias inférieur de
 1168 quelques localités de la Néotéthys (Turquie, Oman et Iran), Institut de Géologie et Paléontologie. Université
 1169 de Lausanne, Lausanne, Switzerland, p. 284.
- 1170 Richter, F.M., Rowley, D.B., DePaolo, D., 1992. Sr isotope evolution of seawater: the role of tectonics. *Earth and*
 1171 *Planetary Science Letters* 109, 11-23.
- 1172 Romano, C., Goudemand, N., Vennemann, T.W., Ware, D., Schneebeli-Hermann, E., Hochuli, P.A., Bruhwiler, T.,
 1173 Brinkmann, W., Bucher, H., 2013. Climatic and biotic upheavals following the end-Permian mass extinction.
 1174 *Nature Geoscience* 6, 57-60.
- 1175 Sawaki, Y., Tahata, M., Ohno, T., Komiya, T., Hirata, T., Maruyama, S., Han, J., Shu, D., 2014. The anomalous Ca
 1176 cycle in the Ediacaran ocean: Evidence from Ca isotopes preserved in carbonates in the Three Gorges area,
 1177 South China. *Gondwana Research* 25, 1070-1089.
- 1178 Schaal, E.K., 2014. Permian-Triassic Global Change: The Strontium Cycle and Body Size Evolution in Marine Clades.
 1179 Ph.D. dissertation, Stanford University.
- 1180 Schaal, E.K., Clapham, M.E., Rego, B.L., Wang, S.C., Payne, J.L., 2016. Comparative size evolution of marine clades
 1181 from the Late Permian through Middle Triassic. *Paleobiology* 42, 127-142.
- 1182 Schmitt, A.-D., Chabaux, F., Stille, P., 2003. The calcium riverine and hydrothermal isotopic fluxes and the oceanic

- 1183 calcium mass balance. *Earth and Planetary Science* 213, 503-518.
- 1184 Silva-Tamayo, J.C., Nägler, T.F., Sial, A.N., Nogueira, A., Kyser, K., Riccomini, C., James, N.P., Narbonne, G.M.,
 1185 Villa, I.M., 2010a. Global perturbation of the marine Ca isotopic composition in the aftermath of the
 1186 Marinoan global glaciation. *Precambrian Research* 182, 373-381.
- 1187 Silva-Tamayo, J.C., Nägler, T.F., Villa, I.M., Kyser, K., Vieira, L.C., Sial, A.N., Narbonne, G.M., James, N.P., 2010b.
 1188 Global Ca isotope variations in c. 0.7 Ga old post-glacial carbonate successions. *Terra Nova* 22, 188-194.
- 1189 Silva-Tamayo, J.C., Lau, K.V., Jost, A.B., Payne, J.L., Wignall, P.B., Newton, R.J., Eisenhauer, A., DePaolo, D.J.,
 1190 Brown, S.T., Maher, K., Lehmann, D.J., Altiner, D., Yu, M., Richoz, S., Paytan, A., accepted. Global
 1191 Perturbation of the Marine Calcium Cycle During the Permian-Triassic Transition. *GSA Bulletin*.
- 1192 Sime, N.G., De La Rocha, C.L., Galy, A., 2005. Negligible temperature dependence of calcium isotope fractionation
 1193 in 12 species of planktonic foraminifera. *Earth and Planetary Science Letters* 232, 51-66.
- 1194 Sime, N.G., De La Rocha, C.L., Tipper, E.T., Tripathi, A., Galy, A., Bickle, M., 2007. Interpreting the Ca isotope
 1195 record of marine biogenic carbonates. *Geochimica et Cosmochimica Acta* 71, 3979-3989.
- 1196 Simms, M., 1984. Dolomitization by groundwater-flow systems in carbonate platforms. *AAPG Bulletin* 34, 411-420.
- 1197 Skulan, J., DePaolo, D., Owens, T.L., 1997. Biological control of calcium isotopic abundances in the global calcium
 1198 cycle. *Geochimica et Cosmochimica Acta* 61, 2505-2510.
- 1199 Song, H.-J., Tong, J., Xiong, Y., Sun, D., Tian, L., Song, H.-Y., 2012a. The large increase of $\delta^{13}\text{C}$ carb-depth gradient
 1200 and the end-Permian mass extinction. *Science China Earth Sciences* 55, 1101-1109.
- 1201 Song, H.-J., Wignall, P.B., Chen, Z.-Q., Tong, J., Bond, D.P.G., Lai, X., Zhao, X., Jiang, H., Yan, C., Niu, Z., Chen,
 1202 J., Yang, H., Wang, Y., 2011. Recovery tempo and pattern of marine ecosystems after the end-Permian mass
 1203 extinction. *Geology* 39, 739-742.
- 1204 Song, H.-J., Wignall, P.B., Tong, J., Yin, H., 2012b. Two pulses of extinction during the Permian-Triassic crisis.
 1205 *Nature Geoscience* 6, 52-56.
- 1206 Song, H.-Y., Tong, J., Algeo, T.J., Horacek, M., Qiu, H., Song, H.-J., Tian, L., Chen, Z.-Q., 2013. Large vertical
 1207 $\delta^{13}\text{C}_{\text{DIC}}$ gradients in Early Triassic seas of the South China craton: Implications for oceanographic changes
 1208 related to Siberian Traps volcanism. *Global and Planetary Change* 105, 7-20.
- 1209 Song, H.-Y., Tong, J., Algeo, T.J., Song, H.-J., Qiu, H., Zhu, Y., Tian, L., Bates, S., Lyons, T.W., Luo, G., Kump,
 1210 L.R., 2014. Early Triassic seawater sulfate drawdown. *Geochimica et Cosmochimica Acta* 128, 95-113.
- 1211 Stanley, S.M., 2006. Influence of seawater chemistry on biomineralization throughout Phanerozoic time:
 1212 Paleontological and experimental evidence. *Palaeogeography, Palaeoclimatology, Palaeoecology* 232, 214-
 1213 236.
- 1214 Stanley, S.M., 2009. Evidence from ammonoids and conodonts for multiple Early Triassic mass extinctions.
 1215 *Proceedings of the National Academy of Sciences* 106, 15264-15267.
- 1216 Steuber, T., Buhl, D., 2006. Calcium-isotope fractionation in selected modern and ancient marine carbonates.
 1217 *Geochimica et Cosmochimica Acta* 70, 5507-5521.
- 1218 Steuber, T., Veizer, J., 2002. Phanerozoic record of plate tectonic control of seawater chemistry and carbonate
 1219 sedimentation. *Geology* 30, 1123-1126.
- 1220 Stoll, H.M., Schrag, D.P., 1998. Effects of Quaternary sea level cycles on strontium in seawater. *Geochimica et*
 1221 *Cosmochimica Acta* 62, 1107-1118.
- 1222 Sun, Y., Joachimski, M.M., Wignall, P.B., Yan, C., Chen, Y., Jiang, H., Wang, L., Lai, X., 2012. Lethally hot
 1223 temperatures during the Early Triassic greenhouse. *Science* 338, 366-370.
- 1224 Svensen, H., Planke, S., Polozov, A.G., Schmidbauer, N., Corfu, F., Podladchikov, Y.Y., Jamtveit, B., 2009. Siberian
 1225 gas venting and the end-Permian environmental crisis. *Earth and Planetary Science Letters* 277, 490-500.
- 1226 Tang, J., Dietzel, M., Böhm, F., Köhler, S.J., Eisenhauer, A., 2008a. $\text{Sr}^{2+}/\text{Ca}^{2+}$ and $^{44}\text{Ca}/^{40}\text{Ca}$ fractionation during
 1227 inorganic calcite formation: II. Ca isotopes. *Geochimica et Cosmochimica Acta* 72, 3733-3745.
- 1228 Tang, J., Köhler, S.J., Dietzel, M., 2008b. $\text{Sr}^{2+}/\text{Ca}^{2+}$ and $^{44}\text{Ca}/^{40}\text{Ca}$ fractionation during inorganic calcite formation: I.
 1229 Sr incorporation. *Geochimica et Cosmochimica Acta* 72, 3718-3732.
- 1230 Teichert, B.M.A., Gussone, N., Torres, M.E., 2009. Controls on calcium isotope fractionation in sedimentary
 1231 porewaters. *Earth and Planetary Science Letters* 279, 373-382.
- 1232 Tipper, E.T., Galy, A., Bickle, M.J., 2008. Calcium and magnesium isotope systematics in rivers draining the
 1233 Himalaya-Tibetan-Plateau region: Lithological or fractionation control? *Geochimica et Cosmochimica Acta*
 1234 72, 1057-1075.
- 1235 Tucker, M.E., Wright, V.P., 1990. *Carbonate Sedimentology*. Blackwell Scientific Publications, Oxford.
- 1236 Walter, L.M., Morse, J.W., 1984. Reactive surface area of skeletal carbonates during dissolution: Effect of grain size.
 1237 *Journal of Sedimentary Petrology* 54, 1081-1090.
- 1238 Watkins, J.M., DePaolo, D.J., Watson, E.B., 2017. Kinetic fractionation of non-traditional stable isotopes by diffusion

- 1239 and crystal growth reactions. *Reviews in Mineralogy and Geochemistry*, 82.
- 1240 Weidlich, O., Bernecker, M., 2011. Biotic carbonate precipitation inhibited during the Early Triassic at the rim of the
- 1241 Arabian Platform (Oman). *Palaeogeography, Palaeoclimatology, Palaeoecology* 308, 129-150.
- 1242 Whitaker, F.F., Smart, P.L., 1990. Active circulation of saline ground waters in carbonate platforms: Evidence from
- 1243 the Great Bahama Bank. *Geology* 18, 200-203.
- 1244 Woods, A.D., Bottjer, D.J., Mutti, M., Morrison, J., 1999. Lower Triassic large sea-floor carbonate cements: Their
- 1245 origin and a mechanism for the prolonged biotic recovery from the end-Permian mass extinction. *Geology*
- 1246 27, 645-648.
- 1247 Woods, A.D., 2014. Assessing Early Triassic paleoceanographic conditions via unusual sedimentary fabrics and
- 1248 features. *Earth-Science Reviews* 137, 6-18.
- 1249

1250 **Figure captions**

1251 Figure 1: Geologic setting. (A) Latest Permian-earliest Triassic paleogeographic locations for
1252 Dajiang (south China) and Taşkent (Turkey). (B) Cross section of the Great Bank of Guizhou,
1253 south China, showing simplified lithology and location of the Dajiang stratigraphic section in the
1254 platform interior. Modified from Lehrmann et al. (1998).

1255
1256 Figure 2: Dajiang stratigraphic section showing $\delta^{13}\text{C}$ data relative to Vienna Pee Dee Belemnite
1257 (VPDB) and $\delta^{44/40}\text{Ca}$ data relative to bulk silicate earth (BSE) and SRM-915a. Smoothing curve
1258 and confidence interval are produced using a spline smoothing fit and a Monte Carlo procedure.
1259 $\delta^{44/40}\text{Ca}$ error bars are 2σ from multiple analyses of the same sample. $\delta^{13}\text{C}$ data were previously
1260 published in Meyer et al. (2011) and $\delta^{44/40}\text{Ca}$ data includes values from Payne et al. (2010; open
1261 squares). Open gray points are dolomitized and excluded from the smoothing curve, and sequence
1262 boundaries are identified as “SB”.

1263
1264 Figure 3: Taşkent stratigraphic section showing $\delta^{13}\text{C}$ data relative to VPDB and $\delta^{44/40}\text{Ca}$ data
1265 relative to BSE and SRM-915a. Smoothing curve and confidence interval are produced using a
1266 spline smoothing fit and a Monte Carlo procedure. $\delta^{44/40}\text{Ca}$ error bars are 2σ from multiple analyses
1267 of the same sample. $\delta^{13}\text{C}$ data were previously published in Lau et al. (2016). Open gray points are
1268 dolomitized and excluded from the smoothing curve, and sequence boundaries are identified as
1269 “SB”.

1270
1271 Figure 4: Combined $\delta^{13}\text{C}$ and $\delta^{44/40}\text{Ca}$ from Dajiang (red circles) and Taşkent (blue triangles) from
1272 (A) the Late Permian to Late Triassic and (B) Early Triassic only (within the dashed lines in A).
1273 Smoothing curve and confidence interval are produced using a spline fit and a Monte Carlo
1274 procedure that incorporates the variability from error on the measurements. Gray, open points are
1275 dolomitized and excluded from the smoothing curve.

1276
1277 Figure 5: Combined $\delta^{13}\text{C}$, $\delta^{44/40}\text{Ca}$, $\delta^{18}\text{O}$, Mg/Ca, Mn/Sr, [Sr], and [Mn] data from Dajiang (red
1278 circles) and Taşkent (blue triangles) from the (A) Late Permian to Late Triassic and (B) Early
1279 Triassic only. Gray points are dolomitized. Ratios are $\text{mg kg}^{-1} / \text{mg kg}^{-1}$. Note log scale for [Sr]
1280 and [Mn].

1281
1282 Figure 6: Scatterplots of $\delta^{44/40}\text{Ca}$ vs. other geochemical data. Open circles are from Dajiang and
1283 open triangles are from Taşkent. Colors represent different carbonate rock fabric types as indicated
1284 in the legend. Note log axes.

1285
1286 Figure 7: Conceptual model depicting the relationship between $\delta^{44/40}\text{Ca}$ and [Sr] for seawater and
1287 carbonates for scenarios of: (A) mass flux imbalances in the seawater Ca and Sr cycles; (B)
1288 variations in the kinetic fractionation factor from a change in precipitation rate; (C) linear mixing
1289 between CaCO_3 polymorph end-members with distinct fractionation factors; and (D) post-

1290 deposition alteration from linear mixing with Sr-depleted submarine groundwaters, Sr-enriched
1291 burial brines, or diagenetic resetting with seawater. These factors are not mutually exclusive: for
1292 example, an acidification event would include both reduced CaCO₃ burial (panel A) and a smaller
1293 fractionation factor (panel B) that may counteract their effects on bulk carbonate $\delta^{44/40}\text{Ca}$.
1294

1295 Figure 8: Scatterplots of (A) $\delta^{44/40}\text{Ca}$ and [Sr] on a linear scale, (B) $\delta^{44/40}\text{Ca}$ and [Sr] on a log scale,
1296 (C) $\delta^{44/40}\text{Ca}$ and Sr/Ca on a linear scale, and (D) $\delta^{44/40}\text{Ca}$ and Sr/Ca on a log scale for Dajiang (red
1297 circles) and Taškent (blue triangles). A log-linear SMA model that describes the correlation in (B)
1298 is statistically better than the linear SMA model in (A) ($\Delta\text{AIC}=-1902$).
1299

1300 Figure 9: Evolution of (A) $\delta^{18}\text{O}$, (B) $\delta^{13}\text{C}$, (C) $\delta^{44/40}\text{Ca}$, and (D) [Sr] in carbonate sediments
1301 interacting with seawater using a water-rock interaction model modified from Banner and Hanson
1302 (1990). As N increases, a greater volume of water has passed through the modeled system. In (C)
1303 and (D), the evolution for sediments that are originally 50% calcitic and 50% aragonitic are plotted
1304 against the left-hand y-axis and the evolution for sediments that are originally 100% aragonitic are
1305 plotted against the right-hand y-axis. Assumed fluid and solid compositions are shown, and
1306 porosity is set at 40% with a rock density of 3 g/mL. Crossplot of modeled $\delta^{44/40}\text{Ca}$ and [Sr]
1307 overlain over data from Dajiang (circles) and Taskent (triangles), with arrows showing the path of
1308 recrystallization to calcite along (E) a linear [Sr] axis and (F) a logarithmic [Sr] axis. The
1309 recrystallization path for five initial aragonite-calcite mixtures are shown.
1310

1311 Figure 10: Boxplots of $\delta^{44/40}\text{Ca}$ and [Sr] grouped by carbonate fabric type for Dajiang (left, red)
1312 and Taškent (right, blue). Boxes are defined by the median, first quartile, and third quartile of the
1313 data, and the whiskers denote the interquartile range. $\delta^{44/40}\text{Ca}$ for Dajiang differ statistically
1314 depending on fabric type (Table 5), whereas $\delta^{44/40}\text{Ca}$ for Taskent do not. Grain-supported fabric
1315 types include grainstones, packstones, and oolites, and matrix-supported fabric types include
1316 wackestones and mudstones. The number of samples within each fabric type are shown below
1317 each boxplot in parentheses.
1318

1319 Figure 11: Scatterplots of $\delta^{44/40}\text{Ca}$ compared to (A, B) [Sr], (C, D) Sr/Ca, and (E, F) Sr/(Ca+Mg)
1320 compiled from previously published studies. Left panels are plotted on a linear scale and right
1321 panels are plotted on a logarithmic scale. Red circles are data from this study, whereas open
1322 symbols are from studies in carbonate rocks and blue triangles are data from shallow marine
1323 carbonate sediments. Data plotted from Silva-Tamayo et al. (in review) are from Oman and Italy.
1324 The standardized major axis regression for datasets that exhibit a statistically significant
1325 correlation are plotted, depending on whether the linear or log-linear models were a better fit.
1326

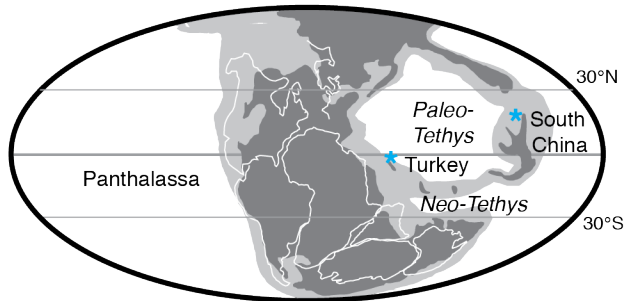
1327 Figure 12: Comparison of the intercept of log-linear regressions with inferred seawater $\delta^{44/40}\text{Ca}$
1328 through the Phanerozoic. (A) The intercepts from Table A.1 for datasets that have statistically
1329 significant log-linear relationships between [Sr] and $\delta^{44/40}\text{Ca}$ are plotted at the approximate

1330 midpoint of the dataset, with horizontal error bars showing the approximate range. Vertical error
 1331 bars are 1 SE. (1) Sawaki et al. (2014), (2) Husson et al. (2015), (3) Holmden et al. (2012a), (4)
 1332 this study, and (5) Jost et al. (2017). Intercepts for Holmden (2009) and Farkaš et al. (2016) are
 1333 not plotted because these datasets are primarily driven by dolomitization and kinetic reaction rates,
 1334 respectively. (B) Reconstruction of seawater $\delta^{44/40}\text{Ca}$ across the Phanerozoic, compiled by Blättler
 1335 et al. (2012; see references therein). Temporal ranges of inferred aragonite and calcite seas are
 1336 from Stanley (2006).

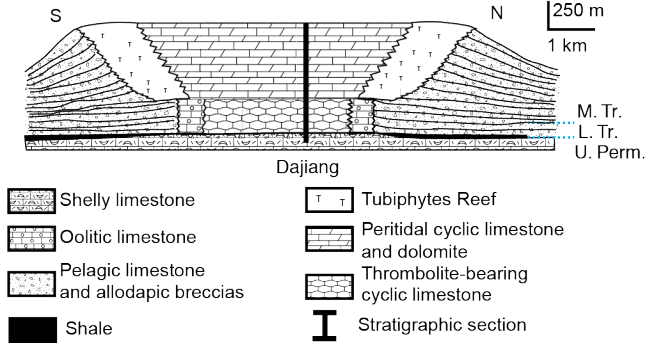
1337
 1338

Figure 1

A Paleogeographic setting

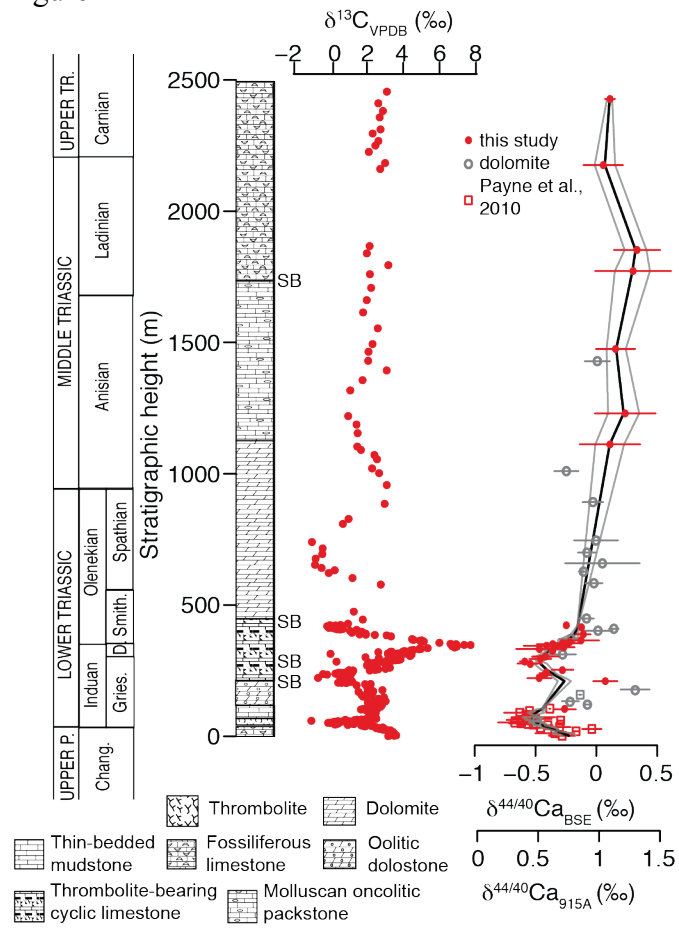


B Great Bank of Guizhou



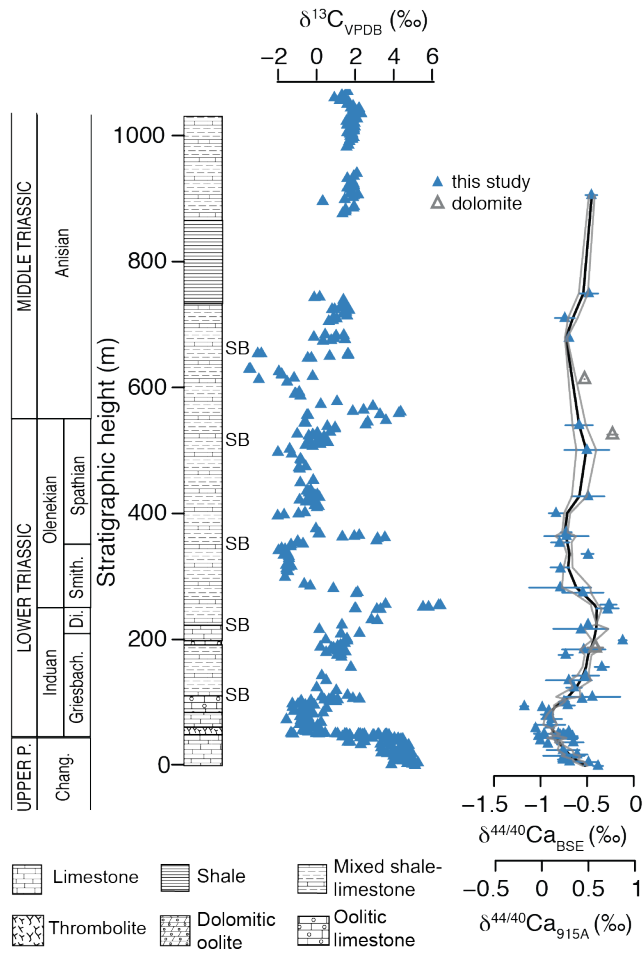
1339
 1340

1341 Figure 2



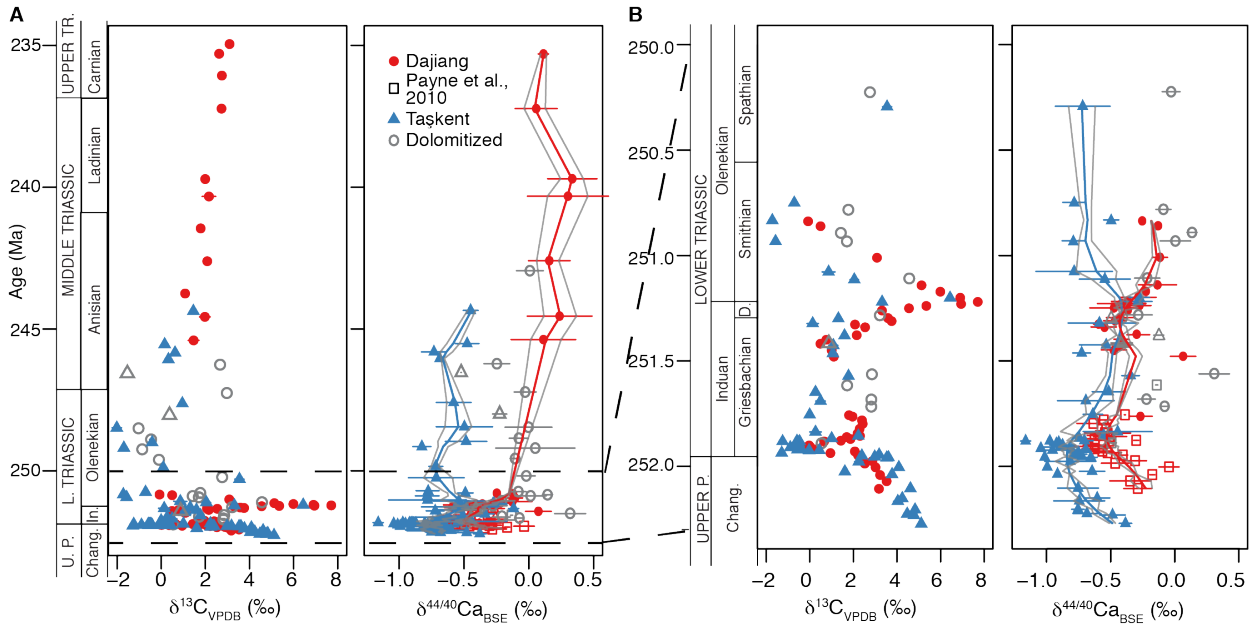
1342
1343

1344 Figure 3



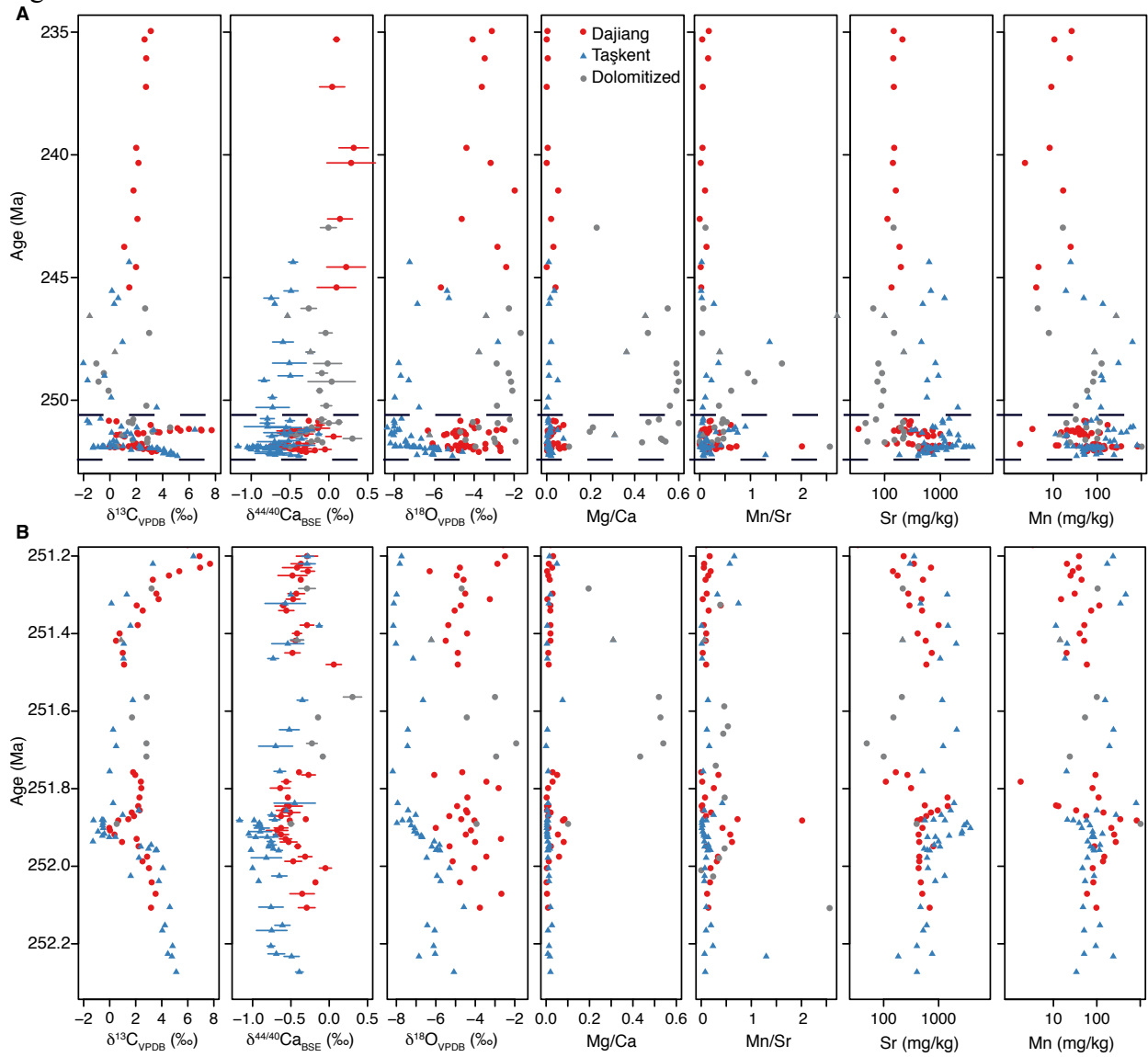
1345
1346
1347

Figure 4



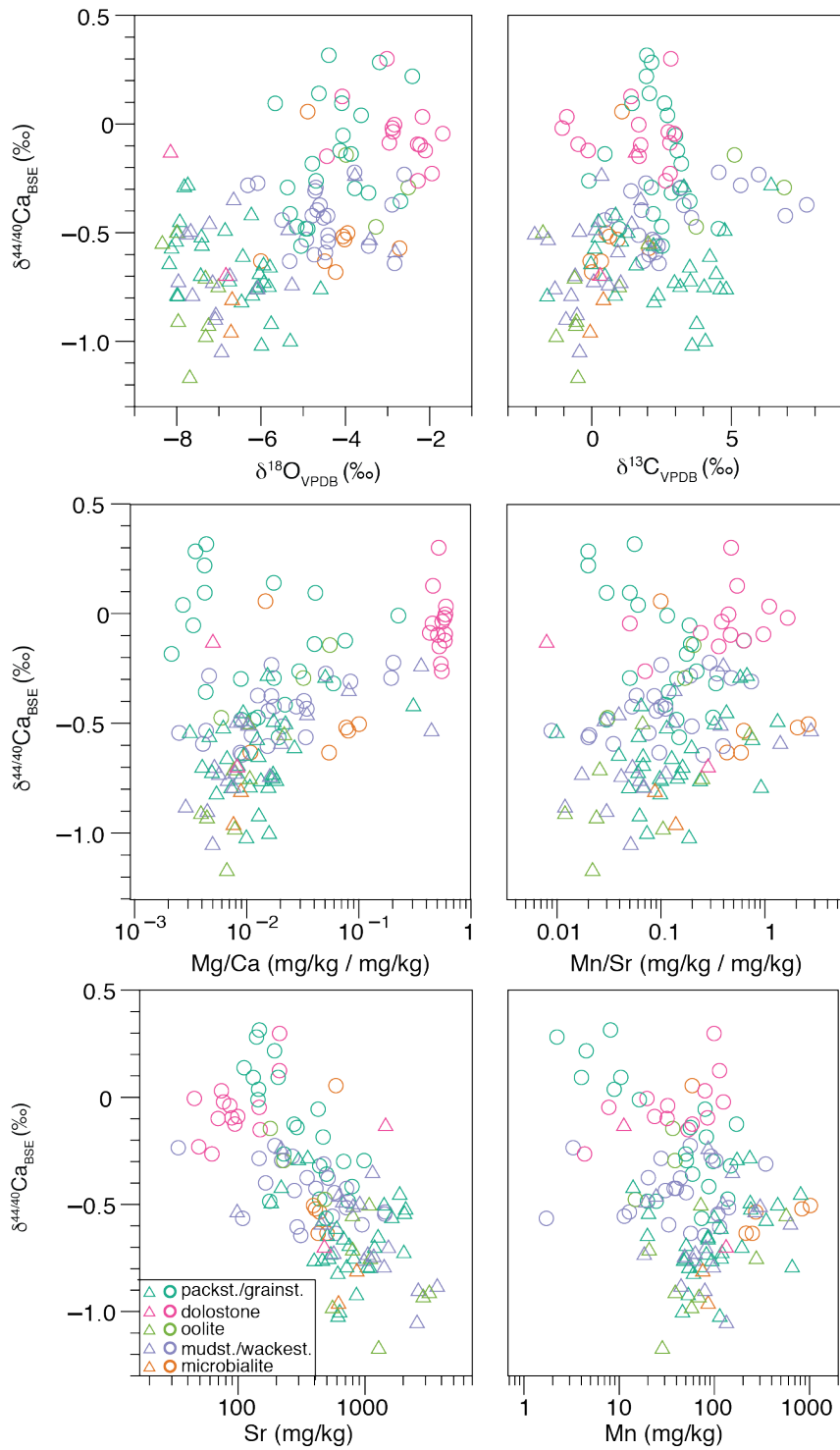
1348

1349 Figure 5



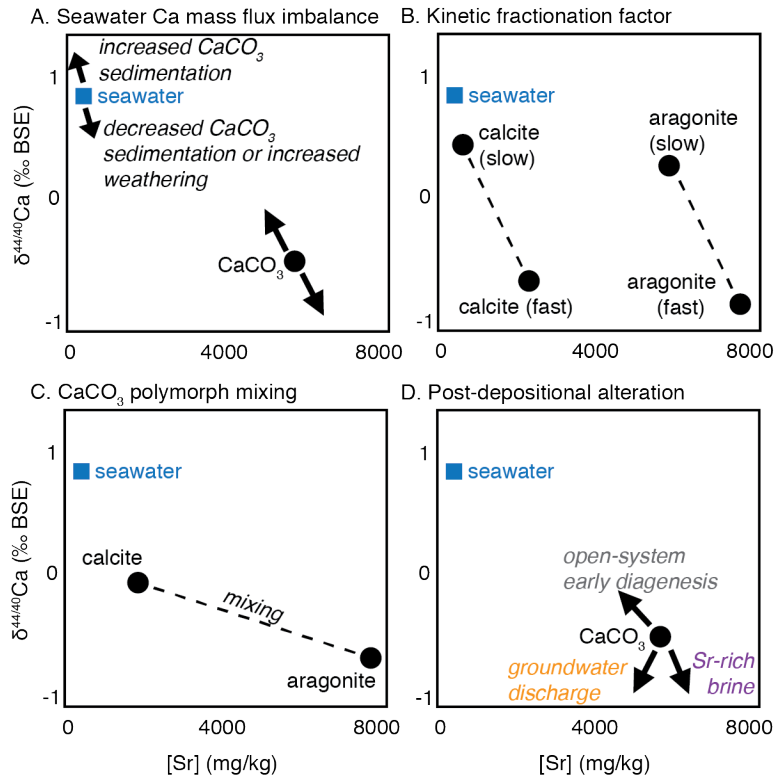
1350
1351

1352 Figure 6

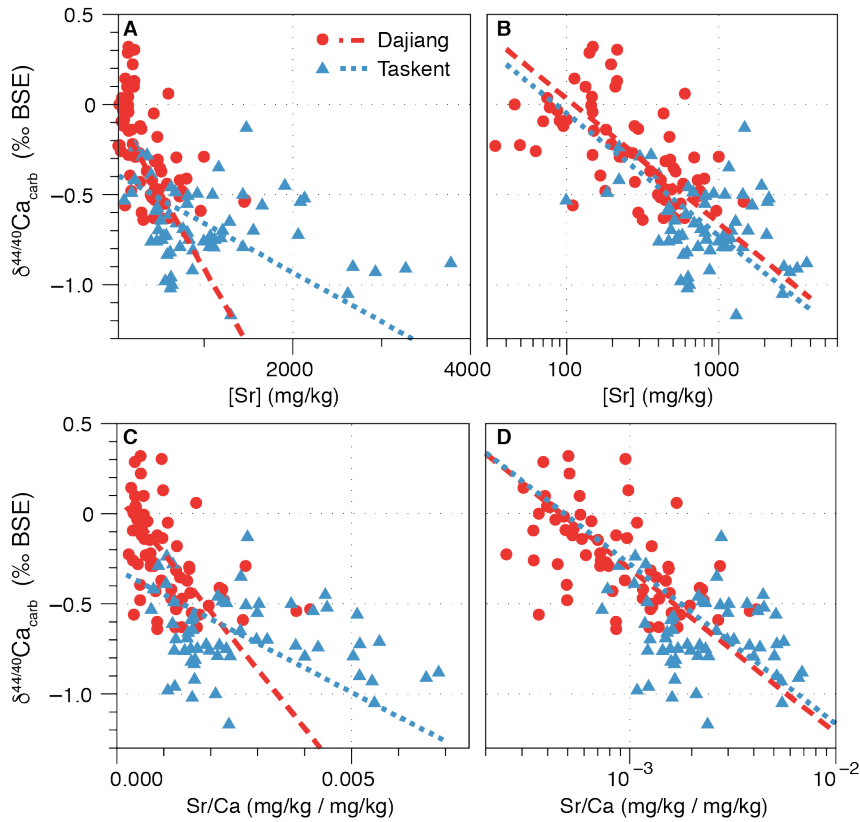


1353
1354

1355 Figure 7

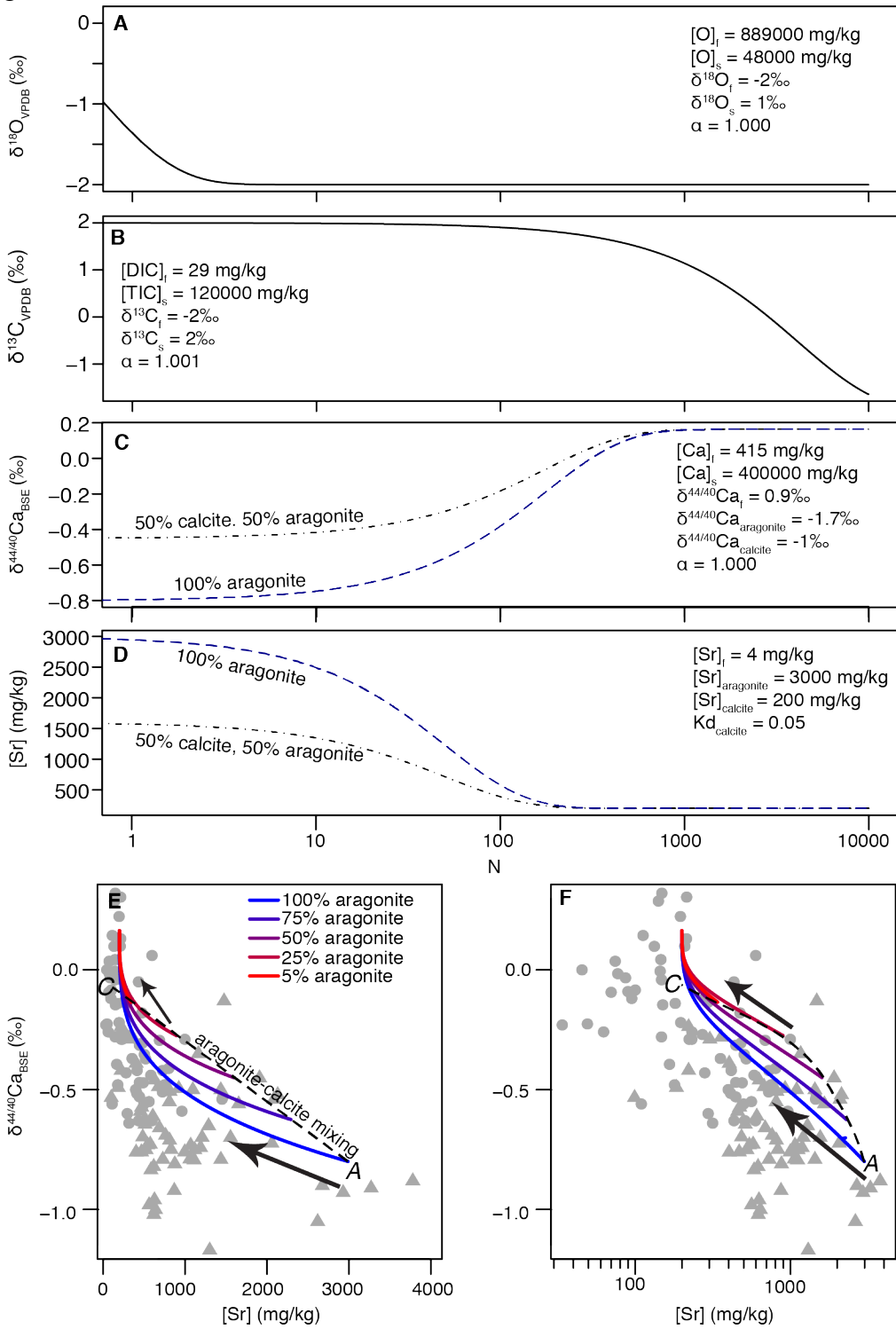


1356
1357 Figure 8



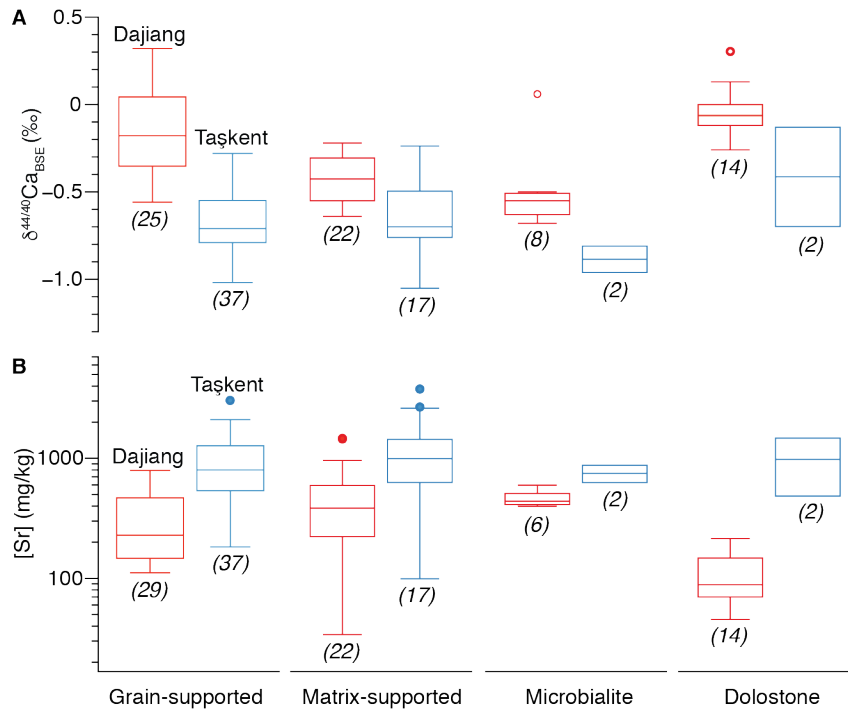
1358

1359 Figure 9



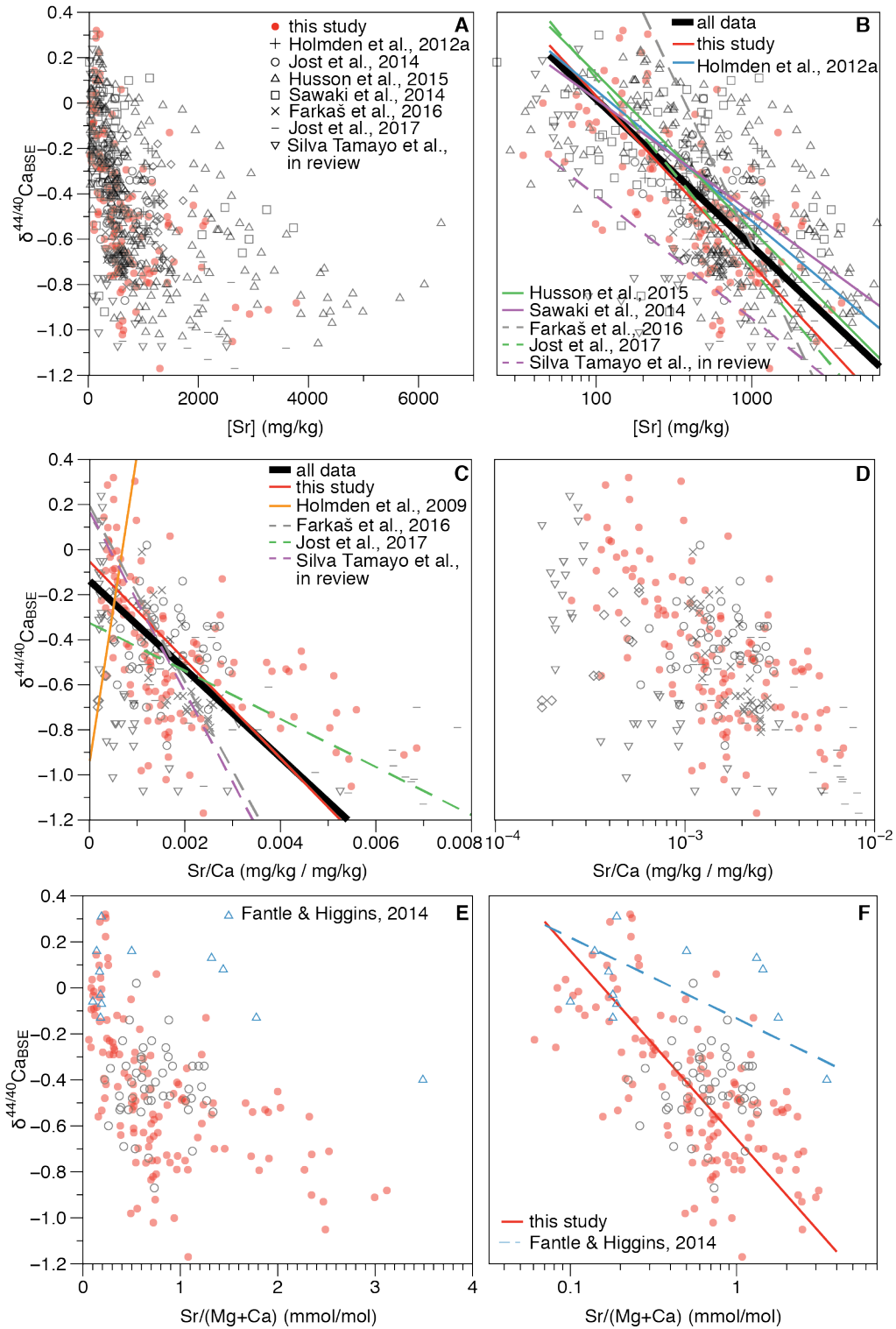
1360
1361

1362 Figure 10



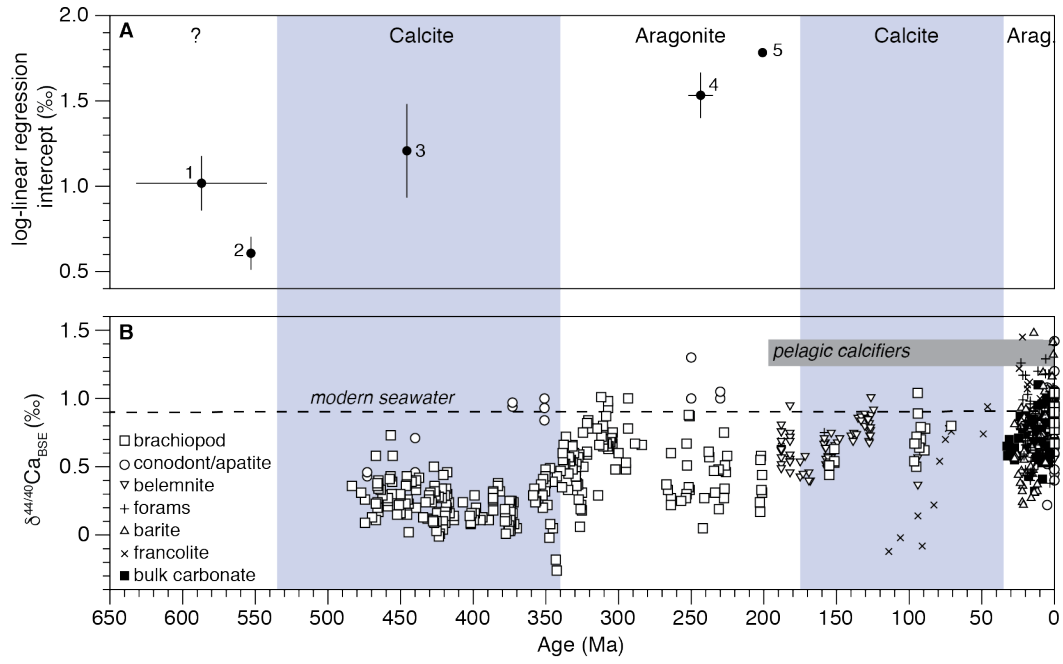
1363
1364

1365 Figure 11



1366
1367

1368 Figure 12



1369
1370

1371 [Note: Tables 1 and S1 are submitted as separate, downloadable excel files]

1372

1373 Table 2: Spearman's ρ correlation statistics and R^2 values of $\delta^{44/40}\text{Ca}$ with geochemical indicators
1374 for diagenesis ($\delta^{18}\text{O}$, Mn/Sr, [Mn]), dolomitization (Mg/Ca, [Mg]), carbon cycling ($\delta^{13}\text{C}$), and the
1375 strontium concentration ([Sr], log([Sr])). Mg/Ca* indicates the analysis was limited to samples
1376 with Mg/Ca < 0.1. Statistically significant correlations ($\alpha = 0.05$) are bolded and italicized.

1377

	Spearman's ρ	<i>p</i>-value	R^2
<i>Dajiang</i>			
$\delta^{18}\text{O}_{\text{carb}}$ (‰ VPDB)	<i>0.343</i>	<i><0.01</i>	0.107
$\delta^{13}\text{C}_{\text{carb}}$ (‰ VPDB)	0.039	0.75	0.000
Mg/Ca	<i>0.273</i>	<i>0.03</i>	0.172
Mg/Ca*	-0.077	0.60	0.010
[Mg]*	-0.944	0.52	0.013
Mn/Sr	0.015	0.90	0.002
[Sr]	<i>-0.619</i>	<i><0.001</i>	0.279
log([Sr])	<i>-0.619</i>	<i><0.001</i>	0.312
[Mn]	<i>-0.313</i>	<i>0.01</i>	0.074
<i>Taşkent</i>			
$\delta^{18}\text{O}_{\text{carb}}$ (‰ VPDB)	-0.133	0.31	0.000
$\delta^{13}\text{C}_{\text{carb}}$ (‰ VPDB)	0.197	0.13	0.031
Mg/Ca	<i>0.402</i>	<i><0.01</i>	0.114
Mg/Ca*	<i>0.330</i>	<i>0.01</i>	0.128
[Mg]*	0.158	0.24	0.147
Mn/Sr	<i>0.281</i>	<i>0.03</i>	0.068
[Sr]	<i>-0.258</i>	<i>0.05</i>	0.084
log([Sr])	<i>-0.258</i>	<i>0.05</i>	0.110
[Mn]	0.189	0.15	0.050

1378

1379

1380 Table 3: Summary of controls on the $\delta^{44/40}\text{Ca}$ value of bulk carbonates.
 1381

Control	References	Effect	Predicted Observation
Early diagenesis	Fantle and DePaolo, 2007; Jacobson and Holmden, 2008; Griffith et al., 2015	At isotopic equilibrium, $\Delta_{c-s} = 0\text{‰}$	Recrystallization with porewaters at equilibrium would produce positive offsets
	Teichert et al., 2009	Up to 0.8‰ negative shift observed in porewaters in silicilastic sediments (presumably less well-Ca-buffered than the carbonate sediment, possibly from Ca released from OM remineralization)	Assuming equilibrium, recrystallization would produce more muted positive offsets
Burial diagenesis	Amini et al., 2008	Hydrothermal fluids are ~0.95‰ more negative than seawater, but more positive relative to BSE	Assuming equilibrium, recrystallization would produce a small positive offset
	Teichert et al., 2009	Fluids that have interacted with oceanic basement are >1‰ more negative than seawater	Assuming equilibrium, recrystallization would produce more muted positive or minor negative offsets
Dolomitization	Heuser et al., 2005; Tipper et al., 2008; Holmden, 2009	Dolomitization occurs close to equilibrium; $\Delta_{c-s} = 0\text{‰}$	Dependent on the $\delta^{44/40}\text{Ca}$ of the dolomitizing fluid.
Submarine groundwater	Holmden et al., 2012b	Can mix with seawater to reduce $\delta^{44/40}\text{Ca}$ by up to 1.2‰	Negative offset from primary values
Fractionation factor			
<i>Precipitation rate</i>	Lemarchand et al., 2004; Gussone et al., 2005; AlKhatib & Eisenhauer, 2017a,b	Negative correlation between precipitation rates and magnitude of Δ_{c-s}	Smaller fractionation (more positive values) with higher Sr
	Tang et al., 2008a; DePaolo, 2011; Nielsen et al., 2012; Watkins et al., 2017	Positive correlation between precipitation rates and magnitude of Δ_{c-s}	Larger fractionation (more negative values) with higher Sr
<i>Temperature</i>	Marriott et al., 2004; Griffith et al., 2008; Hippler et al., 2009; cf. Sime et al., 2005	Weak, positive correlation between temperature and magnitude of Δ_{c-s}	0.013 to 0.2‰ per °C
<i>Carbonate mineralogy</i>	Gussone et al., 2005; Blättler et al., 2012	Calcite $\Delta \sim -1.0$ to -1.4‰ ; Aragonite $\Delta \sim -1.9\text{‰}$	Larger fractionation (more negative values) with higher Sr
<i>Biological control/vital effects</i>	Skulan et al., 1997; Gothmann et al., 2016; Gussone et al., 2005; Steuber and Buhl, 2006	Inorganic calcite has a smaller Δ_{c-s} than organic calcite, but no observed difference for aragonite	More precipitation of inorganic calcite would result in more positive values
	Bohm et al., 2006; summarized in Farkaš et al., 2007; Blättler et al., 2012	Modern carbonates show a range of Δ_{c-s} values depending on mineralogy, where aragonite $\delta^{44/40}\text{Ca} \sim -1.5\text{‰}$, simple calcifiers $\delta^{44/40}\text{Ca} \sim -0.9\text{‰}$, sophisticated calcifiers $\delta^{44/40}\text{Ca} \sim -1.3\text{‰}$	Aragonitic carbonates would have more negative values than calcitic carbonates

1382
 1383

1384 Table 4: Parameters used in diagenetic water-rock interaction model (Figure 9).
 1385

Parameter	Definition	Value					
P	porosity	40 %					
ρ_f	fluid density	1 g/mL					
ρ_s	solid density	3 g/mL					
		O	C	Sr-calcite	Sr-aragonite	Ca-calcite	Ca-aragonite
$C_{f,o}$	initial fluid concentration (seawater)	889000 mg/kg ¹	29 mg/kg ¹	4 mg/kg ²	4 mg/kg ²	415 mg/kg ¹	415 mg/kg ¹
$C_{s,o}$	initial solid concentration	480000 mg/kg ¹	120000 mg/kg ¹	200 mg/kg ³	3000 mg/kg ³	400000 mg/kg ¹	400000 mg/kg ¹
D	single element distribution coefficient	0.54	4137.93	50	750	963.86	963.86
K_d	exchange reaction distribution coefficient	0.00056	4.29	0.052	0.778	1	1
$\delta I_{f,o}$	initial fluid isotopic value	-2 ⁴	-2 ⁴	NA	NA	0.9 ⁵	0.9 ⁵
$\delta I_{s,o}$	initial solid isotopic value	1 ⁶	2 ⁶	NA	NA	-1	-1.7
α	fractionation factor	1.000 ⁷	1.001 ⁷	NA	NA	1.000 ⁸	1.000 ⁸

1386 ¹Banner and Hanson (1990)

1387 ²Half of value from Banner and Hanson (1990)

1388 ³estimates from modern carbonates (Kinsman 1969)

1389 ⁴early diagenetic fluids are typical more negative than primary carbonates (*e.g.*, Tucker and Wright, 1990)

1390 ⁵seawater value (Fantle and Tipper, 2015)

1391 ⁶Selected to represent typical recent carbonate values (Veizer et al., 1999)

1392 ⁷typical fractionation factor at 20 °C (*e.g.*, Tucker and Wright 1990)

1393 ⁸fractionation at equilibrium (Fantle and DePaolo, 2007)

1394

1395 Table 5: Tukey-Kramer pair-wise comparison for Dajiang $\delta^{44/40}\text{Ca}$, grouped by carbonate fabric
 1396 type. Significant relationships ($\alpha = 0.05$) are bolded and italicized. ANOVA results indicate fabric
 1397 type is not a statistically significant control for Taškent. Matrix-supported fabric types include
 1398 mudstones and wackestones, and grain-supported fabric types include packstones, grainstones, and
 1399 oolites.

1400

Fabric type A	Fabric type B	Diff	Lower CI	Upper CI	<i>p</i>-value
Matrix-supported	Dolostone	<i>-0.39</i>	<i>-0.57</i>	<i>-0.28</i>	<i><0.001</i>
Grain-supported	Dolostone	-0.12	-0.30	0.60	0.31
Microbialite	Dolostone	<i>-0.45</i>	<i>-0.69</i>	<i>-0.22</i>	<i><0.001</i>
Grain-supported	Matrix-supported	<i>0.27</i>	<i>0.12</i>	<i>0.43</i>	<i><0.001</i>
Microbialite	Matrix-supported	-0.06	-0.28	0.16	0.87
Microbialite	Grain-supported	<i>-0.34</i>	<i>-0.55</i>	<i>-0.12</i>	<i><0.001</i>

1401

1402

1403 Table 6: Thin-section estimates of microfacies contribution (by area).
 1404

Sample	Sparry calcite	Micrite	Micritic clasts	Recrystallized clasts	Peloids	Microcrystalline cement	Ooids	Skeletal
<i>Dajiang</i>								
PDJ-033	67	0	5	10	0	0	0	18
PDJ-040	0	0	10	0	0	78	0	12
PDJ-055	0	0	0	0	0	99	0	1
PDJ-058	0	10	0	0	0	80	0	10
PDJ-061	0	8	0	0	0	90	0	2
PDJ-064	0	0	0	4	0	95	0	1
PDJ-072	0	100	0	0	0	0	0	0
PDJ-075	0	85	0	0	0	15	0	0
PDJ-107	0	100	0	0	0	0	0	0
PDJ-115	0	100	0	0	0	0	0	0
PDJ-118	0	70	0	0	0	30	0	0
PDJ-127	100	0	0	0	0	0	0	0
PDJ-162	50	45	0	0	0	0	0	5
PDJ-216	0	98	0	0	0	0	0	2
PDJ-235	0	0	0	40	0	60	0	0
PDJ-247	0	100	0	0	0	0	0	0
PDJ-271	0	50	0	0	0	50	0	0
PDJ-274	0	60	0	40	0	0	0	0
PDJ-290	0	72	0	20	0	0	0	8
PDJ-299	0	70	0	10	0	20	0	0
PDJ-316	0	40	0	20	0	40	0	0
MDJ-31	0	80	0	0	0	20	0	0
<i>Taskent</i>								
TCX-47	0	70	5	0	0	0	0	25
TK-0.03	0	67	10	10	0	0	0	13
TK-2.9	0	50	0	50	0	0	0	0
TK-27.1	25	0	0	0	0	0	75	0
TK-45.5	0	95	0	0	0	5	0	0
TK-76.5	5	10	40	0	0	45	0	0
TK-234	10	0	0	0	0	70	0	20
TK-450.5	3	0	15	0	75	0	0	7
TK-489.5	0	99	0	0	0	1	0	0
TKU-63.7	5	0	95	0	0	0	0	0

1405
 1406

1407 **APPENDIX A**

1408

1409 **Carbonate diagenetic model**

1410 To illustrate the impact of diagenesis on Ca relative to other major and minor components
1411 of carbonates, we develop an open-system water-rock interaction model presented in Figure 9. In
1412 this set of calculations, we track the evolution of $\delta^{18}\text{O}$, $\delta^{13}\text{C}$, [Sr], and $\delta^{44/40}\text{Ca}$ in a carbonate rock
1413 reacting with a fluid similar to seawater in order to determine the relative susceptibility of each of
1414 these components to alteration during early diagenesis. Following Banner and Hanson (1990), we
1415 calculate the concentration of each element in the fluid-rock system as

1416
$$C_o = F \times C_{f,o} + (1 - F) \times C_{s,o} \quad (\text{A.1})$$

1417 where C_o is the concentration of the element in the system, $C_{f,o}$ is the concentration of element I in
1418 the initial fluid, $C_{s,o}$ is the concentration of the element in the initial solid, and F is the weight
1419 fraction of the fluid as defined by

1420
$$F = \frac{P \times \rho_f}{P \times \rho_f + (1 - P) \rho_s} \quad (\text{A.2})$$

1421 where P is the porosity and ρ_s and ρ_f are the density of the solid and fluid, respectively. Given a
1422 distribution coefficient D , defined as C_s/C_f , the concentration of the element in the solid, C_s , at
1423 equilibrium is calculated by

1424
$$C_s = \frac{C_o}{F/D + (1 - F)} \quad (\text{A.3}).$$

1425 The isotopic composition of element I in the solid, expressed in delta notation as δI_s , can also be
1426 tracked using the following equation:

1427
$$\delta I_s = \frac{\delta I_o C_o \alpha - 1000 C_f F (1 - \alpha)}{C_s (1 - F) \alpha + C_f F} \quad (\text{A.4})$$

1428 where δI_o is the isotopic composition of the water-rock system and α is the fractionation factor
1429 between the fluid and the solid. The degree of water-rock interaction is represented by N :

1430
$$N = n \times (F / (1 - F)) \quad (\text{A.5})$$

1431 where n is the number of iterations.

1432 We assume that the distribution coefficients (D), fractionation factors (α), and initial fluid
1433 and solid compositions (C) are similar to those of modern marine carbonate sediments as described
1434 in Table 4, and that these did not vary through time or with biotic versus abiotic precipitation.

1435

1436 **Reference**

1437 Banner, J.L., Hanson, G.N., 1990. Calculation of simultaneous isotopic and trace element variations during
1438 water-rock interaction with applications to carbonate diagenesis. *Geochimica et Cosmochimica*
1439 *Acta* 54, 3123-3137.

1440

Table 1. Isotopic and geochemical data.

Sample	Stratigraphic height (m)	Age (yr)	Lithology ¹	$\delta^{13}\text{C}_{\text{carb}}$ (‰VPDB)	$\delta^{18}\text{O}_{\text{carb}}$ (‰VPDB)	$\delta^{44/40}\text{Ca}_{\text{car}}$ (‰BSE)	$\delta^{44/40}\text{Ca}_{\text{car}}$ (‰915a)	2 σ (‰)	n	Lab	Mg/Ca	Mn/Sr	Sr/Ca	Mn (ppm)	Sr (ppm)	Reference
<i>Dajiang</i>																
PDJ-001	0	252.107	PG	3.18	-3.77	-0.29	0.71	0.11	3	Berkeley	0.009	0.142	0.0015	97.7	687.9	Payne et al., 2010
PDJ-009	9	252.071	PG	3.53	-2.68	-0.35	0.65	0.16	2	Berkeley	0.004	0.118	0.0013	59.5	504.0	Payne et al., 2010
PDJ-017	16.4	252.041	PG	3.23	-4.78	-0.18	0.82	0.02	2	Berkeley	0.002	0.175	0.0013	83.0	473.5	Payne et al., 2010
PDJ-026	25.6	252.005	PG	3.02	-4.05	-0.05	0.95	0.08	2	Berkeley	0.003	0.186	0.0011	80.5	432.5	Payne et al., 2010
PDJ-030	30	251.987	PG	2.52	-5.15	-0.47	0.53	0.11	2	Berkeley	0.013	0.313	0.0012	139.0	444.5	Payne et al., 2010
PDJ-033	33	251.975	PG	2.88	-3.44	-0.31	0.69	0.09	3	Berkeley	0.060	0.334	0.0013	148.5	445.0	Payne et al., 2010
PDJ-040	39.7	251.949	PG	2.22	-5.31	-0.41	0.59	0.04	1	Berkeley	0.022	0.110	0.0022	88.0	802.0	Payne et al., 2010
PDJ-044	42.5	251.937	TH	0.95	-4.01	-0.53	0.47	0.11	2	Berkeley	0.081	0.615	0.0013	273.0	444.0	Payne et al., 2010
PDJ-046	44.5	251.929	TH	2.07	-2.70	-0.57	0.43	0.08	2	Berkeley	--	--	--	--	--	Payne et al., 2010
PDJ-050	47.3	251.918	TH	0.37	-4.48	-0.63	0.37	0.10	1	Berkeley	0.055	0.580	0.0012	251.0	433.0	Payne et al., 2010
PDJ-053	50	251.908	TH	0.03	-4.22	-0.68	0.32	0.14	3	Berkeley	--	--	--	--	--	Payne et al., 2010
PDJ-055	51.6	251.901	TH	-0.03	-6.00	-0.63	0.37	0.09	2	Berkeley	0.011	0.425	0.0014	216.0	508.0	Payne et al., 2010
PDJ-058	54.2	251.891	TH	0.54	-3.94	-0.50	0.50	0.04	2	Berkeley	0.101	2.564	0.0013	1019.0	397.5	Payne et al., 2010
PDJ-061	56.4	251.882	TH	0.66	-4.04	-0.52	0.48	0.01	2	Berkeley	0.078	2.015	0.0013	830.0	412.0	Payne et al., 2010
PDJ-064	57.4	251.879	MW	1.43	-4.71	-0.31	0.69	0.02	2	Berkeley	0.085	0.725	0.0015	347.0	478.5	Payne et al., 2010
PDJ-068	60.4	251.871	MW	1.87	-5.32	-0.63	0.37	0.12	2	Berkeley	0.009	0.096	0.0017	57.0	595.5	Payne et al., 2010
PDJ-072	63.9	251.861	MW	1.70	-4.40	-0.51	0.49	0.13	2	Berkeley	0.021	0.196	0.0020	142.0	724.0	Payne et al., 2010
PDJ-075	66	251.856	MW	2.31	-4.47	-0.59	0.41	0.10	1	Berkeley	0.004	0.035	0.0027	33.5	961.5	Payne et al., 2010
PDJ-080	70.1	251.845	MW	2.19	-4.92	-0.53	0.47	0.18	2	Berkeley	0.004	0.009	0.0041	13.0	1463.0	Payne et al., 2010
PDJ-081	70.7	251.843	MW	--	--	-0.55	0.45	--	3	Berkeley	0.011	0.021	0.0016	11.5	560.5	Payne et al., 2010
PDJ-090	77.6	251.823	MW	2.29	-4.40	-0.54	0.46	--	2	Berkeley	0.002	0.076	0.0038	110.0	1452	Payne et al., 2010
PDJ-100	87.6	251.798	MW	2.43	-2.82	-0.64	0.36	0.13	2	Berkeley	0.009	0.252	0.0009	79.5	315.5	Payne et al., 2010
PDJ-107	93.8	251.782	MW	2.40	-3.44	-0.56	0.44	0.06	2	Berkeley	0.034	0.020	0.0004	1.8	109.6	this study
PDJ-115	100.4	251.764	MW	1.96	-6.08	-0.27	0.73	0.09	2	Berkeley	0.051	0.343	0.0008	93.0	271.0	Payne et al., 2010
PDJ-118	103	251.758	MW	1.80	-4.66	-0.39	0.61	0.01	2	Berkeley	0.033	0.000	0.0005	0.0	166.4	this study
PDJ-127	118.2	251.717	DL	2.82	-2.94	-0.08	0.92	0.03	2	Berkeley	0.433	0.238	0.0005	23.9	100.2	this study
PDJ-132	131	251.683	DL	2.82	-1.93	-0.23	0.77	0.07	2	Berkeley	0.543	0.000	0.0003	0.0	49.3	this study
PDJ-140	156.2	251.616	DL	1.71	-4.43	-0.15	0.85	0.01	2	Berkeley	0.527	0.355	0.0007	53.5	150.5	Payne et al., 2010
PDJ-148	176	251.564	DL	2.85	-3.00	0.30	1.30	0.12	4	Berkeley	0.520	0.466	0.0010	100.0	214.5	this study
PDJ-162	207.5	251.480	TH	1.11	-4.89	0.06	1.06	0.10	4	Berkeley	0.015	0.099	0.0017	59.0	597.5	this study
PDJ-171	218.8	251.450	PG	1.01	-4.89	-0.48	0.52	0.10	3	GEOMAR	0.012	0.030	0.0023	20.1	750.0	this study
PDJ-179	230.6	251.418	MW	0.49	-5.50	-0.44	0.56	0.06	3	GEOMAR	0.016	0.090	0.0016	51.1	582.8	this study
PDJ-191	237.75	251.400	MW	0.76	-4.41	-0.42	0.58	0.06	3	GEOMAR	0.018	0.100	0.0012	40.2	415.4	this study
PDJ-201	251	251.378	PG	2.16	-5.37	-0.29	0.71	0.09	3	GEOMAR	0.018	0.050	0.0027	51.4	997.8	this study
PDJ-216	274.1	251.341	PG	2.54	-5.05	-0.56	0.44	0.10	3	GEOMAR	0.019	0.148	0.0018	74.1	499.2	this study
PDJ-224	282.2	251.327	MW	2.08	-4.73	-0.60	0.40	0.04	3	GEOMAR	0.015	0.390	0.0009	114.1	295.2	this study
PDJ-235	292.2	251.311	OL	3.76	-3.26	-0.47	0.53	0.09	2	Berkeley	0.006	0.031	0.0014	15.0	488.5	this study
PDJ-241	301	251.297	MW	3.59	-4.51	-0.43	0.57	0.11	3	GEOMAR	0.035	0.110	0.0008	30.9	280.6	this study
PDJ-247	309.1	251.284	MW	3.22	-4.69	-0.29	0.71	0.11	3	GEOMAR	0.196	0.468	0.0008	104.3	222.6	this study
PDJ-260	323.1	251.261	MW	3.31	-4.60	-0.37	0.63	0.02	2	Berkeley	0.017	0.086	0.0015	44.5	519.0	this study
PDJ-265	329.7	251.250	PG	4.55	-4.94	-0.48	0.52	0.19	3	GEOMAR	0.009	0.140	0.0005	24.8	179.2	this study
PDJ-269	336.6	251.239	MW	5.35	-6.31	-0.28	0.72	0.09	3	GEOMAR	0.005	0.189	0.0004	27.9	147.8	this study
PDJ-271	342.3	251.230	MW	6.94	-4.78	-0.42	0.58	0.19	3	GEOMAR	0.028	0.053	0.0022	38.2	726.2	this study
PDJ-274	348.4	251.220	MW	7.71	-2.88	-0.37	0.63	0.13	3	GEOMAR	0.013	0.058	0.0009	20.5	354.0	this study
PDJ-276	351.9	251.200	OL	6.90	-2.49	-0.29	0.71	0.14	3	GEOMAR	0.032	0.169	0.0007	39.0	231.3	this study
PDJ-279	357	251.172	MW	5.99	-2.59	-0.23	0.77	0.02	3	GEOMAR	0.017	0.100	0.0006	3.3	33.9	this study
PDJ-282	362.4	251.141	OL	5.13	-3.97	-0.14	0.86	0.15	3	GEOMAR	0.056	0.204	0.0006	37.0	181.2	this study
PDJ-286	368.2	251.109	MW	4.56	-3.77	-0.22	0.78	0.10	3	GEOMAR	0.205	0.290	0.0007	56.3	196.6	this study
PDJ-290	385.7	251.011	PG	3.08	-4.12	-0.12	0.88	0.06	2	Berkeley	0.076	0.615	0.0009	171.5	279.0	this study
PDJ-299	399.5	250.933	DL	1.70	-2.82	0.00	1.00	0.12	3	GEOMAR	0.597	0.440	0.0004	19.8	45.5	this study
PDJ-301	406.7	250.893	DL	1.43	-4.07	0.13	1.13	0.04	2	Berkeley	0.462	0.533	0.0010	114.0	214.0	this study
PDJ-307	412.35	250.861	PG	0.50	-3.86	-0.14	0.86	0.02	2	Berkeley	0.040	0.192	0.0010	56.5	294.5	this study
PDJ-316	419.9	250.838	PG	-0.08	-4.69	-0.26	0.74	0.01	2	Berkeley	0.030	0.218	0.0007	50.5	232.0	this study
DJB-03	445.9	250.783	DL	1.77	-2.21	-0.09	0.91	0.06	2	Berkeley	0.511	0.460	0.0003	32.3	70.0	this study
DJB-06	579.9	250.225	DL	2.76	-2.86	-0.03	0.97	0.07	2	Berkeley	0.560	0.380	0.0004	32.7	86.7	this study
DJB-08	624.3	249.612	DL	-0.10	-2.09	-0.12	0.88	0.04	2	Berkeley	0.590	0.620	0.0005	59.0	95.0	this study
DJB-11	655.6	249.243	DL	-0.86	-2.15	0.04	1.04	0.31	2	Berkeley	0.604	1.080	0.0004	80.3	74.4	this study
DJB-13	696.5	248.895	DL	-0.46	-2.27	-0.09	0.91	0.07	2	Berkeley	0.594	0.950	0.0005	85.4	89.9	this study
DJB-15	742.6	248.503	DL	-1.03	-2.87	-0.02	0.88	0.18	2	Berkeley	0.586	1.620	0.0005	125.1	77.3	this study
DJB-19	888.8	247.258	DL	2.97	-1.67	-0.04	0.96	0.08	2	Berkeley	0.458	0.050	0.0007	7.9	147.9	this study
DJB-21	1006.3	246.259	DL	2.67	-2.26	-0.26	0.74	0.10	3	Berkeley	0.555	0.070	0.0003	4.4	62.6	this study
DJB-27	1108.1	245.403	PG	1.47	-5.66	0.10	1.00	0.25	2	Berkeley	0.041	0.030	0.0004	4.1	132.9	this study
MDJ-31	1226	244.573	PG	1.98	-2.40	0.22	1.12	0.25	3	Berkeley	0.004	0.020	0.0005	4.6	195.6	this study

DJB-46	1424.8	242.966	PG	--	--	-0.01	0.99	0.10	2	Berkeley	0.227	0.114	0.0006	16.5	144.8	this study
DJB-48	1470.9	242.612	PG	2.09	-4.62	0.14	1.04	0.16	3	Berkeley	0.017	0.000	0.0003	0.0	112.4	this study
DJB-57	1767.6	240.329	PG	2.16	-3.17	0.29	1.29	0.31	4	Berkeley	0.003	0.020	0.0004	2.3	141.0	this study
DJB-60	1847.7	239.713	PG	1.99	-4.38	0.32	1.32	0.19	3	Berkeley	0.004	0.056	0.0005	8.2	148.5	this study
DJB-62	2170.5	237.230	PG	2.73	-3.62	0.04	0.94	0.16	3	Berkeley	0.003	0.060	0.0004	9.0	146.4	this study
DJB-71	2422.0	235.296	PG	2.63	-4.08	0.10	1.10	0.04	2	Berkeley	0.004	0.050	0.0006	10.6	208.9	this study
<i>Taskent</i>																
TCX-0	0	252.273	PG	5.11	-5.08	-0.39	0.61	0.05	3	GEOMAR	0.019	0.080	0.0011	33.8	403.4	this study
TCX-6	6	252.233	PG	4.78	-6.86	-0.49	0.51	0.10	3	GEOMAR	0.017	1.298	0.0012	239.3	184.4	this study
TCX-7	7	252.226	PG	4.47	-6.04	-0.69	0.31	0.11	3	GEOMAR	0.008	0.067	0.0015	51.0	762.3	this study
TCX-10	10	252.206	PG	4.83	-6.11	-0.76	0.24	0.05	3	GEOMAR	0.013	0.235	0.0014	94.5	402.8	this study
TCX-16	16	252.166	PG	4.04	-6.06	-0.75	0.25	0.20	3	GEOMAR	0.009	0.097	0.0016	50.9	524.6	this study
TCX-18	18	252.152	PG	4.24	-6.43	-0.61	0.39	0.10	3	GEOMAR	0.027	0.195	0.0012	118.2	607.0	this study
TCX-25	25	252.105	PG	4.62	-4.58	-0.76	0.24	0.16	3	GEOMAR	0.018	0.100	0.0012	48.0	467.5	this study
TCX-35	35	252.038	PG	3.77	-5.76	-0.92	0.08	0.01	3	GEOMAR	0.013	0.062	0.0017	53.7	869.1	this study
TCX-37	37	252.025	PG	1.61	-5.94	-0.65	0.35	0.10	3	GEOMAR	0.013	0.067	0.0026	86.2	1287.3	this study
TCX-40	40	252.005	PG	4.09	-5.30	-1.00	0.00	--	3	GEOMAR	0.016	0.073	0.0021	46.7	640.2	this study
TCX-44	44	251.978	PG	2.25	-6.46	-0.82	0.18	0.20	3	GEOMAR	0.005	0.098	0.0016	60.8	618.4	this study
TCX-47	47	251.958	PG	3.61	-5.99	-1.02	-0.02	0.02	3	GEOMAR	0.010	0.185	0.0016	114.7	620.6	this study
TCX-47.5	47.5	251.955	PG	2.98	-5.93	-0.73	0.27	0.02	3	GEOMAR	0.017	0.153	0.0022	83.0	543.6	this study
TK-0.03	46.83	251.959	PG	3.53	-5.79	-0.66	0.34	0.05	3	GEOMAR	0.007	0.126	0.0015	86.4	687.8	this study
TK-1.5	48.3	251.949	PG	2.39	-6.20	-0.79	0.21	0.03	3	GEOMAR	0.011	0.067	0.0021	71.4	1059.6	this study
TK-2.15	48.95	251.945	MW	3.18	-5.81	-0.75	0.25	0.06	3	GEOMAR	0.017	0.143	0.0017	118.8	829.5	this study
TK-2.9	49.7	251.936	TH	-1.29	-6.08	-0.76	0.24	0.05	3	GEOMAR	0.007	0.062	0.0020	61.4	996.2	this study
TK-3.8	50.6	251.925	TH	-0.03	-6.71	-0.96	0.04	0.10	3	GEOMAR	0.008	0.138	0.0012	86.6	627.0	this study
TK-4.15	50.95	251.925	MW	0.44	-6.69	-0.81	0.19	0.09	3	GEOMAR	0.009	0.087	0.0017	76.2	874.7	this study
TK-7.3	54.1	251.921	MW	-0.57	-6.74	-0.70	0.30	0.03	3	GEOMAR	0.005	0.053	0.0030	81.8	1554.8	this study
TK-12.3	59.4	251.916	MW	-0.41	-6.94	-1.05	-0.05	0.01	3	GEOMAR	0.005	0.051	0.0055	134.6	2618.5	this study
TK-18.1	64.9	251.911	MW	-0.89	-7.09	-0.90	0.10	0.15	3	GEOMAR	0.004	0.030	0.0052	80.1	2675.9	this study
TK-27.1	73.9	251.902	OL	-0.50	-7.08	-0.88	0.12	0.10	3	GEOMAR	0.003	0.012	0.0069	45.1	3779.1	this study
TK-34.1	80.9	251.895	OL	-0.54	-7.25	-0.93	0.07	0.06	3	GEOMAR	0.004	0.024	0.0054	69.4	2929.6	this study
TK-40.1	86.9	251.889	OL	-0.52	-7.97	-0.91	0.09	0.03	3	GEOMAR	0.004	0.012	0.0066	39.3	3270.7	this study
TK-45.5	92.3	251.882	OL	-1.25	-7.32	-0.98	0.02	--	3	GEOMAR	0.008	0.104	0.0011	58.2	561.7	this study
TK-47	93.8	251.882	OL	-0.47	-7.70	-1.17	-0.17	0.04	3	GEOMAR	0.007	0.022	0.0024	28.7	1301.0	this study
TK-48.5	95.3	251.880	OL	-0.59	-7.32	-0.71	0.29	0.07	3	GEOMAR	0.008	0.026	0.0056	20.9	811.4	this study
TK-54.5	101.3	251.868	PG	1.01	-7.02	-0.75	0.25	0.05	3	GEOMAR	0.011	0.247	0.0023	276.7	1118.4	this study
TK-58.7	105.5	251.856	PG	2.23	-7.41	-0.56	0.44	0.02	3	GEOMAR	0.005	0.061	0.0051	100.3	1654.3	this study
TK-62	108.8	251.837	PG	0.26	-7.93	-0.45	0.55	0.27	3	GEOMAR	0.009	0.421	0.0044	804.8	1909.5	this study
TK-76.5	123.3	251.755	PG	0.00	-8.19	-0.64	0.36	0.08	2	Berkeley	0.009	0.039	0.0016	20.1	511.7	this study
TK-88	134.8	251.690	PG	0.49	-7.44	-0.70	0.20	0.22	3	Berkeley	0.004	0.160	0.0032	195.2	1208.0	this study
TK-95	142.3	251.648	MW	0.26	-7.42	-0.52	0.48	0.13	3	GEOMAR	0.006	0.113	0.0045	241.8	2130.5	this study
TK-109	155.8	251.572	MW	1.78	-6.65	-0.35	0.65	0.07	3	GEOMAR	0.082	0.134	0.0026	155.9	1163.7	this study
TK-128	174.8	251.464	PG	1.06	-7.15	-0.73	0.27	0.07	2	Berkeley	0.006	0.017	0.0038	18.6	1068.9	this study
TK-136.5	183.3	251.426	PG	1.08	-8.02	-0.54	0.46	0.21	3	GEOMAR	0.003	0.010	0.0042	20.6	2084.5	this study
TK-139.5	186.3	251.417	DL	0.88	-6.23	-0.42	0.48	0.09	1	Berkeley	0.309	0.064	0.0008	14.2	220.8	this study
TK-151	197.8	251.380	PG	1.60	-8.15	-0.13	0.87	0.04	3	GEOMAR	0.005	0.008	0.0028	11.4	1476.1	this study
TK-169	215.8	251.322	PG	0.14	-8.13	-0.57	0.33	0.27	2	Berkeley	0.012	0.744	0.0016	350.2	470.7	this study
TK-176.2	223	251.299	PG	1.31	-7.99	-0.50	0.50	0.00	3	GEOMAR	0.022	0.323	0.0030	463.7	1436.3	this study
TK-201	247.8	251.220	PG	3.32	-7.83	-0.29	0.71	0.11	2	Berkeley	0.051	0.570	0.0009	173.8	302.6	this study
TK-207	253.8	251.201	OL	6.44	-7.74	-0.28	0.72	0.08	3	GEOMAR	0.015	0.660	0.0012	236.4	358.3	this study
TK-226	272.8	251.114	PG	2.04	-8.35	-0.55	0.45	0.20	3	GEOMAR	0.022	0.702	0.0030	568.0	809.2	this study
TK-234	280.8	251.078	PG	0.87	-8.00	-0.79	0.21	0.30	3	GEOMAR	0.016	0.901	0.0024	656.4	728.5	this study
TK-265.5	312.3	250.933	OL	-1.57	-7.98	-0.79	0.11	0.09	3	Berkeley	0.007	0.049	0.0040	54.5	1111.5	this study
TK-287	333.8	250.833	MW	-1.72	-8.01	-0.50	0.50	0.06	3	GEOMAR	0.010	0.066	0.0037	72.6	1095.0	this study
TK-305	351.8	250.750	PG	-0.71	-7.63	-0.79	0.21	0.09	2	Berkeley	0.008	0.068	0.0050	98.4	1437.2	this study
TK-315	361.8	250.294	MW	3.55	-6.76	-0.72	0.18	0.22	3	Berkeley	0.005	0.060	0.0052	120.9	2060.0	this study
TK-321	367.8	249.888	--	0.10	-7.97	-0.73	0.27	0.05	2	Berkeley	0.008	0.111	0.0019	63.5	575.0	this study
TK-351	397.8	249.191	MW	-1.69	-7.27	-0.83	0.07	0.07	3	Berkeley	0.048	0.230	0.0016	134.3	583.4	this study
TK-377.5	424.3	249.004	MW	-0.41	-7.67	-0.50	0.40	0.16	2	Berkeley	0.008	0.130	0.0023	123.5	923.7	this study
TK-450.5	497.3	248.487	MW	-2.01	-7.77	-0.51	0.49	0.22	3	Berkeley	0.010	0.370	0.0027	303.0	817.9	this study
TK-474.8	521.6	248.037	MW	0.38	-3.76	-0.24	0.76	0.06	2	Berkeley	0.363	0.393	0.0011	86.8	220.9	this study
TK-489.5	536.3	247.627	MW	0.96	-2.81	-0.59	0.41	0.13	2	Berkeley	0.020	1.377	0.0016	630.0	457.4	this study
TK-562	608.8	246.568	DL	-1.54	-3.40	-0.53	0.47	0.00	2	Berkeley	0.448	2.708	0.0007	268.5	99.2	this study
TK-627	673.8	246.075	MW	0.33	-6.84	-0.70	0.30	0.02	2	Berkeley	0.008	0.280	0.0013	133.7	483.9	this study
TKU-25	705	245.838	MW	0.63	-5.26	-0.74	0.26	0.10	2	Berkeley	0.016	0.041	0.0043	49.2	1189.5	this study
TKU-63.7	743.7	245.545	MW	0.16	-5.35	-0.49	0.51	0.09	2	Berkeley	0.009	0.029	0.0022	19.4	676.6	this study
TKU-218.:	898.5	244.371	PG	1.46	-7.23	-0.46	0.54	0.06	2	Berkeley	0.035	0.039	0.0022	24.7	628.9	this study

¹PG = packstone/grainstone; TH = thrombolite; MW = mudstone/wackestone; OL = oolite; DL = dolostone

Table A.1. Regression statistics comparing linear models with log-linear models for the data in this study and for published datasets. Δ AIC is the difference between the

Reference	Sr data format	Linear						Log-linear						Δ AIC
		R ²	p-value	AIC	slope (\pm SE)	intercept (\pm SE)	R ²	p-value	AIC	slope (\pm SE)	intercept (\pm SE)			
Latest Permian - Late Triassic, <i>this study</i>	[Sr]	0.303	<0.001	1912.4	-0.0005 \pm 0.0000	-0.1239 \pm 0.0368	0.458	<0.001	10.1	-0.7479 \pm 0.0354	1.533 \pm 0.1340	-1902.4		
	Sr/Ca	0.313	<0.001	-1404	-227.3 \pm 18.51	-0.0455 \pm 0.0413	0.440	<0.001	-47.0	-0.9637 \pm 0.0706	-3.217 \pm 0.1913	1356.8		
	Sr/(Ca+Mg)	0.328	<0.001	155.3	-0.4740 \pm 0.0376	-0.0704 \pm 0.0388	0.460	<0.001	-12.0	-0.8172 \pm 0.0575	-0.6557 \pm 0.0266	-167.2		
Triassic/Jurassic, <i>Jost et al. (2017)</i>	[Sr]	0.574	<0.001	460.4	-0.0003 \pm 0.0000	-0.3558 \pm 0.0597	0.565	<0.001	-32.9	-0.8370 \pm 0.1201	1.783 \pm 0.3239	-493.3		
	Sr/Ca	0.578	<0.001	-334.4	-106.6 \pm 15.05	-0.3250 \pm 0.0625	0.548	<0.001	-34.2	-0.8712 \pm 0.1277	-2.923 \pm 0.2870	300.2		
Permian/Triassic, <i>Silva Tamayo et al., in review (Oman and Italy)</i>	[Sr]	0.362	<0.001	515.5	-0.0008 \pm 0.0001	-0.2139 \pm 0.0803	0.541	<0.001	58.4	-0.5607 \pm 0.0781	0.6741 \pm 0.1556	-457.1		
	Sr/Ca	0.342	<0.001	-389.5	-400.6 \pm 66.94	-0.1704 \pm 0.0831	0.634	<0.001	5.0	-1.067 \pm 0.1290	-4.021 \pm 0.3886	394.5		
Middle - Late Permian, <i>Jost et al. (2014)</i>	[Sr]	0.004	0.65	586.4	-0.0006 \pm 0.0001	-0.0491 \pm 0.0660	0.003	0.69	-104.0	-0.8267 \pm 0.1431	1.840 \pm 0.3443	-690.4		
	Sr/Ca	0.002	0.75	-652.9	-251.8 \pm 43.61	-0.0209 \pm 0.0700	0.000	0.90	-108.7	-0.8694 \pm 0.1507	-2.887 \pm 0.3741	544.2		
	Sr/(Ca+Mg)	0.001	0.81	-64.9	-0.5509 \pm 0.0955	-0.0267 \pm 0.0693	0.000	0.96	-107.4	-0.8581 \pm 0.1488	-0.5787 \pm 0.0414	-42.5		
Late Silurian, <i>Farkas et al. (2016)</i>	[Sr]	0.490	<0.001	402.8	-0.0014 \pm 0.0002	0.1356 \pm 0.0899	0.540	<0.001	-103.3	-1.467 \pm 0.1975	3.377 \pm 0.4722	-506.1		
	Sr/Ca	0.669	<0.001	-517.4	-391.9 \pm 44.07	0.1963 \pm 0.0781	0.699	<0.001	-123.5	-1.571 \pm 0.1676	-4.854 \pm 0.4220	394.0		
Late Ordovician, <i>Holmden et al. (2012a)</i>	[Sr]	0.226	0.004	431	-0.0003 \pm 0.0001	-0.1630 \pm 0.0500	0.172	0.01	-74.2	-0.5759 \pm 0.1116	1.208 \pm 0.2746	-505.2		
	Sr/Ca	0.799	<0.001	-208.7	1377 \pm 187.6	-0.9522 \pm 0.0874	0.804	<0.001	-36.3	1.0346 \pm 0.1396	3.150 \pm 0.5746	172.4		
Ediacaran, <i>Husson et al. (2015)</i>	[Sr]	0.129	<0.001	4429.8	-0.0002 \pm 0.0000	-1.114 \pm 0.0273	0.403	<0.001	126.3	-0.6889 \pm 0.0351	0.6079 \pm 0.0968	-4303.5		
Ediacaran, <i>Sawaki et al. (2014)</i>	[Sr]	0.174	0.002	917.2	-0.0002 \pm 0.0000	-0.0994 \pm 0.0426	0.199	<0.001	30.0	-0.5003 \pm 0.0706	1.018 \pm 0.1605	-887.1		
Modern, <i>Fantle and Higgins (2014)</i>	Sr/(Ca+Mg)	0.372	0.04	12.8	-0.1790 \pm 0.0643	0.1519 \pm 0.0698	0.151	0.21	0.21	-0.3520 \pm 0.1511	-0.1328 \pm 0.0845	-12.6		
Compilation of all data	[Sr]	0.130	<0.001	10309	-0.0002 \pm -0.0003	-0.2265 \pm 0.0167	0.346	<0.001	328.9	-0.6466 \pm 0.0217	1.310 \pm 0.0584	-9979.9		
	Sr/Ca	0.302	<0.001	-3175	-196.3 \pm 10.19	-0.1376 \pm 0.0246	0.317	<0.001	-10.56	-0.8144 \pm 0.0418	-2.845 \pm 0.1165	3164.1		
	Sr/(Ca+Mg)	0.231	<0.001	203.8	-0.4785 \pm 0.0330	-0.0404 \pm 0.0332	0.347	<0.001	-32.0	-0.8281 \pm 0.0524	-0.6150 \pm 0.0234	-235.8		